# Aerosol–Cloud Interactions Over the Southern Ocean

Sean Hartery

A thesis submitted in partial fulfillment of the requirements for the Degree of Doctor of Philosophy in Physics

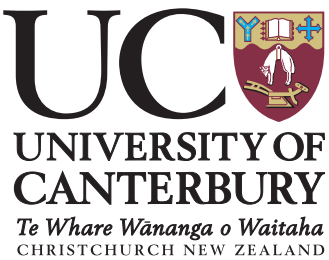


School of Physical and Chemical Sciences
College of Science
University of Canterbury
2021

*I ended up in search of ordinary things,*
*Like: how can a wave possibly be?*
*I started running, and the concrete turned to sand.*
*I started running, and things didn't pan out as planned.*

Bill Callahan, "Jim Cain"

# Abstract

In this work, connections between the abundance of sub-micrometer particulate within the marine boundary layer and optical properties of low-level marine stratus over the Southern Ocean are explored. Global climate models (GCMs) currently predict that much more shortwave radiation is entering the Earth system over the Southern Ocean than satellite-borne radiometers observe. This undermines long-term climate projections in the wider region, leading to greater uncertainty about our climate future. The central hypothesis of this thesis is thus: as the Southern Ocean is a region with near-total cloud cover, and as clouds are opaque to shortwave radiation, and as the abundance of boundary layer particulate available to nascent clouds is known to strongly influence the opacity of those clouds, then radiative biases within GCMs are fundamentally related to the abundance of boundary layer particulate.

The goals of this thesis are thus two-fold. First, to quantify whether GCMs accurately represent the abundance and types of particles present within the Southern Ocean boundary layer; and if not, use new observations to constrain existing parameterizations predicting their generation. Second, to quantify how sensitive Southern Ocean clouds are to variations in the abundance of such particles.

Central to this examination is a new record of measurements collected within the Southern Ocean boundary layer. In February of 2018, scientific instruments were installed on the R/V *Tangaroa* for a voyage to the Ross Sea. The voyage departed and returned to Wellington, New Zealand, providing 40 days of continuous in situ observations within the marine boundary layer. This included measurements of the abundance of suspended particulate by an optical particle counter, a differential mobility analyzer and a cloud condensation nuclei counter; discrete samples of ambient particulate collected on filters; attenuated backscattered light from the boundary layer measured by a ceilometer, and several meteorological variables measured by radiosondes and an automated weather station.

Measurements collected by the optical particle counter throughout this voyage were used to estimate the abundance of sea spray particles within the boundary layer. These particles were prevalent throughout the observational record. As they are highly soluble in water, these particles are ideal cloud condensation nuclei and form cloud droplets when the air saturates with water vapour during cloud formation. However, as the particles themselves are formed at the sea surface from crashing waves, they also contain insoluble organic detritus from bacteria which can act as nucleation points for ice. Since waves break as a result of the continual stress the wind exerts on the ocean surface, the generation of sea spray particles is primarily a function of near-surface wind speed. As the Southern Ocean is one of the windiest oceans on Earth, the measurements recorded throughout the 2018 voyage on the R/V *Tangaroa* provide a valuable data set to test the extremes of parameterizations for the flux of such particles. The results of this study indicate that existing parameterizations produce too many sea spray particles at all wind speeds, leading to significant biases. Based on the observational record, an existing parameterization for the flux of sea spray particles is constrained. This leads to an improved representation of sea spray particles within GCMs.

While this initial study provided a better characterization of the number of particles that may be available to nascent Southern Ocean cloud, low-level clouds can decouple from the boundary layer, which limits the number of particles that would normally be available to a new cloud. In a second study, in situ observations of the abundance of particle surface area are correlated to measurements of the total attenuated backscatter measured by a ceilometer to better understand the conditions in which low-level clouds have access to the reservoir of particulate available in the boundary layer. This study finds that the strong winds over the Southern Ocean provided sufficient turbulent kinetic energy to evenly mix particulate from the sea surface to cloud base, 80% of the time. As a result, in situ measurements of boundary layer particles measured near sea-level provide valuable information about the number of cloud condensation and ice nuclei available to cloud.

Finally, the sensitivity of low-level Southern Ocean cloud to variations in the abundance of sea spray particles is explored. This analysis leveraged recent model results from the Unified Model, a well-known GCM, which showed that the amount of shortwave radiation reflected by a low-level Southern Ocean cloud is very sensitive to the number of ice-nucleating particles available to it. This study demonstrated that a substantial fraction of the shortwave radiation bias over the Southern Ocean could be explained by improved representation of primary ice nucleation within mixed-phase clouds. These results are distilled into a simple parameterization for the amount of primary ice formed when a cloud freezes, which should be appropriate in climate models with a single-moment representation of cloud phase.

Thus, while many other physical phenomena influence the abundance and optical properties of Southern Ocean cloud, this thesis establishes that the abundance of boundary layer particulate is a fundamental physical quantity which governs the extraterrestrial input of energy into the Earth system. As such, future iterations of GCMs should give more careful attention to how these particles are generated within the simulated environment and how they interact with clouds. In this regard, the parameterizations developed within this thesis should provide a fruitful starting point.

**Deputy Vice-Chancellor's Office**
**Postgraduate Office**

UNIVERSITY OF CANTERBURY
*Te Whare Wānanga o Waitaha*
CHRISTCHURCH NEW ZEALAND

# Co-Authorship Form

This form is to accompany the submission of any thesis that contains research reported in co-authored work that has been published, accepted for publication, or submitted for publication. A copy of this form should be included for each co-authored work that is included in the thesis. Completed forms should be included at the front (after the thesis abstract) of each copy of the thesis submitted for examination and library deposit.

Please indicate the chapter/section/pages of this thesis that are extracted from co-authored work and provide details of the publication or submission from which the extract comes:

> *Chapter 3, "Constraining the Surface Flux of Sea Spray Particles from the Southern Ocean" was based on a research article published in the Journal of Geophysical Research.*
>
> *Hartery, S., Toohey, D., Revell, L., Sellegri, K., Kuma, P., Harvey, M., and McDonald, A.: Constraining the Surface Flux of Sea Spray Particles from the Southern Ocean, Journal of Geophysical Research: Atmospheres,* **125** *(4), 2020.*

Please detail the nature and extent (%) of contribution by the candidate:

> *Sean Hartery was the lead author on this study and is responsible for 80% of the material.*

**Certification by Co-authors:**
If there is more than one co-author then a single co-author can sign on behalf of all.

The undersigned certifies that:

- The above statement correctly reflects the nature and extent of the Doctoral candidate's contribution to this co-authored work;
- In cases where the candidate was the lead author of the co-authored work he or she wrote the text.

| Name: | Signature: | Date: |
|---|---|---|
| Adrian McDonald | Adrian McDonald | 30/4/2020 |

**Deputy Vice-Chancellor's Office**
**Postgraduate Office**

UNIVERSITY OF CANTERBURY
*Te Whare Wānanga o Waitaha*
CHRISTCHURCH NEW ZEALAND

# Co-Authorship Form

This form is to accompany the submission of any thesis that contains research reported in co-authored work that has been published, accepted for publication, or submitted for publication. A copy of this form should be included for each co-authored work that is included in the thesis. Completed forms should be included at the front (after the thesis abstract) of each copy of the thesis submitted for examination and library deposit.

Please indicate the chapter/section/pages of this thesis that are extracted from co-authored work and provide details of the publication or submission from which the extract comes:

> *Chapter 4, "Classification of the Below-Cloud Mixing State Using In-Situ and Remotely-Sensed Measurements" was based on a research article submitted to the journal, Journal of Geophysical Research: Atmospheres.*
>
> *Hartery, S., Kuma, P., Harvey, M., and McDonald, A.: Classification of the Below-Cloud Mixing State Using In-Situ and Remotely-Sensed Measurements, Journal of Geophysical Research: Atmospheres (under review).*

Please detail the nature and extent (%) of contribution by the candidate:

> *Sean Hartery was the lead author on this study and is responsible for 80% of the material.*

**Certification by Co-authors:**
If there is more than one co-author then a single co-author can sign on behalf of all.

The undersigned certifies that:

- The above statement correctly reflects the nature and extent of the Doctoral candidate's contribution to this co-authored work;
- In cases where the candidate was the lead author of the co-authored work he or she wrote the text.

| Name: | Signature: | Date: |
|---|---|---|
| Adrian McDonald | Adrian McDonald | 30/4/2020 |

# Acknowledgements

Thank you to all of the kind and friendly folks at the National Institute of Water & Atmospheric Research. Thank you to the reception team: Carolyn, Lisa, Victoria and Ebony for teaching me the ropes. Thanks especially to Andrew, for the bench space in the aerosol lab; Tony, for the valuable mentorship in balloon operations; Carolann, for the many, many lunches and daily discussion of memes; Nick, for his friendship; and especially Mike Harvey, who not only co-supervised this thesis, but provided many neat and interesting opportunities while I was at the NIWA office. I owe a lot to your mentorship and expertise. More thanks are owed to the folks up at NIWA Auckland: particularly Guy and Gus, who lent us their SMPS for the voyage. Gus, in particular, gave me some invaluable training on maintaining these instruments. Additional thanks to those at NIWA Lauder for their hospitality during a field testing experiment in 2017, particularly fellow Canadian, Richard.

Gratitude to Capt. Solly of the R/V *Tangaroa* and his skilled crew: particularly deck hands Bruce, Bryce, Glenn and Shane who helped us launch balloons. Your skills gave us safe passage through the Ross Sea in some genuinely rotten weather.

Thanks to some colleagues outside of NIWA, in particular: Karine, for her critical eye on our sea spray measurements, as well as the opportunity to run her experiments while out on the Tangaroa; and, David for his help getting the CPC3010 back up to par before the voyage.

The friends and colleagues I met in my time at the University of Canterbury: Peter, for putting up with me for 60+ days at sea; Ethan, for the Wilson-esque appearances over the cubicle divider; Alex, for the tea trips every now and then; Laura, for her bewildering amount of atmospheric chemistry knowledge; Darin, for his gracious sharing of SOCRATES data and illuminating discussions. Finally, thanks to Adrian McDonald for trusting me with this opportunity. This project took me to reaches of the world this Nova Scotian never expected to see. I still remember towards the end of my initial interview four years ago, you asked if I was really interested in going out to the Southern Ocean. I'm not sure I knew then, what I was getting myself into; but, I have a framed picture of a penguin and that's nice.

Lastly, on a personal level: this work would not have been possible without the support of friends and family back in Canada. Thanks to my Mom and Dad for their enduring support. And, Alexandra. Thank you for your constant encouragement and love.

# Table of Contents

# List of Figures

# List of Tables

# List of Abbreviations

| | |
|---|---|
| **AGL** | Above Ground Level |
| **AIC** | Akaike Information Criterion |
| **AMPS** | Antarctic Mesoscale Prediction System |
| **AOD** | Aerosol Optical Depth |
| **ASL** | Above Sea Level |
| **AVHRR** | Advanced Very-High-Resolution Radiometer |
| **AWS** | New Zealand MetService's Automated Weather Station |
| **BDC** | Bipolar Diffusion Charger |
| **CBH** | Cloud Base Height |
| **CCM** | Chemistry-Climate Model |
| **CCN** | Cloud Condensation Nuclei |
| **COARE** | Coupled Ocean-Atmosphere Response Experiment |
| **CPC** | Condensation Particle Counter |
| **CRDS** | Cavity Ring-Down Spectrometer |
| **DMPS** | Differential Mobility Particle Sizer |
| **EC** | Electrostatic Classifier |
| **FLEXPART** | FLEXible PARTicle transport model |
| **FSSP** | Forward Scattering Spectrometer Probe |
| **HIAPER** | High-performance Instrumented Airborne Platform for Environmental Research |
| **INP** | Ice Nucleating Particle |
| **LCL** | Lifted Condensation Level |
| **LPDM** | Lagrangian Particle Dispersion Model |
| **LWC** | Liquid Water Content |
| **MBL** | Marine Boundary Layer |
| **MODIS** | Moderate Resolution Imaging Spectroradiometer |
| **NDVI** | Normalized Difference Vegetation Index |
| **NSE** | Nash-Sutcliffe model Efficiency coefficient |
| **OPC** | Optical Particle Counter |
| **PBL** | Planetary Boundary Layer |
| **PCASP** | Passive Cavity Aerosol Spectrometer Probe |
| **PDF** | Probability Density Function |
| **PLPDM** | Pseudo-Lagrangian Particle Dispersion Model |
| **RF** | Research Flight |
| **SOCEX** | Southern Ocean Cloud Experiment |
| **SOCRATES** | Southern Ocean Clouds, Radiation, Aerosol Transport Experimental Study |
| **SSP** | Sea-Spray Generated Particle |
| **SST** | Sea Surface Temperature |
| **UHSAS** | Ultra-High Sensitivity Aerosol Spectrometer |
| **WRF** | Weather Research & Forecasting model |

# List of Variables

A table of common variables used throughout this thesis. There is unfortunately some repetition: $N$ denotes both the abundance of particles and the Brunt-Väisälä Frequency. P denotes both a probability and pressure. Fundamental variables are listed first, then grouped by dimension.

| | | |
|---|---|---|
| C | Total Number of Particles | – |
| N, n | Total Abundance of Suspended Particulate | $cm^{-3}$, $m^{-3}$ |
| A, a | Total Abundance of Suspended Particle Surface Area | $m^2$ $cm^{-3}$ |
| M, m | Total Abundance of Suspended Particle Mass | kg $m^{-3}$ |
| $\rho$ | Density | kg $m^{-3}$ |
| $\nu$ | Average Volume per Particle | $m^3$ |
| $D$ | Diameter | $\mu$m, m |
| $h$ | Thickness of an Atmospheric Layer | m, km |
| $z$ | Altiude | m, km a.s.l. |
| $T$ | Temperature | K, °C |
| $T_w$ | Sea Surface Temperature | K, °C |
| $\theta_v$ | Virtual Potential Temperature | K |
| $U$ | Scalar Magnitude of Wind Speed | m $s^{-1}$ |
| $I$ | Precipitation Rate | mm $hr^{-1}$ |
| $N$ | Brunt-Väisälä Frequency | $s^{-1}$ |
| $S$ | Vertical Wind Shear | $s^{-1}$ |
| $\Lambda$ | Scavenging Rate of Particulate by Precipitation | $s^{-1}$ |
| $\tau$ | Lifetime | s, min, hr, day |
| $t$ | Time | s, min, hr, day |
| $\mathcal{P}$ | Sensitivity of an Observation to a Volume Flux | s, min, hr, day |
| P | Probability | % |
| $RH$ | Relative Humidity | % |
| $\eta$ | Sampling Efficiency | – |
| $\phi$ | Number of Bound Charges | – |
| $s$ | Saturation Ratio of Water Vapour | – |
| $w$ | Mixing Ratio | – |
| $Ri$ | Richardson Number | – |
| $\Omega$, $\Gamma$ | Instrument Transfer Functions | – |
| $W$ | Fraction of Ocean Surface Covered in Breaking Waves | – |
| $\beta$ | Attenuated Backscatter | $m^{-1}$ $sr^{-1}$ |
| $Q$ | Flow Rate | L $min^{-1}$ |
| $P$ | Pressure | Pa, hPa |
| $V$ | Voltage | V |
| $F$ | Flux | $m^{-2}$ $s^{-1}$ |
| $SW$ | Shortwave Reflectivity | W $m^{-2}$ |

# The Shortwave Radiation Bias over the Southern Ocean

## 1. Introduction

Recent comparisons between the total amount of outgoing shortwave radiation estimated by global circulation models (GCMs) and measured from satellites have revealed that there are significant biases over the Southern Ocean (Trenberth and Fasullo, 2010). South of 55° S, models consistently over-predict the amount of shortwave radiation reaching the Earth's surface relative to satellite observations (Schuddeboom et al., 2019). However, the troposphere over the Southern Ocean is an extremely cloudy place, with the surface being obscured >80% of the time (Haynes et al., 2011). Thus, biases in radiation can arise when a model incorrectly predicts cloud properties: depth, breadth, opacity, phase, lifetime, etc., which would allow excess shortwave radiation to reach the Southern Ocean.

Looking out at the Southern Ocean sky, many familiar cloud types are present: streaking cirrus, cumulus fractus, stratus, etc. However, most, if not all of these are obscured by the most widespread and common cloud: marine stratocumulus. This low-lying cloud tends to form at the top of the boundary layer (Lock et al., 2000). Despite being relatively commonplace, not all marine stratocumulus are created equal: research has found that the shortwave radiation bias is strongest within the cold sector of extra-tropical cyclones (Bodas-Salcedo et al., 2014). A climatology of cyclones in the Southern Hemisphere supports this, too: storm tracks are densest between 55°S and the Antarctic coastline (Irving et al., 2010), precisely where the shortwave radiation bias is strongest (Kay et al., 2016; Schuddeboom et al., 2019). Extra-tropical cyclones are a common occurrence in the Southern Ocean (Irving et al., 2010): one of the windiest and most inhospitable seas on Earth (Hande et al., 2012a). As a result, the Southern Ocean boundary layer is a dynamic environment. However, the coarse vertical resolution within climate models means that the simulated boundary layer can often be too calm or too shallow. This is thought to produce optically thin stratocumulus clouds within GCMs, which weakly reflect incoming solar radiation (Williams et al., 2013). However, others have suggested the opposite, showing that stratocumulus within GCMs are actually too opaque and that the regional radiation bias is instead a result of severe under-prediction of their occurrence (Nam et al., 2012).

More recently, it has been proposed that the shortwave radiation bias stems primarily from errors in predicting cloud-top phase, as clouds with super-cooled liquid tops are responsible for reflecting 27–38% of the total incoming shortwave radiation, relative to other cloud types (Bodas-Salcedo et al., 2016). Indeed, cloud opacity in the cold sector is very sensitive to how cloud glaciation is parameterized within models (Vergara-Temprado et al., 2018). Depending on the spatial and temporal resolution of model, these parameterizations can be quite simple: global climate models like the HadGEM3-GA7, generate a fixed amount of ice in any cloud colder than -10°C (Furtado and Field, 2017). However, in reality, high-latitude, low-level clouds are abundant in super-cooled liquid water (Hogan et

**Figure 1.1 :** March 2017 – Campbell Plateau. Marine Stratocumulus (lower left) threatens to obscure a brief glimpse of the sky from the R/V *Tangaroa*.

al., 2004; Huang et al., 2012). Despite its global significance, a path forward for parameterizing ice nucleation within clouds remains an open issue in the numerical modelling community (Herbert et al., 2014).

These biases fundamentally undercut the utility of regional climate projections. Not only do they imply that clouds (and thus, precipitation) are modelled poorly in the region, the surplus of radiation within these models results in many compounding effects, which aren't just restricted to the Southern Ocean. For instance, the radiation bias can strongly influence inter-hemispheric energy transport, resulting in poor predictions of precipitation in tropical, equatorial zones (Hawcroft et al., 2017). Further, the additional radiation leads to warmer seas, affecting storm track predictions and sea ice. Ultimately, the accuracy of climate predictions in both New Zealand and the wider Southern Ocean region is undermined by these uncertainties.

# 2. Background

To correctly represent the transfer of radiation through a cloud, a model not only needs to generate clouds of sufficient breadth and depth, it must also accurately determine the opacity and lifetime of the cloud, too. While the spatial extent of a cloud is predominantly a function of synoptic conditions and dynamic forcings, the opacity and lifetime of a cloud can be significantly modulated by the abundance and physical properties of the precursor aerosol.

*a. Cloud Condensation Nuclei*

A cloud condensation nuclei is any particle suspended in the atmosphere that, when exposed to a supersaturation of water vapour, acts as a condensation site for liquid water. This process is known as heterogeneous nucleation (Pruppacher et al., 1998). While it is technically possible for water vapour to spontaneously condense onto itself, i.e. homogeneously nucleate, the supersaturation of water vapour required to do so is several orders of magnitude higher than what is required for heterogeneous nucleation. Hence, the latter is the favoured nucleation mechanism, as particles are in sufficient abundance anywhere

cloud forms. Not all particles are equal, however: the supersaturation required for water vapour to condense onto a particle is strongly governed by the seed particle's size and its solubility in water (Petters and Kreidenweis, 2007). As such, only particles of a sufficiently large diameter, typically >50 nm, and suitable chemical composition act as nuclei. These particles, being cloud forming agents, are thus named cloud condensation nuclei (CCN).

*b. Ice-Nucleating Particles*

Particles also influence the phase transition of clouds. Depending on the physicochemical properties of the particles, condensation of water vapour may be severely inhibited during cloud activation, leaving some particles as solid suspended material within the cloud. When the temperature of a cloud falls below the freezing point, collisions between cloud droplets and these solid particles can initiate spontaneous droplet freezing. Particles which fill this role are known as ice-nucleating particles (INPs). However, it is not even necessary for a particle to remain solid through cloud formation. Immersion ice nuclei are solid particles that are embedded within cloud condensation nuclei. These particles typically do not freeze immediately once cloud temperatures fall below 0°C. Just as a supersaturation of water vapour is necessary for condensation, super-cooled temperatures are necessary for immersion freezing. While the homogeneous nucleation of ice in a droplet of pure liquid water will occur once it cools to -38°C (Rosenfeld and Woodley, 2000; Jeffery and Austin, 1997), depending on the available surface area of immersion nuclei, freezing can occur at much warmer temperatures (Irish et al., 2019).

*c. Direct and Indirect Radiative Effects*

The abundance of both CCN and INPs can have profound effects on the opacity of clouds. Aircraft studies have previously shown that the number of cloud condensation nuclei below cloud is linearly related to the number of cloud droplets observed within cloud over the Southern Ocean (Yum and Hudson, 2004). This leads to the well-known aerosol indirect effect: the abundance of cloud condensation nuclei available to a forming cloud determines its opacity (Twomey, 1977). This also leads to a secondary effect, sometimes known as the cloud lifetime effect: increasing the abundance of CCN leads to smaller cloud droplets, since the available water vapour is partitioned across a larger surface area (Albrecht, 1989). This inhibits droplet growth, delays precipitation, and extends the lifetime of clouds.

Within mixed-phase clouds, the abundance of CCN and ice-nucleating particles produce two more indirect effects. First, increasing the number of ice-nucleating particles leads to more rapid glaciation. Once formed, additional droplets which collide with the new ice particle will freeze and adhere in a process known as riming. This secondary formation process rapidly glaciates the cloud and scavenges any available cloud droplets, leading to less opaque clouds (Hu et al., 2010). In contrast, increasing the number of cloud condensation nuclei results in smaller droplets, which freeze at much cooler temperatures (Pruppacher et al., 1998). Thus, in both liquid and mixed-phase clouds, an increase in the abundance of CCN can extend cloud lifetimes (Borys et al., 2003).

In a cloud-free troposphere, both CCN and INP can also directly reflect a substantial amount of shortwave radiation (Bohren and Huffman, 1983). However, as the reflectivity of particles in the Rayleigh scattering regime ($D_p < \frac{\lambda}{2}$) is several orders of magnitude smaller than particles in the geometric regime ($D_p > 2\lambda$), the strength of this direct radiative effect is mostly dictated by the abundance of the largest particles ($D_p > 1\mu$m). However, the size of these particles means that they are more likely to deposit to the surface (Slinn, 1977). As a result, they will only remain in suspension if turbulence is significant, leaving them mostly confined to the boundary layer. As the Southern Ocean boundary layer is almost

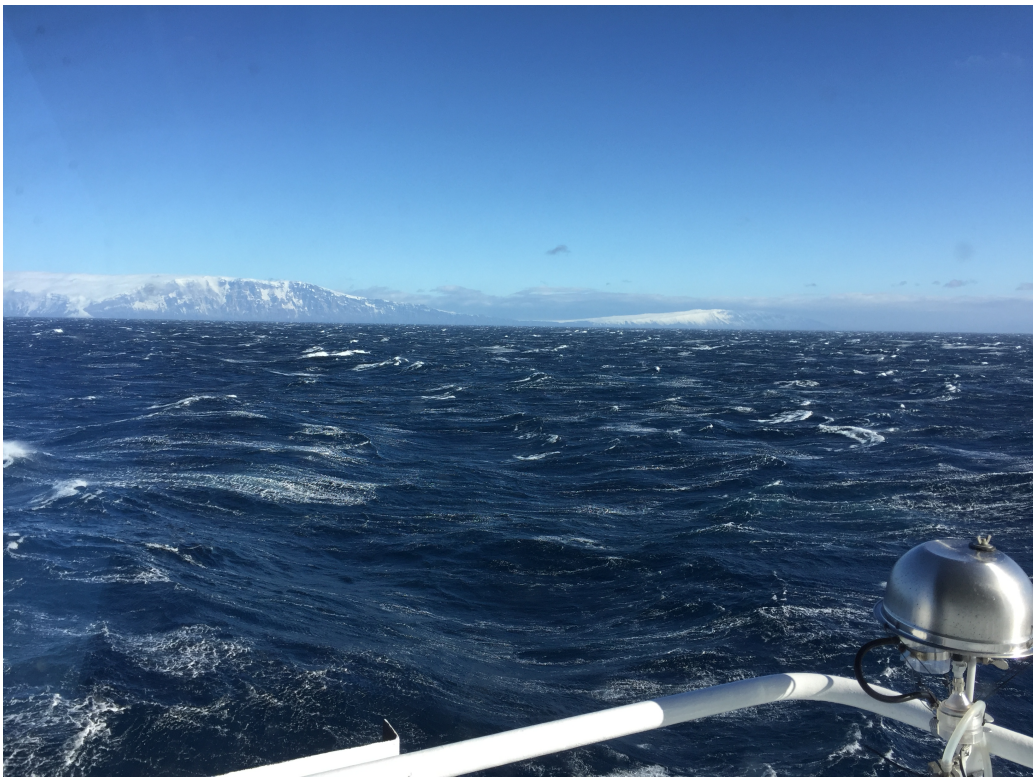

**Figure 1.2 :** February 2018 – Cape Adare. Waves breaking off the coast of Cape Adare, Antarctica. View from the bridge of the R/V Tangaroa.

always covered in cloud, the direct effect tends to be much less important to the overall radiation balance.

# 3. Measurements of Particulate in the Southern Ocean Boundary Layer

To understand the extent to which cloud optical properties are modified by the aerosol particles present within the boundary layer, it is important that the abundance, composition, and size of those particles be well characterized. However, the harsh environment of the Southern Ocean is often a hindrance to direct observation. High winds and cold temperatures year-round make the region inhospitable. In this section, a brief overview of previous field campaigns in the region will be provided. Up-to-date knowledge of the physical and chemical properties of Southern Ocean boundary layer aerosol particles will also be summarized.

Some of the earliest attempts to characterize the particulate present in the Southern Ocean boundary layer took place on ships during the establishment and subsequent maintenance of Antarctic field stations. These included attempts to quantify the number of ice-nucleating particles, which found an almost total absence of such particles compared to other regions of the world (Bigg and Hopwood, 1963). The first measurements of the total abundance of particles in the Antarctic boundary layer took place in 1965 on the 10$^{th}$ Soviet Antarctic Expedition, and also reported a relatively pristine atmosphere (Voskresenskii, 1968). Detailed electron microscope studies of suspended particulate at Mt. Discovery followed shortly, finding sulfate particles were the dominant species by number relative to other chemical constituents (Cadle et al., 1968). A scientific consensus soon formed: ma-

rine gasses emitted from the mid-tropics are driven by the polar cell up into the free troposphere and stratosphere and towards the South pole. Once above the marine stratocumulus, these gasses are rapidly photo-oxidized into more volatile by-products which can homogeneously nucleate into new particles. Near the pole, subsidence draws these newly-formed particles into the boundary layer. As these new particles were nucleated in situ from gasses, there is no functional surface area embedded in the particle to nucleate ice, corroborating the lack of INPs observed by Bigg and Hopwood (1963). The theory of Cadle et al. (1968) is still mostly consistent with the decades of observation in the marine boundary layer that have followed. However, the wide variety of organisms, gasses, and chemical interactions involved in this process mean that this particle formation pathway is much more complex than this simple model. Current knowledge of the relevant chemical constituents, particle formation pathways, and boundary layer entrainment processes will be summarized in this section.

Dimethyl sulfide (DMS) is a well-known pre-cursor to such particles. It is generated by *dinoflagellate* and *coccolithophore* phytoplankton communities at the surface of the ocean as dimethylsulfoniopropionate (DMSP) (Walker et al., 2016), which the phytoplankton use as an osmolyte and metabolic compound (Andreae and Barnard, 1984). When these phytoplankton communities bloom, and subsequently die, DMSP is available in large quantities at the ocean surface. The resulting surplus of DMS is then transferred across the ocean interface with the help of winds and wave breaking (Bell et al., 2017). Globally, marine production of DMS adds an estimated 28.1 Tg of sulfur to the atmosphere, per annum (Lana et al., 2011). Once in the atmosphere, DMS can also be broken down by bromine oxide (Veres et al., 2020), leading to the production of methanesulfonic acid (MSA), another particle precursor (Hara et al., 2005). Results from tethered balloons show that the number of small, newly-formed particles reaches a maximum well above the boundary layer, near 750 mb, indicating that the production of these particles tends to occur in the free troposphere (Ito, 1985).

*a. Sulfate Particles*

Perhaps some of the best understanding of sulfate particles within the Southern Ocean boundary layer has come from the Aerosol Characterization Experiment (ACE-1) (Murphy et al., 1998; Bates et al., 1998; Pósfai et al., 2003). Over the course of the ACE-1 experiment, the size distribution of particles was observed to consist of 3 or 4 lognormal modes: an ultra-fine (or Young Aitken) mode centred around 16 nm, with an abundance of 190 particles $cm^{-3}$; an Aitken mode of 210 $cm^{-3}$ at 33 nm; an accumulation mode of 74 $cm^{-3}$ at 110 nm; and a coarse mode of 15 $cm^{-3}$ at 540 nm (Bates et al., 1998). Throughout the expedition, the Young Aitken mode was only present $\sim$50% of the time (Bates et al., 1998). Particles in this size range are formed from the homogeneous nucleation of volatile gasses. As there was no direct evidence of particle formation in the boundary layer, these particles were assumed to have been entrained into the boundary layer during the passage of cold fronts (Bates et al., 1998). The enhancement of newly-formed particles following the passage of cold fronts has also been documented at Cape Grim (Gras et al., 2009). However, not just the smallest particles are composed of sulfate: a chemical analysis revealed that the Young Aitken, Aitken, and accumulation mode particles were all predominantly sulfate in composition, reflecting the relevance of this particle formation mechanism (Murphy et al., 1998). The size of these particles is, instead, reflective of their age. Aitken and Young Aitken mode particles are newly-formed particles that are entrained into the boundary layer. Over time, these particles grow via condensation of additional sulfuric vapours until they are large enough to act as cloud condensation nuclei within cloud. When a cloud is formed

**Figure 1.3 :** February 2018 – Ross Sea. A humpback whale breaches the air–sea interface with its tail. An unexpected, but minor, source of sea spray.

from these particles, the sulfate particle population is bifurcated: particles large enough to act as CCN will form cloud droplets, whereas all of the smaller particles will remain interstitial within the cloud (Hoppel et al., 1986). If the cloud precipitates, the largest particles will be lost to the surface below, leaving only the smallest particles behind. However, if the cloud simply evaporates, those large particles will effloresce and detrain into the boundary layer below. Such particles form the accumulation mode. As a result, only the accumulation mode and coarse mode particulate are available as cloud condensation nuclei at the supersaturations typical of Southern Ocean cloud (0.2–0.3%) (Fossum et al., 2018).

*b. Sea Spray Particles*

In contrast to the accumulation and aitken mode particles, coarse mode particles observed in the Southern Ocean boundary layer are primarily composed of sea salt (Murphy et al., 1998; Quinn et al., 2017). The strong winds over the Southern Ocean consistently transfer momentum from the atmosphere to the ocean, leading to the development of large waves around Antarctica (Jiang and Chen, 2013). Sea spray particles are generated when the slope of those waves, and hence the weight of the ocean surface, overcomes surface tension (Snyder and Kennedy, 1983). When this happens, the surface of the wave shears, entraining air into the ocean surface. Air rapidly rises and dissipates back into the atmosphere in a matter of seconds, forming bubbles (Callaghan et al., 2012). As these bubbles burst, particles are produced via two mechanisms: film bursting, which is the actual rupturing of the bubble at the sea-air interface; and jet bursting, which is the creation of large droplets from the gravitational collapse of the cavity left by the burst bubble. Generally speaking, sea spray particles with diameters $<1$ $\mu$m are generated from film drops, while particles $>1$ $\mu$m are generated from jet drops (Monahan et al., 1986). While the accumulation mode (sulfate particles) often outnumbers the coarse mode particulate (sea spray particles) in calm conditions and high in-cloud water vapour supersaturations, the opposite is true in windy condition and

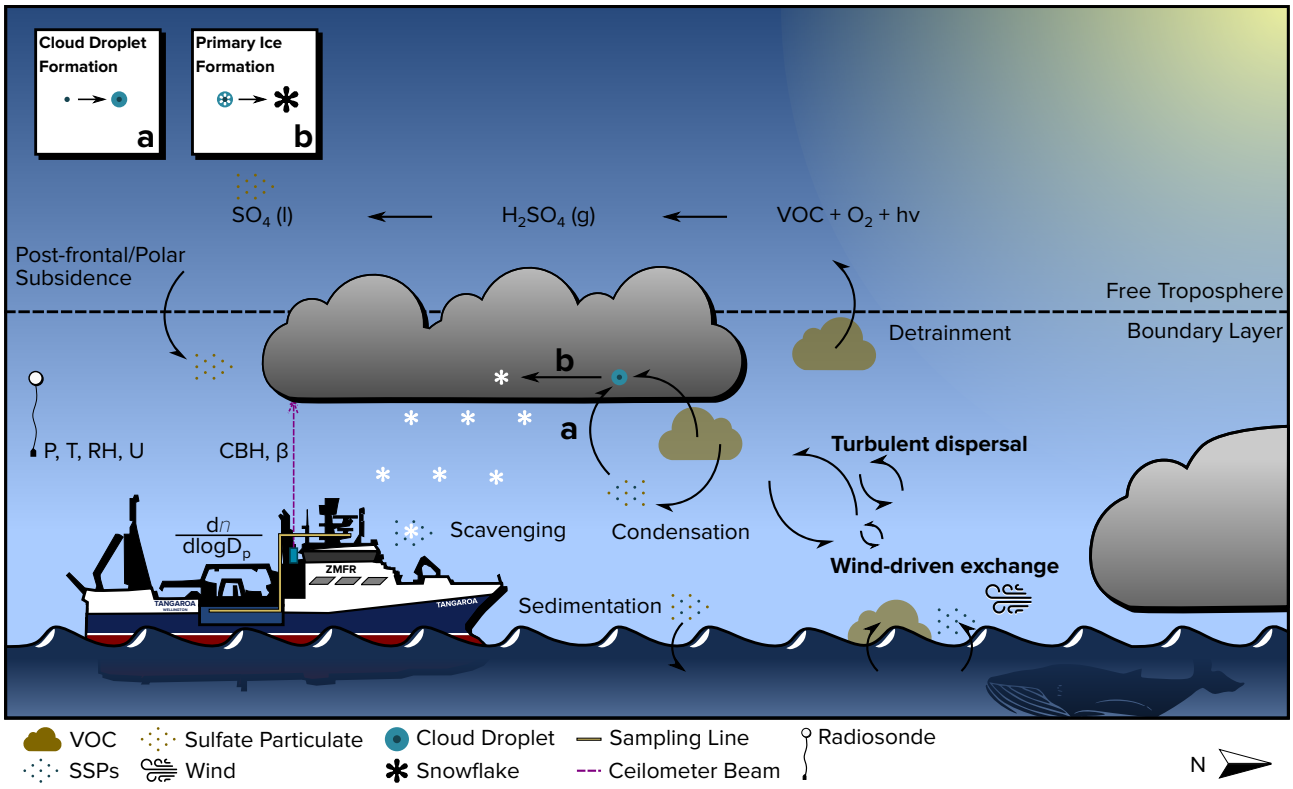


**Figure 1.4 :** A schematic of the relevant processes which generate (and scavenge) particles in the Southern Ocean boundary layer. Volatile organic compounds (VOCs) emitted from phytoplankton are shown rising through the boundary layer into the troposphere. Once they reach sunlight, these gasses oxidize, accumulate and saturate to form new particles. These particles are entrained following cold fronts (Gras et al., 2009) and over Antarctica where the Polar cell converges (Cadle et al., 1968). In contrast, larger particles are formed directly from breaking waves, Sea Spray Particles (SSPs). These particles are thoroughly scavenged by the clouds which form at the top of the boundary layer. Though few in number these particles act as ice nuclei (DeMott et al., 2016; Pósfai et al., 2003), leading to the phase transition of clouds. Measurements of the particle size distribution (dn $(\mathrm{dlogD}_p)^{-1}$), cloud base height (CBH), backscattered light from particles ($\beta$), and thermodynamic profiles of pressure (P), temperature (T), humidity (RH) and wind (U) were all used in this thesis to understand how these particles are formed, how they enter clouds, and ultimately how they govern the radiation budget in the region.

low in-cloud supersaturations (Fossum et al., 2018). In such cases, sea spray particles can make up 100% of the CCN. As such, they are vital to understanding the shortwave reflectiviy of Southern Ocean clouds. Further, as these particles are remnant fragments of the ocean surface, their composition reflects this, too. So while they mostly resemble seawater (Murphy et al., 1998), organic detritus and bacteria present at the ocean surface can find its way into these particles (Pósfai et al., 2003; Uetake et al., 2020). As a result, sea spray particles, despite their innate solubility in water, are also weak ice nuclei (DeMott et al., 2016).

These two broad categories of particles (sea spray, sulfate) encompass the majority of particles observed over the Southern Ocean. As a result, understanding the abundance of both constituents is fundamental to understanding cloud over the Southern Ocean. However, these two categories of particles are not completely independent: extrapolations from measurements at Syowa station, Antarctica suggest that the scavenging of MSA, a sulfate particle pre-cursor, by coarse mode sea spray depletes 10% of the total atmospheric sulphur budget (Hara et al., 2005).

# 4. Summary

A relatively broad picture of particulate in the Southern Ocean boundary layer now comes into view: sulfur compounds released from marine biota bubble up through the air–sea interface and are turbulently mixed up through the boundary layer and into the free troposphere (see Fig. 1.4). Once in the free troposphere, photo-chemical oxidation of these sulfur species slowly converts them into more volatile gasses (sulfur dioxide, MSA, and ultimately sulfuric acid) as they are advected along the poleward flow. Moving southward, these gasses continue to oxidize and accumulate, until they saturate within the free troposphere, forming new particulate via homogeneous nucleation.

After formation, particle concentrations tend to be high, leading to rapid self-coagulation. This process leads to quick growth of the small particulate at the expense of particle number, but the process is exhausted once the average particle diameter reaches 30 nm. These particles form the Aitken mode. Near the pole, the converging winds of the polar cell result in strong subsidence. Particles are drawn down into the boundary layer, where they reverse their heading and make their way to the coast along dry katabatic winds. Subsidence can occur in frontal zones over the ocean, too, bringing new particulate directly into the boundary layer. Along their trajectory, these particles grow to cloud-relevant sizes via condensation. Once the particles are activated within a cloud, the population is bifurcated, with the larger particles detraining from non-precipitating clouds as the now cloud-processed accumulation mode. Existing at a minimum of all particle loss processes (deposition and scavenging by precipitation), these cloud-processed particles tend to accumulate over time, providing a reservoir of nuclei for boundary layer cloud that is only ever diminished when cloud precipitates.

The lifetime of a sea spray particle is much simpler. Due to their large size and inherent hygroscopicity, these particles readily activate within clouds. As a result of the near-constant winds over the Southern Ocean, these particles are almost always available, too: though, they are often outnumbered by the accumulation mode particles. Despite this, their ample surface area acts as an efficient sink for marine gasses; thus, the presence of sea spray acts as a buffer against the generation of new sulfate particles.

The complex interactions which govern the formation and cloud-relevance of sulfate particles have been the basis of many scientific efforts within the Southern Ocean. Though still inconclusive to this day, it has been conjectured that these particles are climate moderators (Charlson et al., 1987). Sea spray particles, too, are thought to moderate climate (Korhonen et al., 2010). However, the radiation biases over the Southern Ocean have revealed that global climate models are unable to resolve cloud phase. Accurately predicting the phase of clouds is more strongly tied to predicting the abundance of ice-nucleating particles, than cloud condensation nuclei. While sea spray particles are only weak ice-nucleating particles (McCluskey et al., 2018), they are potentially the only source of such particulate (Vergara-Temprado et al., 2017), as sulfate particles do no nucleate ice. Hence, despite their relative sparsity, there are many valuable questions to answer in regards to the connection between the bacteria within sea spray particles and the phase of the cloud overhead. Thus, a comprehensive evaluation of the number of sea spray particles available in the boundary layer, how those particles are entrained into low-level clouds, and how they initiate phase transitions within cloud could lead to significant improvements to predictions of the radiation balance over the Southern Ocean.

# 5. Thesis Outline

In this chapter, it was established that the optical properties of Southern Ocean cloud are fundamentally connected to the availability and physicochemical properties of boundary layer particulate. The primary goal of this thesis is to evaluate how well global climate models estimate the formation of particles in the boundary layer and characterize how the properties of those particles affect cloud phase. First, this thesis will use in situ observations collected over the course of a 2018 voyage to the Ross Sea to study parameterizations of particle formation mechanisms directly. Then, conditions in which particles measured near the ocean surface were relevant to cloud formation will be defined. Finally, key assumptions GCMs make about cloud phase and cloud formation will be addressed.

**The Tangaroa Marine Environment and Ecosystem Voyage**
Measurements conducted aboard the R/V *Tangaroa* are described. The sampling efficiency of the main sampling conduit is characterized and quality control for various instruments is discussed. Some limited measurement theory is provided to contextualize data processing. Significant portions of this chapter are present in a manuscript describing the entire suite of atmospheric trace gas, aerosol, and cloud measurements made during the Marine Environment and Ecosystem Voyage. Though the material presented here and in Sections 3.8 and 4.2.2 of the manuscript originated from the author, the manuscript was led by Dr Stefanie Kremser and has been submitted to the journal *Earth System Science Data* as of October 2020.

**Constraining the Surface Flux of Sea Spray Particles from the Southern Ocean**
To better constrain the source of sea spray particles, particles measured on the R/V *Tangaroa* were simulated backwards in time with a Lagrangian particle dispersion model. This provided a one-to-one map between measurements and the upwind sea surface, creating a framework through which the environmental factors which affect sea spray particle flux could be studied. This framework was then used to optimize an existing parameterization for the surface flux of sea spray particles based on the near-surface wind speed. Finally, a database of observations of surface ocean wave-breaking was compiled, which corroborated the new parameterization. This study was published in the *Journal of Geophysical Research: Atmospheres* in February 2020.

**Classification of the Below-Cloud Mixing State Using In-Situ and Remotely-Sensed Measurements**
To understand the impact these particles have on overlying cloud, it was necessary to establish conditions in which they're available to nascent clouds. Measurements of backscattered light from a ceilometer on the R/V *Tangaroa* were correlated to the abundance of particulate surface area measured at sea-level. The strength of this correlation was then used to define periods when the boundary layer was well-mixed. This study has been submitted to and is under review for submission in, *Geophysical Research Letters*.

**Ice-Nucleating Particles over the Southern Ocean**
Measurements of the number of ice-nucleating particles within the Southern Ocean Boundary Layer are presented. A simple method for generating climatologies of such particles is then described. Finally, these climatologies are leveraged to explore potential biases within a GCM, based on its implicit and explicit microphysical assumptions. The results confirm that sea spray particles are indeed the predominant source of ice nuclei in the region. The sensitivity of cloud phase to the abundance of sea spray particles is then discussed.

# The Tangaroa Marine Environment and Ecosystem Voyage

The key scientific instrument throughout this entire thesis was the R/V *Tangaroa* itself. The *Tangaroa* is a 70 m long, purpose-built research vessel with a beamwidth of 13.8 m and a draught of 7 m. It can accommodate 40 people, including a mix of research staff and ship personnel. With a fuel capacity of 620 $m^3$, the ship can endure 60 days at sea, port-to-port. Over the course of the Marine Environment and Ecosystem Voyage, the R/V *Tangaroa* travelled 11,000 km. The Tangaroa departed from Wellington Harbor on February 9, and returned on March 21, 2018. The bulk of the voyage was spent in waters south of 60°S, with 17 days of the voyage spent in seas between 60–70°S and 13 days of the voyage south of 70°S. The full ship track is shown in Fig. 2.2.

## 1. Measurements

*a. Particle Counting Instruments*

The most difficult logistical challenge in running equipment aboard the *R/V Tangaroa* was finding a suitable laboratory location. Access to un-polluted ambient marine air was the only requirement. Since the ship itself was the sole producer of anthropogenic particulate in the immediate area, air needed to be sampled from a point nearest the bow to avoid sampling the ship's exhaust. The sampling inlet also needed to be positioned reasonably aloft, such that seawater wouldn't be aspirated during heavy weather. In general, the deck above the bridge offered the best vantage point as it minimized exposure to the both the midships and aft-ships exhaust stacks. In addition, the suite of meteorological sensors aboard the *R/V Tangaroa* are all located above the bridge, so real-time meteorological measurements could easily be merged with the aerosol measurement time-series. However, there is no suitable sheltered location atop the bridge in which to set-up all of the instrumentation. No indoor locations were deemed suitable, either, as the majority of the forecastle was devoted to accommodations and communal spaces for scientific and ship staff.

Ultimately, it was decided that ambient air would be drawn through a conduit to a container laboratory elsewhere on the ship. The container laboratory was a retro-fitted 6 m$\times$3 m$\times$3 m shipping container on the trawl deck (1–2 m a.s.l.). In Fig. 2.3a, the location of the container laboratory relative to the sampling inlet is shown.

Approximately 40 m of 0.1 m inner diameter (ID) conductive hose was used to create a conduit between air near the mast and the instrumentation in the container laboratory below. Air was drawn through the conduit at a flow rate of $3.92 \times 10^{-2}$ $m^3$ $s^{-1}$ by two pumps. The conduit was attached to a manifold of plastic plumbing parts within the laboratory (Fig. 2.3b). This was necessary to plumb the particle sampling instrumentation to the conduit, as the majority of the instruments were designed with $6.35 \times 10^{-3}$ m outer diameter inlets.

From the sampling manifold in Fig. 2.3b, air was drawn either directly into the Passive


**Figure 2.1 :** February 2018 – Ross Sea. The stern of the ship on a particularly foggy and snowy day.

Cavity Aerosol Spectrometer Probe (PCASP-100x; Droplet Measurement Technologies) or through a diffusion drier to the remaining instrumentation. In the former, the plumbing first stepped down from the manifold into a 0.032 m flexible hose. This was clamped to the inlet of the PCASP-100X using a worm clamp.

Air was drawn into the diffusion drier via 0.24 m of $6.35 \times 10^{-3}$ m Synflex tubing inserted into the center of the sampling manifold's air stream. Air was drawn through the Synflex tubing via the combined instrument flows of the dry particle sub-system ($9.2 \times 10^{-5}$ m$^3$ s$^{-1}$). Particles in the dry particle sub-system passed through a diffusion drier before continuing to the rest of the instrumentation. The diffusion drier was custom-built using PVC and stainless steel Swagelok fittings. It consisted of two $6.35 \times 10^{-3}$ m to $1.27 \times 10^{-2}$ m bulkhead fittings at either end of a 0.1 m OD $\times$ 0.50 m long PVC capped pipe. Inside of the PVC pipe, a wire mesh screen was sewn to create a $1.27 \times 10^{-2}$ m internal diameter tube connecting both ends of the PVC pipe. Silica gel beads were placed around the mesh tubing to provide ample surface area to absorb water from the incoming particulate without blocking airflow. A more detailed drawing is shown in Fig. 2.4.

The geometry of the plumbing in Fig. 2.3b was a result of the considerable footprint of all of the instruments. Minimizing tubing length to instrumentation that measured coarse particulate was prioritized. All $6.35 \times 10^{-3}$ m plumbing fittings were Swagelok stainless steel fittings. Except for the tubing to the Lightweight Optical Aerosol Counter (LOAC; Meteomodem) and the tubing inside the manifold, all tubing was stainless steel.

All of the particle counting instruments shown in Fig. 2.3b were operated continu-

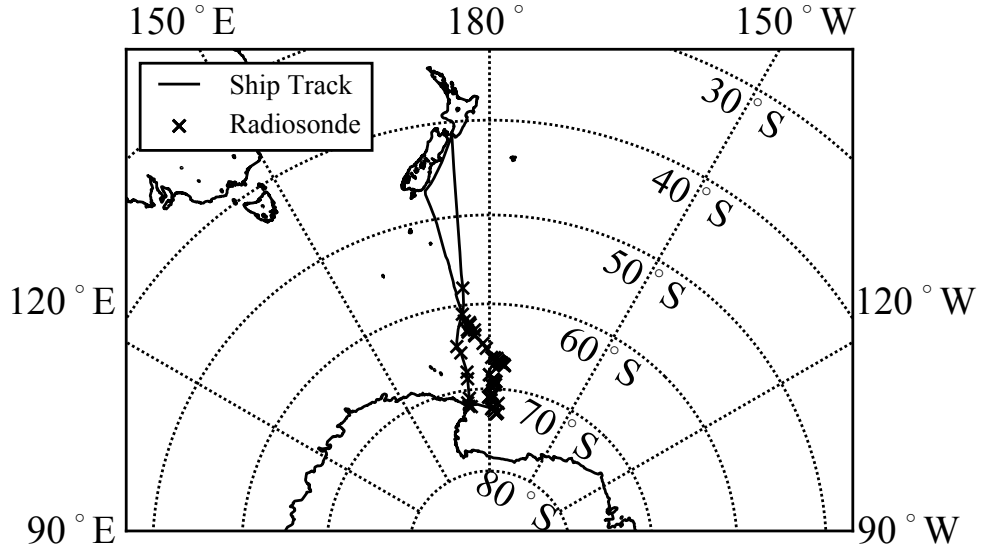


**Figure 2.2 :** The ship track for the voyage is shown. Radiosonde launch locations are indicated by $\times$ symbols.

ously throughout the voyage. While each instrument was fundamentally an optical particle counter, some instruments first manipulated the particulate by condensing vapor onto them or passing them through electrical fields. The instrumentation is suitably divided into 2 categories: condensing optical particle counters (CPCs) and pure optical particle counters (OPCs). A summary of all of the instrumentation is given in Table 2.1. Three different OPC's were operated throughout the duration of this experiment: the Passive Cavity Aerosol Spectrometer Probe (PCASP-100X; Droplet Measurement Technologies), the Lightweight Optical Aerosol Counter (LOAC; Meteomodem) and the GRIMM (GRIMM EDM 1.108; GRIMM Aerosol Technik GmbH & Co. KG). In practice the PCASP-100X was used as the best measurement of coarse particulate. The GRIMM was simply used to characterize particle losses from the main sampling conduit into the secondary sampling line. Unfortunately, the variance in data collected by the LOAC was simply too high to provide any valuable information.

**PCASP-100X**

The Passive Cavity Aerosol Spectrometer Probe is an optical particle counter designed to detect particles between 0.1 and 3 $\mu$m in diameter. The PCASP(Fig. 2.3) drew air from the main sampling conduit into its inlet at a flow rate of $1.28\times10^{-2}$ m$^3$ s$^{-1}$. Within the inlet a needle drew air into the optical cavity at a flow rate of $1\times10^{-6}$ m$^3$ s$^{-1}$. The combination of flows ensured that sampling from the main conduit was approximately isokinetic. Once inside the PCASP, sample air was hydro-dynamically focused into a particle beam by a sheath flow of $1.5\times10^{-5}$ m$^3$ s$^{-1}$. This beam shot across the optical cavity, intersecting with a 632 nm laser at the focal point of a parabolic mirror. Light scattered from the particles was first reflected by the parabolic mirror, then by a 45° flat mirror on the opposite side of the optical cavity, before finally passing through an aspheric collector, which focused the light into a photo-detector. The wide solid angle of the parabolic mirror ensured that the angular-dependent variations in scattering intensity which arise from Mie Scattering (Bohren and Huffman, 1983) were averaged out. The photo-detector operated three different particle detection channels in parallel, each of which used linear voltage amplifiers with different gain settings to raise the scattering signal to a detectable range by the counting electronics. This allowed the PCASP-100X to measure scattering intensities across six orders of magnitude. As a result, the PCASP-100X detected particles as small as 0.1 $\mu$m and as large as 3 $\mu$m. Each particle detection event was subsequently sized into one of 30 discrete bins, the

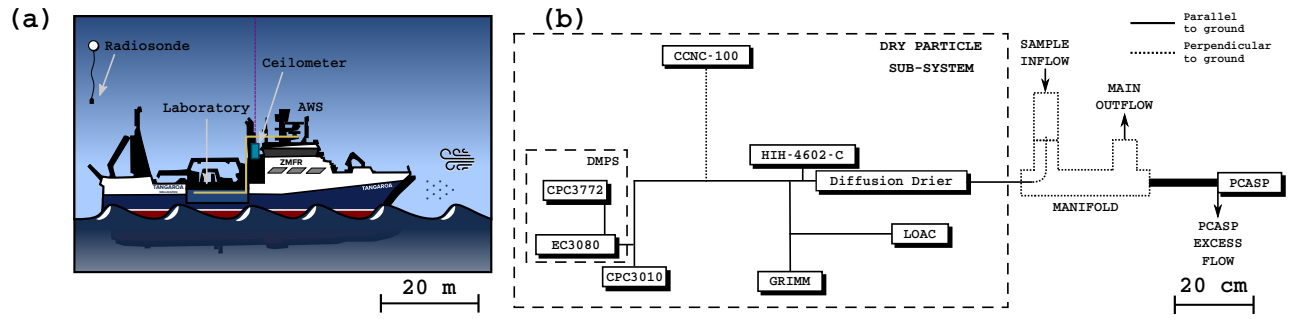


**Figure 2.3 :** (a) A starboard side diagram of the R/V *Tangaroa*. Key locations and equipment for operations throughout the voyage are named. (b) A flattened drawing of the instrument layout in the container laboratory. It shows how ambient air, drawn in from the mast, was distributed to the instruments within the container laboratory. The plumbing is drawn to scale, but the instruments are not. Dotted lines represent pieces of plumbing that extended upwards, dashed lines denote sub-systems referred to in text.

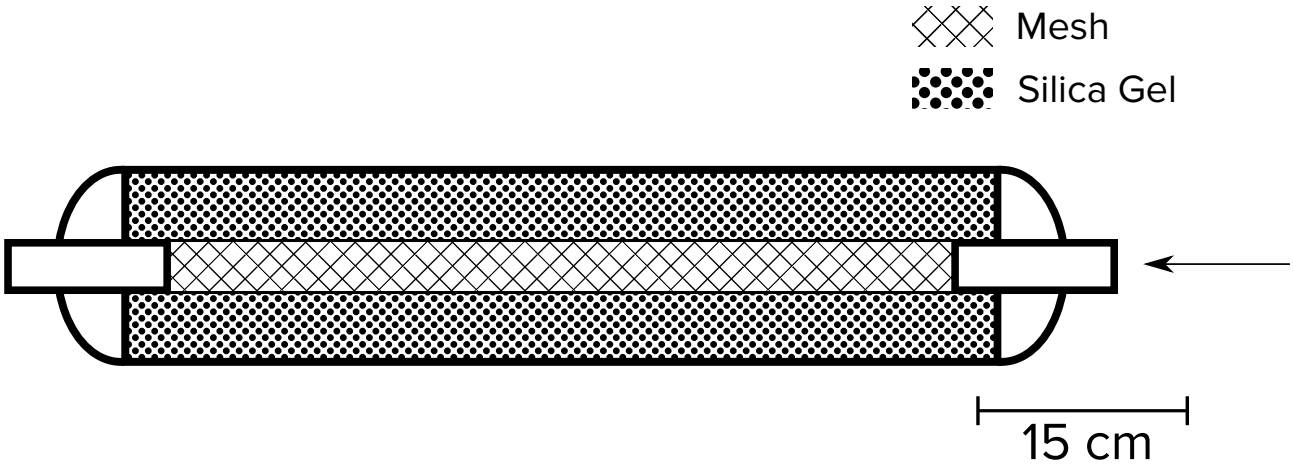


**Figure 2.4 :** The design of the diffusion drier seen in Fig. 2.3b. Particle-laden air enters from the right side, and is passed through a mesh tube with silica gel beads on all sides. A lower bound for the dry surface area can be estimated by $f\pi r^2 L$, where f is the open area fraction of the wire mesh. However, the uneven surface provided by the beads means the actual surface area is much greater.

widths of which were determined through calibration by the manufacturer. Uncertainties for particle counting instruments within a given interval are equal to the square root of the mean concentration within said interval.

**CPC3010**

The TSI CPC3010 is a condensation particle counter which measures the total concentration of particles larger than 10 nm and smaller than 3$\mu$m. The TSI CPC3010 condenses N-butanol onto all incoming particles such that they grow to a uniform size. To accomplish this, the unit maintains a steady temperature gradient between a saturation and condensation stage of 17 K. At a temperature differential of 17 K, N-butanol will condense onto particles as small as 10 nm. They rapidly grow via condensation until they reach the optically detectable range of the unit (>300 nm). Thus, the CPC3010 was used to measure the total number concentration of particles in the size range (0.01 – 3 $\mu$m). Particles with diameters larger than 3 $\mu$m were not well transported through the CPC3010 and tended to deposit onto the walls of the focusing jet before entering the optical cavity.

**DMPS**

The DMPS is a differential mobility particle size spectrometer which is nominally capable of measuring the concentration of aerosol particles larger than 10 nm and smaller than 1$\mu$m. The DMPS is composed of two separate instruments: an Electrostatic Classifier (TSI EC3071) and a CPC (TSI CPC3772). The DMPS first draws particles through a bipolar diffusion charger (BDC). A Kr-85 BDC was used, which bombarded incoming particulate with beta radiation. This electrically neutralized >90% of the incoming particles. The rest of the particles were either singly-charged or doubly-charged, the fraction of which can be readily calculated (Wiedensohler, 1988). Only a negligible fraction of particles remain multiply charged. After leaving the BDC, the mixture of charged and uncharged particles passed through a differential mobility analyzer (DMA). The DMA is simply two concentric stainless steel tubes, held at a fixed voltage relative to each other. At the end of the concentric tubes is a small inlet near the outer edge of the inner tube which connects to the CPC3772. For a fixed voltage, only a narrow range of particles have the correct diameter and charge to cross the streamlines towards the center tube at such a rate that they exit through the small opening which connects to the CPC. The rest will either cross too quickly and deposit onto the center tube, or not cross quickly enough and be filtered out by a steady sheath flow through the DMA. Over a period of 12 minutes, the voltage applied to the DMA was incremented in even logarithmically-spaced steps through the operational range (10–10 000 V). As a result, the particles entering the CPC3772 steadily increased in size (0.02–0.3 $\mu$m). Particles exiting the EC-3071 were counted by the CPC3772 over a period of 10 s, allowing 2 s between each step in voltage for particles of the previous size to be flushed through. Further data processing details are given in Subsection 3.c.

**CCN-100**

The final particle counting instrument operated on this voyage was a cloud condensation nuclei counter (CCN-100; Droplet Measurement Technologies). This instrument was similar to the other CPC's, but used water as the condensing fluid. The instrument has a sample flow of $8.3\times10^{-6}$ m$^3$ s$^{-1}$. The instrument was calibrated using ammonium sulfate to derive the required temperature of the saturation and condensation stages necessary to replicate cloud formation conditions. The instrument was set up to scan through supersaturation levels of 0.1% from 0.2–1.0%. Each level was measured for three minutes to ensure that the system had reached thermal equilibrium. The CCN-100 differs from the CPC3010 in that it provides size spectra of the humidified droplets. These highly detailed data are useful for research into the water activity of different particle species; but, for this thesis, only the number concentration of optically detectable droplets was studied.

**Table 2.1 :** A summary of the particle counting instrumentation used in the container laboratory. A spectral instrument is one that measures the number concentration in various size bins, whereas an integral instrument just gives the total number of particles within the detectable range.

| *Instrument Name* | *Manufacturer* | *Size Range* | *Spectral or Integral* | Used in thesis? |
|---|---|---|---|---|
| Passive Cavity Aerosol Spectrometer Probe (PCASP-100X) | DMT | 0.1–3 $\mu$m | Spectral | yes |
| Environmental Dust Monitor (EDM 1.108) | Aerosol Technik GmbH | 0.25–32 $\mu$m | Spectral | no |
| Lightweight Optical Aerosol Counter (LOAC) | Meteomodem | 0.2–100 $\mu$m | Spectral | no |
| Cloud Condensation Nuclei Counter (CCN-100) | DMT | variable | Integral | yes |
| Condensation Particle Counter (CPC3010) | TSI | 0.01–3$\mu$m | Integral | yes |
| Differential Mobility Particle Sizer (DMPS) | TSI | 0.02–0.3$\mu$m | Spectral | yes |

*b. Discrete Aerosol Particle Samples*

Throughout the voyage, aerosol particles were also collected onto filter paper. The particle collection assembly was located ahead of the bridge. This provided relatively consistent exposure to the uncontaminated air mass ahead of the R/V Tangaroa; however, as with the aerosol sampling line, contamination of the filter bed from ship exhaust was unavoidable. The collection assembly consisted of a rain shelter, a Pall filter holder, a single layer of 47 mm pre-sterilized polycarbonate membrane filter paper, a vacuum pump and a gas flow meter. The filter folder and filter papers were provided pre-packaged from Colorado State University. The filter holders were clamped beneath the rain shelter. The filter holder lid was then removed and the vacuum pump was turned on, leaving the quartz filter exposed to ambient air for 12–50 hours. The total volume of air which passed through the filter paper was verified with the gas flow meter. On average, 14 L $min^{-1}$ of ambient air flowed through the filters while exposed. After exposure the filter paper was removed with tweezers, inspected, packaged in a petri dish, sealed with aluminium foil, and kept in an air-tight plastic bag. The finished samples were then stored at -20°C until they could be shipped to Colorado State University for analysis.

*c. Weather & Ancillary Measurements*

Measurements of the state of the atmosphere were also collected from the NZ MetService Automated Weather Station (AWS). The AWS was positioned above the bridge of the R/V *Tangaroa* at 22.5 m asl. Relevant measurements included ambient pressure, air temperature, relative humidity, wind speed, wind direction and precipitation rate. Raw wind speeds were corrected for accelerations over the ship's structure (Popinet et al., 2004; Smith et al., 2011). From these corrected winds, the true winds were calculated from the ship's vector. Finally they were adjusted to the 10 m reference height according to the COARE 3.5 bulk flux algorithms (Edson et al., 2013). The bulk seawater temperature was also measured near the inlet of the underway seawater sampling system using a thermistor (SBE38; Sea-Bird Scientific). The inlet for the seawater sampling line is located at a depth of 5.5 m below the waterline of the R/V *Tangaroa*. Generally, differences between the bulk temperature and skin temperature are less than 1 K (Schluessel et al., 1990). The bulk temperature is the average temperature of water in the upper 10 m of the ocean column (exact depth varies depending on study), while the skin temperature is the temperature of the ocean surface inferred from infrared measurements (Schluessel et al., 1990). To determine the sea surface temperature from the bulk temperature, the COARE algorithm simply subtracted 0.3 K from the bulk temperature (Edson et al., 2013).

*d. Ceilometer Data*

A CHM-15K ceilometer was operated from just behind the bridge (see Fig. 2.3). The ceilometer measured the reflectivity of the overlying atmosphere by sending 1064 nm laser pulses at 5 kHz directly upward. The intensity of the reflected light from cloud, precipitation, particulate and even molecules, is then detected back at the instrument. The speed of light being well known, the time since a pulse is sent, to when a laser pulse is received, is used to discretize the back-scattered intensity into height bins, 15 m high. The raw laser power reflected back to the instrument is then divided by the square of this distance to account for laser width divergence as a function of altitude. Finally, a system calibration coefficient is then used to convert the back-scattered intensity into a measure of attenuated backscatter. System algorithms are then applied to these profiles to derive cloud base height. Additional quality control flags are provided by the instrument which inform the user if there is precipitation on the outer optical window, there is precipitation ongoing, or if there is fog. Uncertainties in the raw backscatter signal are equal to the square root of the

mean. The background-corrected and range-corrected "attenuated backscatter" signal has an additional uncertainty related to the variation in the background.

*e. Radiosondes*
Radiosondes (iMet-1 ABx; Intermet) were launched approximately twice daily from the stern of the ship. The radiosonde package contained a radio transmitter, bead thermistor, thin polymer humidity sensor, solid state pressure sensor and a 12 channel GPS transceiver. The sensors were attached to weather balloons (KCL-150; Kaymont) with low-weight string and a string un-winder. When launched, the string around the un-winder would loosen, allowing the radiosonde to fall 10 m below the balloon. This prevented measurement issues within the balloon wake, but also prevented tangles around the ship frame during launch. The weather balloons were inflated with technical grade helium (99.9%; BOC) until they could adequately lift a reference weight. This guaranteed an ascent rate of 3–5 m $s^{-1}$. The balloons typically burst near 17 km, sending a data packet (P, T, RH, Latitude, Longitude) every second until then. Wind speeds were calculated from the time-series of the GPS locations. The launch locations for the radiosondes are pictured in Fig. 2.2.

# 2. Quality Control

*Intrusions of Ship Exhaust*
As the ship was the sole source of anthropogenic particulate in the region, it was necessary to screen the measurements for contamination by ship exhaust. Co-incident to the inlet of the sampling conduit in Fig. 2.3 was an air inlet for a cavity ring-down spectrometer (CRDS; Picarro G2301), which measured mole fractions of $CO_2$, $CH_4$, and $H_2O$. A mole fraction of 405 ppm $CO_2$ was used as a threshold detection limit for sample contamination by ship stack emissions. This threshold was chosen as it was well above the primary trend line for [$CO_2$]. Measurements from the particle counting instruments were removed if the contamination flag was raised.

*Counting Uncertainties*
Poisson counting statistics were also leveraged to provide quality control on the raw measurements. Poisson counting statistics state that the standard deviation of a count is equal to the square root of the number of items counted. As an example, the PCASP-100X data were available at a temporal resolution of 1 Hz. However, in just 1 second, very few particles were in any of the size bins, resulting in large standard deviations relative to the measured value. To improve this, the PCASP-100X spectra were averaged over one minute intervals. Then, the standard deviation of the 1 Hz sub-samples for each of these minute averages was calculated. When the standard deviation exceeded Poisson counting statistics ($\sigma_N > 1.5\sqrt{N}$), the minute average was discarded. These samples tended to occur shortly after ship stack emissions had entered the sampling conduit, since it took several seconds for the pollution to be purged from the line.

*Checking for Leaks*
Part of setting up and maintaining an air sampling system is routinely checking for leaks. Every two days, the dry particle sub-system was disconnected from the main sampling conduit (see Fig. 2.3), and connected to a total particle filter. With all of the instruments running, this slowly removed any particulate from the sample line. In all cases, concentrations of particulate measured by all instruments tended towards zero, with measurements from the CPC3010 being no more than 1–2 counts per second. As part of this testing, the voltage of the DMA was set to 10 V, such that only the smallest particles could be detected by the DMPS. Since the smallest particles are the most gas-like, they are the most likely to pen-

etrate into the tubing, even for small leaks. However, on February 25, the voltage across the DMA was accidentally left at 10 V after the scheduled maintenance was completed. As a result, no particle spectra were measured by the DMPS system between 25–27 February. This maintenance did not rule out the possibility of leaks forming in the sampling manifold. However, it was impractical to test for this.

A mass flow meter (TSI 4140) was periodically used to measure the total flow entering the dry particle sub-system. This measurement verified that the total flow through the dry particle sub-system was equal the sum of the flow through each instrument, within 10%.

*Unrealistic Measurement Variability from the CPC3010*
About halfway through the voyage, the measurements from the CPC3010 began changing erratically. To diagnose the issue, a total particle filter was placed on the inlet of the unit. While the unit would periodically report very low concentrations, it would randomly ramp up to unreasonable concentrations. It was concluded that the particle beam dump in the optical cavity had become dislodged. The beam dump prevents the laser from firing directly into the photodiode. Minor misalignments from vibrations and tilting at sea can dislodge the laser beam dump, leading to artificial particle counts. Despite this, the CPC was left in place, such that the flow through the system remained unchanged. However, the latter part of the time series from this instrument was discarded (March 1 $^{st}$ onward).

*Gain Stitching Errors in the PCASP-100X*
Within the raw measurement data collected by the PCASP-100X there was a systematic over-abundance of particles classed into bin 5 relative to bin 6. This resulted from a stitching error between the first and second gain channels, which should overlap in this size range. This was fixed by redefining bin 4 to be the width of bin 4 and 5, adding in the counts for both channels, and removing bin 5. Bin 0 was also flagged, as the lower bound of particles detectable in this bin is not well characterized; thus, particles smaller than 100 nm are often counted by the instrument, leading to an over-estimation of particle abundance in this size range. Particle number concentrations were then calculated by dividing the number of detected particle events by the sample flow rate and integration time.

*Obscuration of Particles*
As particles are continually passing through the laser of an optical particle counter, there will always be some chance of a smaller particle being obscured by a larger particle. At high particle concentrations, this could lead to significant under-counting. The manual of the CPC3772 estimates the degree of under-counting by the following relation:

$$\begin{aligned} N_a &= N_m exp^{N_a Q \tau} \\ N_a &= -\frac{\mathcal{W}(-N_m Q \tau)}{Q\tau} \end{aligned} \tag{2.1}$$

where $\mathcal{W}$ is the Lambert-W function, $N_a$ is the actual concentration of particulate, $N_m$ is the measured concentration, $Q$ is the sample flow rate, and $\tau$ is the effective time particles spend in the sample volume. According to Eq. (2.1), obscuration is less than 6% for particle concentrations of $1 \times 10^4$ cm$^{-3}$. Note that as concentrations of this magnitude were rarely encountered, the measurements have not been corrected to account for obscuration.

*Efficiency of the Diffusion Drier*
As indicated in Fig. 2.3b, relative humidity and temperature were measured just after the diffusion drier using a Honeywell HIH-4602-C sensor. The relative humidity of the air sample remained lower than 50% throughout the measurement period and was always lower

than the ambient relative humidity. While the diffusion drier did help to keep this below 20% initially, this weakened over time as the silica gel beads saturated. However, since the RH remained below 50%, and since the efflorescence relative humidity of sodium chloride is very close to 50% (46.2%), it seemed unnecessary to periodically re-dry the diffusion drier beads, which would have resulted in regular interruptions to the measurement time series.

*Calibration Drift in the CCN-100*
The CCN-100 must be carefully calibrated such that the temperature differences in the condensation and saturation stages faithfully reproduces the full spectrum of superaturations particles might encounter in a cloud. This calibration can drift over time, so it is prudent to calibrate the instrument before and after a measurement campaign. The calibration procedure is as follows: first, the CCN-100 is set to create a fixed temperature difference between the saturation and condensation stages of the cloud chamber. At the same time, an atomizer is supplied with a positive pressure to generate aerosol from a dilute solution of ammonium sulfate. The hydrated particles that form the aerosol are then passed through a diffusion drier to remove any moisture from the particulate. These particles are subsequently passed through the electrostatic classifier. The classifier scanned through the range of voltages, such that the outgoing particulate were monodisperse at any given time. From the electrostatic classifier, the CPC3772 and the CCN-100 measured the total number of particulate and the total number of CCN, respectively. The fraction of cloud-activated particulate, f, can be described by a logistic-like curve as a function of particle diameter, $D_p$:

$$f \equiv \frac{N_{CCN}}{N} = \frac{1}{1 + \left(\frac{D_p}{D_{p,c}}\right)^{-\beta}} \tag{2.2}$$

where $D_{p,c}$ is the critical diameter for which 50% of the particles activate and $\beta$ is a parameter that describes the steepness of the logistic curve. Once the the critical diameter is estimated, $\kappa$-Köhler theory can be used to retrieve the supersaturation, $S_c$ from the following equation (Petters and Kreidenweis, 2007):

$$\ln^2(S_c) = \frac{1}{2\kappa}\left(\frac{8\sigma M_w}{3RT\rho_w D_{p,c}}\right)^3 \tag{2.3}$$

Where $\kappa = 0.61$ is the hygroscopicity of ammonium sulphate, $\sigma = 0.072$ J m$^{-2}$ is the surface tension of water, $M_w = 0.018$ kg mol$^{-1}$ is the molecular weight of water, R is the universal gas constant, T is the ambient temperature in degrees Kelvin, and $\rho_w = 997$ kg m$^{-3}$ is the density of water.

The calibration activation curves, and their fit to Eq. (2.2), are shown in Fig. 2.5. Note that the small hump in each scan which precedes the transition to full activation is a result of doubly-charged particles from the BDC. By performing this analysis for several system temperature differences, a calibration curve can be obtained (see right-hand side of Fig. 2.5). Overall, the drift in calibration was small, with supersaturation set values of 0.2 and 0.3% drifting the least throughout the experiment. The calibration drift is only provided as a measure of quality control as it was not used to correct the data.

# 3. Data Processing

*a. Relative Humidity*
It is also well-known that the size of hygroscopic particles can vary significantly as a function of relative humidity. To remove shifts in the particle size distribution that result from variations in relative humidity, all size spectra were corrected to 80% relative humidity.

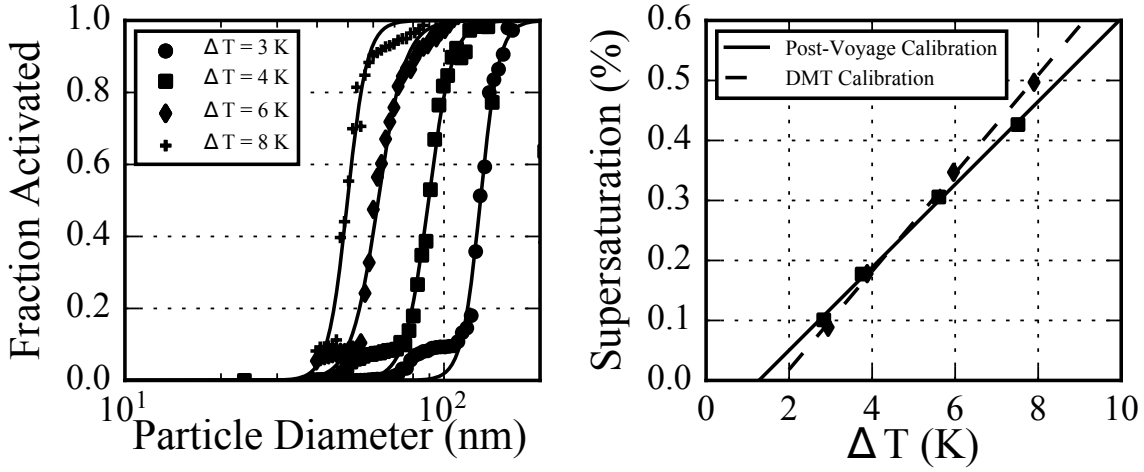


**Figure 2.5 :** (left) The fraction of activated ammonium sulfate particles observed by the CCN-100 as a function of particle diameter. The lines represent fits to Eq.( 2.2) for different cloud chamber temperature differentials in the CCN-100. (right) The calibration curve after the voyage is compared to the manufacturer's calibration pre-voyage.

This was accomplished using a parameterization of the hygroscopic growth of sea spray and sulfate particles (Gerber, 1985):

$$\begin{aligned} r &= \sqrt[3]{\frac{c_1 {r_d}^{c_2}}{c_3 {r_d}^{c_4} - log(S)} + {r_d}^3} \\ c_1 &= 0.7674 \\ c_2 &= 3.079 \\ c_3 &= 2.572 \times 10^{-11} \\ c_4 &= -1.424 \end{aligned} \tag{2.4}$$

where $S$ is the saturation ratio of water vapour, $c_1 - c_4$ are empirical parameters and $r$ and $r_d$ are the hydrated and dry particle radius, respectively. This was more important for size spectra from the PCASP-100X, since these particles were not dried before measurement. The temperature difference between the container and the PCASP-100X likely removed some water from the particulate. However, a relative humidity sensor was not connected to the inlet of the PCASP-100X, so it was assumed that the particles were at ambient humidity. In contrast, sample air in the dry particle sub-system was typically below the deliquescence point of sea spray and sulfate, so a voyage-wide size correction could be applied. Note that data provided in Kremser et al. (2020) has not been corrected according to RH.

*b. Sampling Efficiency*

In any sampling conduit, particle losses are inevitable. To make statements about the true ambient particle size distribution, it is necessary to correct for these losses. In estimating particle losses, calculations described in Chapter 6 of 'Aerosol Measurement' (Brockman, 2001) were followed. These calculations describe sampling losses due to: wind speed, wind direction, inlet orientation, diffusion, turbulence, gravitational settling, and sampling conduit geometry (bends, constrictions, diameter).

The sampling conduit was modeled as a 40 m long horizontal tube with three main turns (two are visible in Figure 2.3) and one sharp right turn within the sampling manifold. This ignores the fact that the sampling conduit was vertical in some sections. However, gravita-

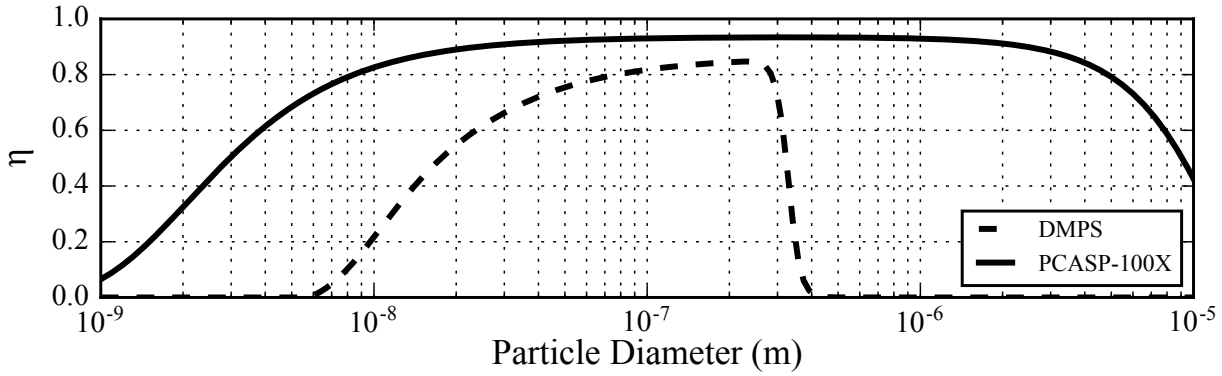


**Figure 2.6 :** The fraction of ambient particles which are successfully transported through the main sampling conduit is shown as a function of particle diameter. This was calculated according to the geometry of the sampling conduit and equations in Brockman (2001).

tional losses in vertical tubing are zero and all other losses are unchanged, so this calculation represents a worst-case scenario. This also ignores slight constrictions in the tubing from bending around elements of the ship's frame. However, the tubing used was relatively rigid, so any constrictions were small. Finally, the tubing was embedded with a copper wire, so it was assumed that there was no buildup of static charge on the exterior of the line. As a result, there were likely no particle losses from electrostatic deposition.

The flow through the main sampling conduit was provided by two pumps: a primary pump, which provided a flow of $2.64 \times 10^{-2}$ m$^3$ s$^{-1}$, and a secondary pump providing an additional $1.28 \times 10^{-2}$ m$^3$ s$^{-1}$ of flow. This resulted in a net flow of $3.92 \times 10^{-2}$ m$^3$ s$^{-1}$ through the sampling conduit. Assuming the velocity field approximately followed Hagen-Poiseuille's law, this provided a mean gas velocity of 5 m s$^{-1}$ and a flow Reynold's number of 32, 400: evidently well into the turbulent regime. The total transit time of the particles through the sampling conduit was 8 s.

The inlet of the tube was restrained to face slightly downwards in order to avoid accumulation of precipitation in the inlet line. The inlet thus made an angle of -45° from the plane of the ship. However, winds were largely parallel to the ocean surface. As a result, sampling was always anisoaxial. Additional sampling losses in the inlet region came from: aspiration inefficiency and inertial impaction with the vena contracta. Throughout the remainder of the transport to the container laboratory, particles could deposit onto the tube walls as result of gravitational settling, bends, sharp turns, turbulent inertial deposition, and diffusion.

Figure 2.6 shows the total sampling efficiency for the PCASP-100X, $\eta$, for standard atmospheric temperature and pressure, with ambient winds of 5 m s$^{-1}$. Since the inlet was so

**Table 2.2 :** Reference equations from Baron and Willeke (2001) (B+W) that were used to calculate the sampling efficiency are summarized.

| Loss | Anisoaxial Aspiration Inefficiencies | Collision w/ Vena Contracta | Gravitational Settling |
|---|---|---|---|
| Equation | (B+W; 8-20) | (B+W; 8-25) | (B+W; 8-54) |
| Loss | Wall Collisions in Bends | Wall Collisions in Turns | Wall Collisions from Turbulence |
| Equation | (B+W; 8-68) | (B+W; 8-66) | (B+W; 8-61) |
| Loss | Wall Collisions from Diffusion | Losses in a CPC | Losses to an Impactor |
| Equation | (B+W; 8-56) | (Hermann et al., 2007) | (B+W; 8-3) |

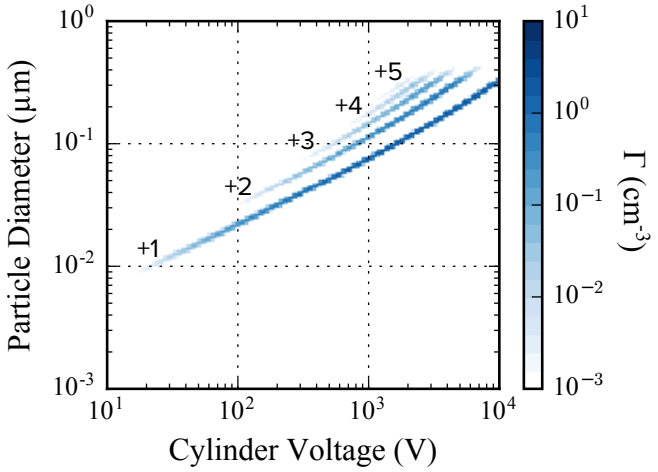


**Figure 2.7 :** The modelled instrument response matrix Γ is shown for 256 particle diameter bins for an example even voltage scan of 256 voltages from 1 to 10,000V. The different lines in Γ correspond to particles with increasing number of charges.

wide, the Stokes numbers for the relevant particle sizes were small ($<1\times10^{-2}$). As a result, losses from anisokinetic effects were very low. The largest losses were due to diffusion, inertial impaction with walls and the vena contracta in the inlet region, bends in the tubing, and gravitational losses. The equations used to estimate Figure 2.6 are listed in Table 2.2.

Finally, the ambient particle number–size spectrum, $N_a$ can be calculated from the sampled number–size spectrum, $N_s$ by simple inversion:

$$N_a = \frac{N_s}{\eta} \tag{2.5}$$

Which is applicable to almost all of the particle counting instruments. However, additional losses were encountered within the DMPS. Diffusional losses within the BDC, the EC3071, and the diffusion drier are all substantial. While the additional pipe length from the sample manifold to the DMPS is only 1 m, the effective diffusional length of the BDC, EC3071 and diffusion drier combined is 13 m (Wiedensohler et al., 2012). These diffusional losses are calculated exactly as in the sampling conduit, but with the effective diffusional length rather than the true length. The CPC3772 and CPC3010 have additional losses, too, and only efficiently measure particulate larger than 10 nm (Hermann et al., 2007). Additionally, an impactor was placed in front of the EC3071 which prevented large particles from entering the system. Large particles are more likely to be multiply-charged (Gunn, 1955; Wiedensohler, 1988), which complicates the DMPS sampling procedure and can lead to false counts in smaller bins. The losses from these elements were multiplied through with the losses in the sampling conduit to estimate the total sampling efficiency of the DMPS. This curve is shown in Figure 2.6.

*c. Inverting the DMPS Data*

The reconstruction of the fine particle size spectrum from DMPS measurements is a relatively complicated procedure. While the electrostatic classifier reports a particle diameter for each voltage setting, this is only the predicted diameter for singly charged particles at that voltage. The particles exiting the BDC can actually have multiple charges. As the particle diameter increases, so does the probability that a given particle could have multiple charges (Gunn, 1955; Wiedensohler, 1988). To compensate for this, an inversion methodology must be applied.

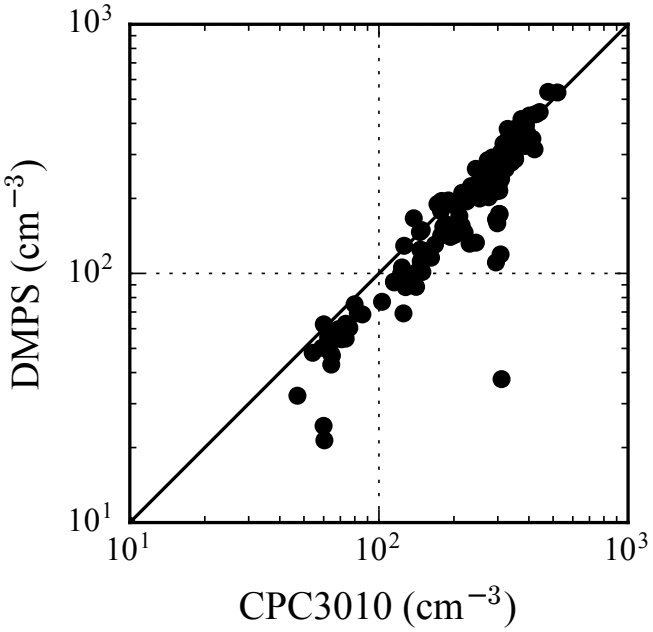


**Figure 2.8 :** The total number concentration of particles observed by the DMPS is compared the number observed by the CPC3010.

The first step in the inversion is to define the size resolution of the retrieved size spectra. A set of 256 diameters logarithmically-spaced between 10–500 nm, $d_{p,j}$ was chosen. The probability, *f*, that a particle will have a charge of $\phi$ was calculated according to Gunn (1955), along with ion mobilites and thermal velocities from Wiedensohler et al. (1986). Since the window of particle diameters that are able to transfer through the classifier is not infinitely sharp, the instrument transfer function, $\Omega$ also needs to be approximated. In theory, the number of particles, *C*, that will be observed by the CPC3772 when the EC3071 is set to a voltage, V, can be calculated from (Stolzenburg, 1988):

$$C = \int_0^\infty \left[ \frac{\mathrm{d}n}{\mathrm{d}\log(D_p)} \, Q \, \eta \, \Delta t \sum_{\phi=-\infty}^{\infty} f(D_p, \phi, T) \Omega(D_p, \phi, Q, Q_s V, P, T) \right] \mathrm{d}\log(D_p) \tag{2.6}$$

where $\mathrm{d}n(\mathrm{d}\log(D_p))^{-1}$ is the ambient particle number–size spectrum, *Q* is the inlet flow rate, $Q_s$ is the sheath flow rate, $\Delta t$ is the counting integration time, $\eta$ is the efficiency in Fig. 2.6, $\phi$ is the number of charges, *P* is the ambient pressure, and *T* is the temperature in column (Brockman, 2001). The narrowness of the transfer function depends mostly on the ratio of the inlet and sheath flow rates, where a high sheath-to-inlet flow results in an extremely narrow transfer function.

The outer integral of Eq. (2.6) is discretized into 256 bins and re-formulated in matrix notation as:

$$C = \Gamma N \tag{2.7}$$

Where, $\Gamma$ is the instrument response matrix, and *N* is the particle number–size spectrum across the diameter space. The probability that an incoming particle will have more than five charges is quite small, so the sum was limited to just the first five positive charges. The value of the transfer function for particles with zero or negative charges ($\phi \leq 0$) is zero. The response matrix, $\Gamma$, can then be defined as follows:

$$\Gamma_{i,j} = Q \, \eta \, \Delta t \log\left(\frac{d_{p,j+1/2}}{d_{p,j-1/2}}\right) \sum_{\phi=1}^{5} \bar{f}(d_{p,j}, \phi) \Omega(d_{p,j}, V_i, \phi) \tag{2.8}$$

**Measurement**

1. Multiply EC-3080 voltage by factor: f
2. Measure voltage
3. Integrate CPC3772 particle counts
4. If V≥10000V
   f = 1/f
   If V≤10V
   f = 1/f
5. Repeat

**Inversion**

6. Define n voltage bins evenly spread from 10-10000 V in log-space.
7. Define m particle size bins evenly spread from 10-500 nm
8. Calculate Γ as an nxm matrix
9. Sort particle counts, C, into the n voltage bins.
10. Apply LSMR algorithm to retrieve spectra N.

**Smoothing**

11. $X = \frac{C}{\Gamma \cdot N}$
12. $N = (1 + (X - 1) \cdot \Gamma) \circ N$
13. Apply moving geometric mean to N
14. Repeat

**Figure 2.9 :** Pseudo code for measuring, processing and smoothing retrieved particle size spectra from the DMPS. The inversion step discretized pairs of measured voltages and particle sub-counts into the voltage array. The median of each bin was retained for the inversion. Inversion and smoothing took place after the voyage had concluded. Smoothing steps 11 and 12 are Twomey's algorithm (Twomey, 1975).

where,

$$d_{p,j\pm1/2} = \sqrt{d_{p,j} d_{p,j\pm1}} \tag{2.9}$$

The resulting transfer matrix is visualized in Fig. 2.7.

To solve Equation 2.7, the raw DMPS measurements were first sorted into 1000 sequential 1-hr bins over the duration of the experiment. Then, the particle sub-counts and voltages were discretized into 256 bins by voltage from 10–10,000V. In each voltage bin, only the median number of particles observed was retained. This provided a measure of quality control by ignoring really high counts (from ship exhaust) and really low counts (from lack of N-butanol). Sorting in this way also provided a common basis of voltages across the entire time series. Hence, the response matrix, Γ, only needed to be calculated once. Finally, the number concentration size spectra were calculated by inverting Equation 2.7. The inversion was accomplished with an implementation of the LSMR algorithm in SciPy. The LSMR algorithm is designed for solving least squares problems with sparse matrices (Fong and Saunders, 2011), like Γ. However, the spectra, N, retrieved from inverting Equation 2.7 were still quite noisy. To retrieve a smoother signal, a variant of a smoothing algorithm for mobility size spectra was applied (Markowski, 1987). This algorithm is an adaptation of Twomey's algorithm (Twomey, 1975), which inserts a moving averaging step after the adjustment step. However, the geometric mean was used instead of the arithmetic mean. This better preserved the shape of the distribution in log space in between iterations of Twomey's algorithm. An outline of the measurement, inversion and smoothing steps is presented in Fig. 2.9.

The total number concentration from the retrieved spectra is compared to the total concentration observed by the CPC3010 in Fig. 2.8. The comparison was restricted to times when the CPC3010 was functioning correctly (before March 1st). Overall, the correlation was high ($R^2$ = 0.85) with no appreciable bias. Total number concentrations calculated from the DMPS that were much smaller than measured by the CPC3010 occurred when the CPC3772 was running out of N-Butanol. This was a recurring issue with the system. The constant motion of the boat forced the CPC3772's liquid-level sensor to trigger that

the reservoir was full. This closed the ball-valve between the fill bottle and the instrument reservoir. A software patch was implemented to force the ball valve open every 30 minutes while keeping a bottle full of N-Butanol connected to the reservoir at all times. The majority of scans where this was an issue were masked by taking the median of all of the discretized scans within an hour in the inversion step; however, a few remained.

# 4. Modelling

*a. AMPS*

To contextualize the measurements made during the Marine Ecosystem and Environment Voyage, two primary modelling tools were used. The first such tool was meteorological output fields from the Antarctic Mesoscale Prediction System (AMPS) (Bromwich et al., 2005). AMPS is fundamentally based on the Advanced Weather Research and Forecasting model (WRF); however, it includes more detailed parameterizations for polar climates than are available in the standard version of WRF. The model is initiated using initial and boundary conditions for the state of the atmosphere from NCEP GFS, sea surface temperature and sea ice data from NSIDC. The model then predicts the evolution of the atmosphere at several nested spatial and temporal resolutions. AMPS initializes a new forecast every twelve hours. However, in this work only meteorological forecasts at +03, +06, +09, and +12 hours after initialization were used. This helped avoid initialization biases relative to the rest of the forecast (Jolly et al., 2016). In addition, only the outermost spatial domain, d01, was studied, as the higher resolution domains were specific to Antarctica and did not adequately represent the Southern Ocean. Within this domain, AMPS provides meteorological predictions at 3 hour resolution, 24 $\times$ 24 km horizontal resolution, and 60 $\eta$ levels between the surface and 10 hPa. $\eta$ levels are a hybrid coordinate system which defines altitude according to pressure and surface topography. A complete overview of AMPS is provided in Bromwich et al. (2005), though the configuration has changed considerably since. Data used in this thesis were downloaded from `https://www.earthsystemgrid.org/project/amps.html`.

*b. FLEXPART-WRF*

The second modelling tool used extensively throughout this thesis was the Lagrangian particle dispersion model, FLEXPART-WRF (Brioude et al., 2013). FLEXPART-WRF was used to predict the air mass history of our in situ measurements. Air mass history calculations estimate the path through which aerosol particles, or gasses, are transmitted through the atmosphere to the point of measurement. Air mass history can thus be used to identify where and when an airborne contaminant (particulate, gas), was emitted into the atmosphere. FLEXPART-WRF characterized the air mass history of our in situ measurements by simulating the dispersion of model aerosol particles in reverse time through meteorological fields. As indicated by the acronym, the model ingests meteorological output from WRF to predict air mass history. In this case, the meteorological output was provided by the AMPS forecasts introduced earlier.

The dispersion of the particles through the atmosphere is predicted according to the local wind velocity. Reynold's decomposition can be used to break down the wind velocity into its mean and fluctuating components:

$$v = \overline{v} + v_t + v_m \tag{2.10}$$

Where $\overline{v}$ is the mean velocity of the wind, $v_t$ is a perturbation due to turbulence, and $v_m$ is a perturbation which accounts for mesoscale variability in wind. FLEXPART-WRF reads the mean velocity, $\overline{v}$, directly from the AMPS meteorological forecasts. The model then uses the

Langevin equation to calculate both $v_t$ and $v_m$:

$$\frac{\mathrm{d}v_x}{\mathrm{d}t} = a_x + b_x \mathrm{d}W \tag{2.11}$$

Where $a_x$ and $b_x$ are terms which characterize the acceleration and the strength of the diffusive process (respectively), d$t$ is the time-step, and d$W$ is a random stochastic variable with zero-mean, and unit variance (Stohl et al., 2005). In the case of the turbulent wind fluctuations ($v_t$) $a_t$ and $b_t$ are parameterized according to the planetary boundary layer height, Monin-Obukhov length, convective velocity scale, roughness length and friction velocity. For the mesoscale wind fluctuations ($v_m$) $b_m$ is a function of the gridscale variability in wind, i.e. the model assumes that the variability of winds within nearby grid cells is the same as the variability within a given grid cell. Complete simulation details are provided in Chapter 3.

The key output variable provided by FLEXPART-WRF is the grid-cell residence time, which tracks the total amount of time that a particle spends within a given grid-cell during a meteorological time step. As demonstrated by Seibert and Frank (2004), the grid-cell residence time constitutes a source-receptor relationship between the airborne concentration of a substance measured at the initialization point of the air mass history calculation, $N(x_0, y_0, t_0)$, and the volumetric flux of that substance from a given grid cell along the back trajectory, $F(x, y, z, t)$. However, the particle concentration is not necessarily preserved along the Lagrangian path. Along the trajectory, the particles may be subjected to dry deposition (e.g. gravitational settling) or wet deposition (e.g. rain-out or cloud activation) depending on the meteorological forecasts. As the length of time a particle spends within a grid-cell dictates the amount of particulate lost to a given mechanism (dry or wet deposition), FLEXPART-WRF scales the residence time according to the strength of the loss mechanisms:

$$\mathrm{d}\mathcal{P} = \frac{M}{M_0}\mathrm{d}t \tag{2.12}$$

Where d$\mathcal{P}$ is the scaled residence time, $M$ and $M_0$ are the time-dependent and initial mass concentrations of the particle, and d$t$ is the time step. Note that $M_0$ is arbitrary as it scales the time-dependent mass, $M$. It is nominally set to a value of 1. When the time-dependent mass decreases past a certain threshold value, the simulation is terminated. In such a case, the air mass history is considered to be completely characterized.

If the flux, $F$, of a quantity is known then the concentration, $N$, at the receptor $(x_0, y_0, z_0, t_0)$ can be estimated according to the following equation:

$$N(x_0, y_0, z_0, t_0) = N_0 + \int_{t_f}^{t_0} \iiint_A F(x, y, z, t)\mathrm{d}x\mathrm{d}y\mathrm{d}z\mathrm{d}\mathcal{P} \tag{2.13}$$

where $N_0$ is the background concentration, $t_f$ is some time prior to the observation time $t_0$, and $A$ denotes that the integral is taken over the entire atmosphere. This equation is simplified by the following observations. First, we are not concerned with the volume flux of airborne contaminants throughout the entire atmosphere. This thesis is interested in the interfacial flux of sea spray particles into the atmosphere. We also assume that the simulation is sufficiently long, such that the residence time of particles within grid-cells beyond the simulation time is too small to affect the predicted concentration at the receptor point ($\|\frac{dN}{dF}\| \sim 0$). Then, assuming the flux is well-mixed into a boundary layer of minimum

depth, $h$, equation 2.13 becomes:

$$N(x_0, y_0, z_0, t_0) = \frac{1}{h} \int_{t_f}^{t_0} \iint_{O} F(x, y, t) \mathrm{d}x\mathrm{d}y\mathrm{d}\mathcal{P} \tag{2.14}$$

Where $O$ denotes that the integral is taken over the ocean surface. To increase confidence in the back-trajectory calculations, 100 000 particle back trajectories are calculated for each observation point. Equation 2.13 is then calculated using the ensemble average of the residence time over all of the independent particle back trajectory simulations.

# 5. Summary

In this chapter, particle counters, discrete samples of particles collected on filter paper, aerosol backscatter measurements, meteorological data, and radiosonde deployments were described. The principals of measurement were outlined and relevant aspects of quality control and data processing were discussed. In following the procedures described in this chapter, a high quality data set has been produced. In this thesis, the data set described in this chapter will be used to characterize the abundance of particulate within the Southern Ocean boundary layer and the mechanisms through which those particles are transferred to, and subsequently activated within, the cloud layer. The data collected on this voyage, along with many other measurements from collaborators, are available via Zenodo, `https://zenodo.org/record/4060237#.X70Z1GhKjIU`. An accompanying manuscript detailing the data set is forthcoming (Kremser et al., 2020).

As described in this chapter, the in situ observations will also be supplemented with a characterization of the wider Southern Ocean atmosphere as predicted by AMPS. In addition, air mass history calculations from FLEXPART-WRF will be exploited to understand the origin of the particles observed throughout the Marine Environment and Ecosystem Voyage. Combined, the measurements and modelling techniques described in this chapter create a robust framework for understanding aerosol-cloud interactions.

# Constraining the Surface Flux of Sea Spray Particles from the Southern Ocean


## Abstract

*Modeling the shortwave radiation balance over the Southern Ocean region remains a challenge for Earth system models. To investigate whether this is related to the representation of aerosol-cloud interactions, we compared measurements of the total number concentration of sea spray generated particles within the Southern Ocean region to model predictions thereof. Measurements were conducted from a container laboratory aboard the R/V Tangaroa throughout an austral summer voyage to the Ross Sea. We used source–receptor modeling to calculate the sensitivity of our measurements to upwind surface fluxes. From this approach, we could constrain empirical parameterizations of sea spray surface flux based on surface wind speed and sea surface temperature. A newly tuned parameterization for the flux of sea spray particles based on the near-surface wind speed is presented. Comparisons to existing model parameterizations revealed that present model parameterizations led to over-estimations of sea spray concentrations. In contrast to previous studies, we found that including sea surface temperature as an explanatory variable did not substantially improve model–measurement agreement. To test whether or not the parameterization may be applicable globally, we conducted a similar regression analysis using a database of in situ whitecap measurements. We found that the key fitting parameter within this regression agreed well the parameterization of sea spray flux. Finally, we compared calculations from the best model of surface flux to boundary layer measurements collected onboard an aircraft throughout the Southern Ocean Clouds, Radiation, Aerosol Transport Experimental Study (SOCRATES), finding good agreement overall.*


## 1. Introduction

In the remote boundary layer of the Southern Ocean, continental sources of particulate matter such as black carbon, terrestrial monoterpenes, dusts, and pollen contribute very little to the population of suspended particulate (Murphy et al., 1998). As a result, the magnitudes of the direct and indirect shortwave radiative effects from the suspended particulate within the region are largely driven by local, marine sources (Carslaw et al., 2013; McCoy et al., 2015). There has been a considerable amount of work in recent years to understand the excess of shortwave radiation reaching the ocean surface in the Southern Ocean within climate-chemistry models (CCMs), especially regarding the representation of clouds within these models (Trenberth and Fasullo, 2010; Bodas-Salcedo et al., 2014). Since hygroscopic particulate matter are a necessary precursor to cloud formation, they can indirectly exert a substantial influence on the radiation balance through modification of cloud brightness (Twomey, 1977) and cloud phase through the availability of ice nuclei (DeMott et al., 2010).

The natural sources of airborne particles in the region are the production of sea-spray generated particles (SSPs) from wind–wave interactions and ultra-fine particles from the homogeneous nucleation of sulfuric acid and other volatile vapours. However, the rate of

production of SSPs remains an open problem: the number of particles entering the atmosphere of a given droplet size and at a given wind speed has been shown to vary by over an order of magnitude among existing parameterizations for the production of SSPs (Ovadnevaite et al., 2014). If one also accounts for the uncertainties related to predicting the dependence of the surface flux on the wind speed over the water, estimates for the intensity of the surface flux diverge further. As a result, both the concentration and seasonal cycle of SSPs remain poorly constrained in the Southern Ocean (Henzing et al., 2006; Revell et al., 2019). Several studies have shown that the lack of prediction accuracy for the flux of SSPs results in large biases between observed and modelled mass concentrations of SSPs in the marine boundary layer (MBL), particularly in regions with cold waters (Jaeglé et al., 2011; Grythe et al., 2014; Witek et al., 2016).

In general, sea spray is the dominant source of particulate matter in the Southern Ocean in terms of mass (Murphy et al., 1998); however, during ice formation in coastal Antarctica, wind-blown frost flowers and snow from sea-ice can also become locally prominent sources (Kaleschke et al., 2004; Yang et al., 2008). Since these particles are the largest in the region (Quinn et al., 2017), they are also a substantial contributor to the local aerosol optical depth (AOD) (Shindell et al., 2013). While the contribution of SSPs to the regional AOD is much more significant than its contribution to cloud albedo in the Northern Hemisphere, over the Southern Ocean it is precisely the opposite (Ayash et al., 2008). This highlights that SSPs are a regionally important component of cloud formation over the Southern Ocean. This is not surprising: SSPs are mainly comprised of highly soluble sea salt and so they are very efficient cloud condensation nuclei (CCN) (Petters and Kreidenweis, 2007). While SSPs form only a small fraction of CCN globally, they can make up $\sim$65% of CCN over the Southern Ocean (Quinn et al., 2017).

Recent studies have also shown that SSPs can act as ice nucleating particles (INPs), which encourage the phase transition of cloud droplets to ice (DeMott et al., 2016; McCluskey et al., 2018). Since the Southern Ocean is far removed from continental sources of INPs (e.g. dust), SSPs may be the only source of INPs in the region. Ice nucleation sites within the droplets are likely a result of suspended amounts of organic material within the sea surface microlayer which became entrained within the droplets during formation (DeMott et al., 2016). However, organic materials form very little of the mass composition of the resulting SSPs (Murphy et al., 1998); hence, the ice-nucleating potential of sea spray is very weak relative to continental sources such as mineral dusts (McCluskey et al., 2018). Still, the capacity for SSPs to modulate cloud phase represents an additional mechanism through which they can affect the local radiation balance.

While we have emphasized the potential radiative effects SSPs might have on the Southern Ocean region, there are other ways in which they can perturb the Earth system. Several studies have shown that the largest SSPs are non-negligible contributors to the exchange of latent and specific heat across the ocean–atmosphere interface (Richter and Sullivan, 2013; Ortiz-Suslow et al., 2016). In a bulk flux model of the air–sea exchange of heat, Andreas et al. (2015) showed that these large, "shear" sea-spray droplets accounted for fluxes of sensible and latent heat on the same order of magnitude as fluxes directly from the ocean–atmosphere interface at high wind speeds ($U_{10} > 15$ m s$^{-1}$). Observations and model simulations have shown that the rate of momentum transferred from the atmosphere to the ocean starts to decrease after a critical threshold wind speed is passed (30 m s$^{-1}$; (Powell et al., 2003; Bao et al., 2011; Hwang, 2018)). Theoretical work has suggested that this change is driven by the exchange of sensible heat between the largest droplets and the atmosphere,

which become more abundant at high wind speeds (Bao et al., 2011). This leads to considerable biases in the prediction of storm intensity (Bao et al., 2011). The ability to predict the abundance of SSPs is therefore vital to fully understanding many macroscopic processes within the region.

To constrain the potential role sea spray may have on the regional radiation budget, it is first necessary to validate current parameterizations for its flux against in situ observations of its abundance. However, there is currently a dearth of such observations over the Southern Ocean. In this work we present measurements of the total number concentration of airborne particles recorded throughout an austral summer voyage to the Ross Sea aboard the R/V *Tangaroa*. We use these measurements to test existing empirical parameterizations which describe the flux of particles from wave breaking events in open seas. Measurements from instruments onboard the High-Performance Instrumented Airborne Platform for Environmental Research (HIAPER) throughout the Southern Ocean Clouds, Radiation, Aerosol Transport Experimental Study (SOCRATES) were also used to validate these parameterizations. Since the winds throughout both of these experiments included the extremes of surface conditions encountered at the air–sea interface, understanding the flux of SSPs in this highly dynamic region will be valuable in constraining both current and future flux estimates.

# 2. Methods

*a. Measurements*

The voyage aboard the R/V *Tangaroa* began on February 9$^{th}$ and ended on March 21$^{st}$, 2018 departing and returning to Wellington, New Zealand (41°17' S, 174°46' E). The bulk of the voyage was spent in waters south of 60°S, with 17 days of the voyage spent in seas between 60–70°S and 13 days of the voyage south of 70°S.

In situ measurements of boundary layer aerosol were conducted from a container laboratory on the shelter deck of the R/V *Tangaroa* (2 m a.s.l.). The instruments within the container laboratory drew a continuous air sample through 40 m of 100 mm ID anti-static tubing (EOLU PU; IPL Ltd.) from the mast of the R/V *Tangaroa* (15 m a.s.l.). For the purposes of this study, we have primarily focussed on measurements from the passive cavity aerosol spectrometer probe (PCASP-100X; Droplet Measurement Technologies) with supplementary data from a differential mobility particle sizer (DMPS; TSI). The PCASP-100X is an optical particle counter which measured the number concentration size spectra of particles within the air sample. The instrument is capable of detecting particles with optical diameters between 0.1–3.0 $\mu$m in 30 size bins at 1 Hz. The DMPS measured the number concentration size spectra of particles within the air sample with mobility diameters between 0.02–0.3 $\mu$m in 32 size bins once every 10 minutes. We have corrected the number concentration measurements according to calculations of the sampling and transport efficiency from Brockman (2001). These calculations accounted for anisokinetic sampling conditions, diffusion of the particles toward the tube walls, and gravitational settling of the particles. All of these calculations were based on empirical parameterizations of these losses in a turbulent flow. Across the spectrum of sizes we measured, we estimate that the total sampling efficiency was at most 93%, but no less than 90%.

Throughout the voyage, a cavity ring-down spectrometer (CRDS; Picarro G2301) measured mole fractions of $CO_2$, $CH_4$, and $H_2O$ from a separate sampling line. The sampling line of the CRDS was within 5 m of the main sampling line used for the particulate sampling. Intrusions of ship exhaust from the rear of the ship would have been sufficiently

well-mixed in the turbulent air around the ship superstructure so as to affect both sampling lines. We used a threshold limit of 405 ppm of $CO_2$ to detect when ship exhaust contaminated our main sampling line. This threshold was well above the trend line of the [$CO_2$] mole fraction time-series. After removing these outliers, we used 1 Hz sub-samples of the particle number concentrations to calculate 1-minute averages of the number concentration size spectra and its standard deviation. When the standard deviation of the 1 Hz samples deviated significantly from Poisson counting statistics the sample was removed.

This study also incorporated measurements from the New Zealand Met Service's Automated Weather Station (AWS) aboard the R/V *Tangaroa*. The AWS anemometer was positioned at 22.5 m a.s.l. on the mast of the ship, while the rest of the AWS was positioned at 15 m a.s.l. The AWS measured: atmospheric pressure, atmospheric temperature, relative humidity, wind speed, wind direction, and accumulated precipitation. Measurements of the average relative wind speed and wind direction were made using a pair of ultrasonic anemometers (Gill WindSonic) and reported at 1-minute intervals. The measurements of wind speed were corrected according to directionally-dependent acceleration factors, based on a model of air flow around the R/V *Tangaroa*'s superstructure (Popinet et al., 2004; Smith et al., 2011). The wind speeds were then corrected according to the ship heading and speed to derive the true wind speed and wind direction. Finally, the acceleration-corrected, true wind speed at 22.5 m was scaled to the 10 m reference level using the bulk flux algorithms developed from the Coupled Ocean-Atmosphere Response Experiment (COARE) (Edson et al., 2013). In employing the COARE bulk flux algorithms, we have not accounted for differences in the height of the AWS due to heave with respect to mean sea level, which may amount to $\pm$4 m in heavy seas. If for a given measurement, the pitch or roll of the ship was significant with respect to the mean wind vector, then the measured wind speed would have been systematically biased low. However, throughout the voyage, the pitch of the ship was $<$20°, and so these corrections would be less than 6%.

Measurements of the boundary layer number concentration size spectra were also conducted onboard HIAPER, a modified Gulfstream V aircraft, from January 16$^{th}$–February 24$^{th}$, 2018. These measurements were part of the SOCRATES experiment. Over the course of the experiment, there were 15 flights, which departed and returned to Hobart, Australia. We have focused on the flights which coincided with our observational record, namely Research Flights (RF) 10–15 which took place between February 7$^{th}$–24$^{th}$, 2018. Two Ultra-High Sensitivity Aerosol Spectrometers (UHSAS; Droplet Measurement Technologies) were used throughout the experiment to measure the number concentration size spectra of particles within the surrounding air; however, for this study we focused solely on the measurements from the UHSAS mounted inside of the aircraft. The UHSAS sampled ambient air via a counterflow virtual impactor inlet mounted outside of the aircraft. This ensured that the internal flow rate of the UHSAS was isokinetically matched to the exterior flow around HIAPER. Like the PCASP-100X, the UHSAS is an optical particle counter which can detect particles with optical diameters between 0.059–1.022 $\mu$m in 100 discrete size bins at 1 Hz. It was determined that corrections to the number concentration size spectra from the additional ram pressure of sampling the aerosol from a moving aircraft would amount to less than 1%. This was substantially less than the observed variability in both the number concentration time series and the volume flow rate of the pump that provided the flow through the UHSAS. For each flight we identified 3–6 periods when the altitude was stable, there was little precipitation, and the observed number concentration size spectra were relatively stable. In each of these periods, we averaged the number concentration size spectra over 5–10 minutes. This resulted in 28 unique measurements between 69–6,100 m a.s.l, 17 of

which were in the boundary layer.

*b. FLEXPART-WRF*

The FLEXible PARTicle transport model (FLEXPART), FLEXPART-WRF, is a Lagrangian particle dispersion model designed to model particle trajectories within mesoscale meteorological fields from the Weather Research & Forecasting Model (WRF) (Brioude et al., 2013). For this study, we used meteorological forecasts from the real-time Antarctic Mesoscale Prediction System (AMPS) (Polar Meteorology Group, 2018). AMPS uses a variety of data sources to constrain these forecasts, including near-real-time sea-ice concentrations measured from the Special Sensor Microwave/Imager (SSM/I) radiometer and sea surface temperature (SST) data from the National Center for Environmental Prediction (NCEP) (Bromwich et al., 2005). Initial and boundary conditions for AMPS were specified according to near-real-time forecasts from the NCEP Global Forecasting System (Bromwich et al., 2005). We used the AMPS output with the widest spatial coverage, domain 1, which has a horizontal resolution of 24 $\times$ 24 km, a vertical resolution of 61 $\eta$ levels, and a temporal resolution of three hours. The AMPS forecasts used throughout this study were downloaded from `https://www.earthsystemgrid.org/project/amps.html`.

We initialized 100, 000 particle trajectories from the geographic location of the R/V *Tangaroa* every three hours to match the temporal resolution of AMPS. Additional simulations were run for every hour in between the meteorological time steps if the R/V *Tangaroa* had entered a new grid cell in the AMPS domain. These two criteria resulted in 651 unique simulations. To trace losses due to deposition throughout the simulation, FLEXPART assigned each particle a unit mass distributed over a log-normal size distribution. To match our observations, we centered this distribution around a geometric dry diameter of 0.20 $\mu$m ($D_{p,g}$ = 0.4 $\mu$m at 80% relative humidity), with a geometric standard deviation of 2.00, and a dry density of 1.84 g cm$^{-3}$. FLEXPART-WRF used the discretized Langevin equation to describe the turbulent dispersion of these particles through the atmosphere in reverse time with an adaptive time-step strictly less than 180 s. The particles were advected through the meteorological fields specified by AMPS from the time of measurement up to five days prior in reverse time. Throughout the trajectory, losses of particle mass due to dry deposition were calculated according to the resistance method (Hicks et al., 1987). To improve these calculations we modified FLEXPART-WRF to account for hygroscopic particle growth according to the ambient relative humidity (Gerber, 1985), since changes in particle size can significantly affect a particle's settling velocity and dry deposition velocity. FLEXPART-WRF also accounted for losses of particle mass from precipitation and droplet activation. Within clouds, FLEXPART-WRF calculated the scavenging rate of particles from droplet activation according to the parameterization of Hertel et al. (1995). For scavenging by precipitation below cloud, loss rates were estimated from the following empirical relationship:

$$\Lambda = AI_s^B \tag{3.1}$$

where the scavenging rate, $\Lambda$, was calculated as a function of the rain-equivalent snow intensity, $I_s$ (mm hr$^{-1}$), and user-set scavenging coefficients, A and B. While fairly good representations of particle scavenging from rain exist in the literature, there is substantially more uncertainty with regards to the scavenging from snow (Slinn, 1977). Recent parameterizations of below-cloud scavenging in the non-WRF version of FLEXPART recommend applying an empirical fit to a set of snow scavenging rates measured in southern Finland (Kyrö et al., 2009; Grythe et al., 2017). However, this parameterization doesn't explicitly account for increases in scavenging with increasing snow intensity. We observed that the differences in scavenging rates Kyrö et al. (2009) observed across the particle size spectra

were small compared to the difference in median snow scavenging rates they observed between their median observed snow intensity (0.2 mm $hr^{-1}$) and peak snow intensity (5 mm $hr^{-1}$). We used the median scavenging rates and snow intensity values they reported to estimate the following scavenging coefficients for snow: A = $4\times10^{-5}$ and B = 0.43. For reference, the typical values used by FLEXPART-WRF for rain are $5\times10^{-6}$ and 0.62, respectively. Together with the dry deposition velocity, the mass concentration loss rate could be described at any point in the simulation by the following:

$$\frac{\mathrm{d}m}{\mathrm{d}t} = -\left(\frac{v_d}{h} + \Lambda\right) m \tag{3.2}$$

where $m$ is the mass of the particle, $v_d$ is the dry deposition velocity, and $h$ was the height of the layer in which dry deposition occurred (30 m a.s.l.).

In reverse mode, FLEXPART-WRF calculated the residence time of the particles within the lowest 100 m of the atmosphere. The residence time calculation was weighted by the local air density and the residual mass of the particles within the grid-cell. The weighted residence time was normalized by the initial mass of the particles such that the resulting residence time accounted for losses from wet and dry deposition as described above. Finally, FLEXPART-WRF integrated the weighted residence time over the duration of the meteorological time-step for each grid-cell of the AMPS domain.

*c. Quantifying the contribution of sea spray*

Previous studies have shown that in pristine marine environments, the contribution of SSPs to the number concentration size spectra can be characterized by a single log-normal number concentration size distribution (Modini et al., 2015; Quinn et al., 2017). Distributions derived from this method have been shown to agree well with number concentration size spectra measured during laboratory wave-breaking experiments and the "canonical sea spray size distribution" derived from other studies (Prather et al., 2013; Lewis and Schwartz, 2004). This also agrees with the mass composition of the particles measured in the Southern Ocean boundary layer during the ACE-1 campaign, which found that particles larger than 0.3 $\mu$m were composed almost entirely of sea-salt (Murphy et al., 1998). We applied this methodology to our own measurements of the number concentration size spectra from the PCASP-100X; i.e. we fit a number concentration size spectra, $\mathrm{d}n(\mathrm{d}\log D_p)^{-1}$, of the following form:

$$\frac{\mathrm{d}n}{\mathrm{d}\log D_p} = \frac{N}{\sqrt{2\pi}\log(\sigma_g)} \exp\left[-\frac{\log^2\left(\frac{D_p}{D_{p,g}}\right)}{2\log^2(\sigma_g)}\right] \tag{3.3}$$

where $D_p$ is the particle diameter, $N$ is the total number concentration of particles, $D_{p,g}$ is the geometric mean diameter of the distribution, and $\sigma_g$ is the geometric standard deviation of the distribution. After fitting, the retrieved spectra were corrected to a relative humidity of 80% (Gerber, 1985). In the process of fitting, the geometric standard deviation ($\sigma_g$) of the mode was fixed to a value of 2, which best fit our data. While Modini et al. (2015) and Quinn et al. (2017) allowed $\sigma_g$ to freely vary in their regression analysis, the variance-covariance matrix from our regression indicated that the resulting parameters were significantly correlated, since the data very weakly constrained $\sigma_g$.

To calculate the total number concentration of sea spray from the FLEXPART-WRF residence time, we assumed that the surface flux of SSPs also followed a log-normal distribution:

$$\frac{\partial f}{\partial \log D_p} = \frac{F}{\sqrt{2\pi}\log(\sigma_g)} \exp\left[-\frac{\log^2\left(\frac{D_p}{D_{p,g}}\right)}{2\log^2(\sigma_g)}\right] \tag{3.4}$$

where $f$ is the partial particle flux in $m^{-2}$ $s^{-1}$, $F$ is the total particle flux in $m^{-2}$ $s^{-1}$, and $D_p$ is the particle diameter.

The most widely used empirical approach for constraining the particle flux from the ocean surface is the "*whitecap method*". It results from the following assumptions: first, that the total flux of particles entering the atmosphere from the ocean surface can be determined from the fractional surface coverage of whitecaps, $W$ ("*whitecap fraction*"); second, that the whitecap fraction can be adequately determined from the 10 m scalar wind speed over the ocean, $U_{10}$; and third, that the shape of the SSP size distribution is not a function of wind speed. Laboratory and field experiments have shown that all of these assumptions are reasonable (Monahan and Ó Muircheartaigh, 1980; Monahan et al., 1986). Hence, the total number of particles entering the atmosphere, $F$, can be predicted from just the 10 m wind speed, $U_{10}$:

$$\begin{aligned} F &= \frac{E}{\tau} W(U_{10}) \\ F &= \alpha W(U_{10}) \end{aligned} \tag{3.5}$$

where $W$ is a function that models how the surface coverage of whitecaps increases as a function of wind speed, $E$ is the number of particles produced per whitecap, and $\tau$ is the lifetime of the whitecaps. Since we can only hope to constrain one constant pre-factor, we combine both $E$ and $\tau$ into a single parameter $\alpha$, which we assume to be constant. Historically, the whitecap function $W$ has been assumed to be a simple power-law, based on early field observations of whitecap formation (Monahan, 1971). However, it has since been well-established that whitecaps do not form in the open ocean until the 10 m wind speed exceeds 3–4 m $s^{-1}$, which is a feature that cannot be described by a power-law model (Callaghan et al., 2008; Schwendeman and Thomson, 2015; Bell et al., 2017). We considered three other wind-dependent models of the surface flux that incorporated a threshold wind speed below which very few SSPs are produced:

$$\begin{aligned} W_{PL} &= a_1 {U_{10}}^{a_2} \\ W_C(U_{10}) &= \begin{cases} b_1 \left(U_{10} - b_2\right)^3, & U_{10} \geq b_2 \\ 0, & U_{10} < b_2 \end{cases} \\ W_F(U_{10}) &= 1 - \Phi\left(\frac{c_1}{\sqrt{U_{10}}}\right) \\ W_{LLPL}(U_{10}) &= \frac{d_1 {U_{10}}^{d_2}}{1 + \left(\frac{U_{10}}{d_3}\right)^{-d_4}} \end{aligned} \tag{3.6}$$

where $a_x, b_x, c_x$ and $d_x$ and are empirical parameters determined from regression analysis with our observations, and $\Phi$ is the error function. The first function, $W_{PL}$ ('PL' = 'Power-Law'), is as previously introduced. The second function, $W_C$ ('C' = 'Cubic'), has been used to match more recent field observations of whitecaps (Callaghan et al., 2008; Schwendeman and Thomson, 2015)). The third function, $W_F$ ('F' = 'Fetch'), was based on the theoretical work of Snyder and Kennedy (1983), who developed a model of whitecap production based on a fetch dependent threshold for wave breaking. While the work of Xu et al. (2000)

showed that the whitecap fraction could be fully determined from the model of Snyder and Kennedy (1983) if both the wind speed and fetch were known, the fetch was typically unlimited throughout our observation period. In high fetch regimes, the coverage of whitecaps is only very weakly dependent on variations in fetch (Piazzola et al., 2002). As a result, we treated $c_1$, which is a function of the fetch, as a free parameter to be determined through regression, since a single value should accurately describe the data. The last function, $W_{LLPL}$ ('LLPL' = 'Log-Logistic Power-Law') combined the power-law with a log-logistic curve to emulate the threshold mechanism. While $W_{PL}$, $W_C$ and $W_{LLPL}$ predict that the surface flux will continue increasing as a function of wind speed, the Fetch model ($W_F$) is the only model which predicts that there exists an upper bound on the particle flux at high wind speeds.

There has also been some debate as to how the temperature of the sea water might moderate whitecap formation (Mårtensson et al., 2003; Sellegri et al., 2006; Jaeglé et al., 2011; Zábori et al., 2012a; Callaghan et al., 2014; Grythe et al., 2014). This was tested directly with SST data from NCEP, which was available from the AMPS forecasts. Thus, the model of surface flux was expanded to:

$$\begin{aligned} F &= \alpha(T_w)W(U_{10}) \\ \alpha(T_w) &= \alpha_0(1+\alpha_1 T_w) \end{aligned} \tag{3.7}$$

where the coefficient $\alpha$, which describes both the lifetime of the whitecaps and the number of particles produced per whitecap, is now a function of the SST, $T_w$. Note that, in reality, parameters $\alpha_0$ and other scaling coefficients within $W$ (e.g. $a_1, b_1, d_1$) cannot be determined independently, so they are combined into a single parameter for each regression (e.g. $a_1^* = a_1\alpha$). Finally, we assumed that the surface flux was well-mixed within the lowest atmospheric grid cell in FLEXPART-WRF, $h$ = 100 m. Following these assumptions, the number concentration of particles in the SSP mode, $\hat{N}$, was calculated according to:

$$\hat{N}_i = \frac{1}{h}\int_{-t_0}^{0}\iint_{O} F(1-C_{ice})\,\mathrm{d}\mathcal{P}_i \tag{3.8}$$

where $t_0$ was the length of the FLEXPART-WRF simulation, $C_{ice}$ was the fractional surface coverage of sea ice, $O$ denotes that the integral was only integrated over oceans, and $\mathcal{P}_i$ was the map of footprint residence times for the observation $i$.

A non-linear least-squares regression analysis optimized the set of parameters for each surface flux model, $W$, being tested. Parameter optimization was achieved with the Gauss-Newton algorithm, where the goodness-of-fit was measured by the Nash-Sutcliffe model efficiency coefficient (NSE):

$$NSE = 1 - \frac{\sum_{i=1}^{m}\left(N_i - \hat{N}_i\right)^2}{\sum_{i=1}^{m}\left(N_i - \overline{N}\right)^2} \tag{3.9}$$

where $m$ was the total number of observations and $\overline{N}$ represents the average of every measurement of $N_i$ within the dataset (Nash and Sutcliffe, 1970). To account for differences between the number of parameters between models, we also calculated the Akaike Information Criterion (AIC), which penalized models with more parameters (Akaike, 1974):

$$AIC = 2k + m\log\left(\frac{1}{m}\sum_{i=1}^{m}\left(N_i - \hat{N}_i\right)^2\right) \tag{3.10}$$

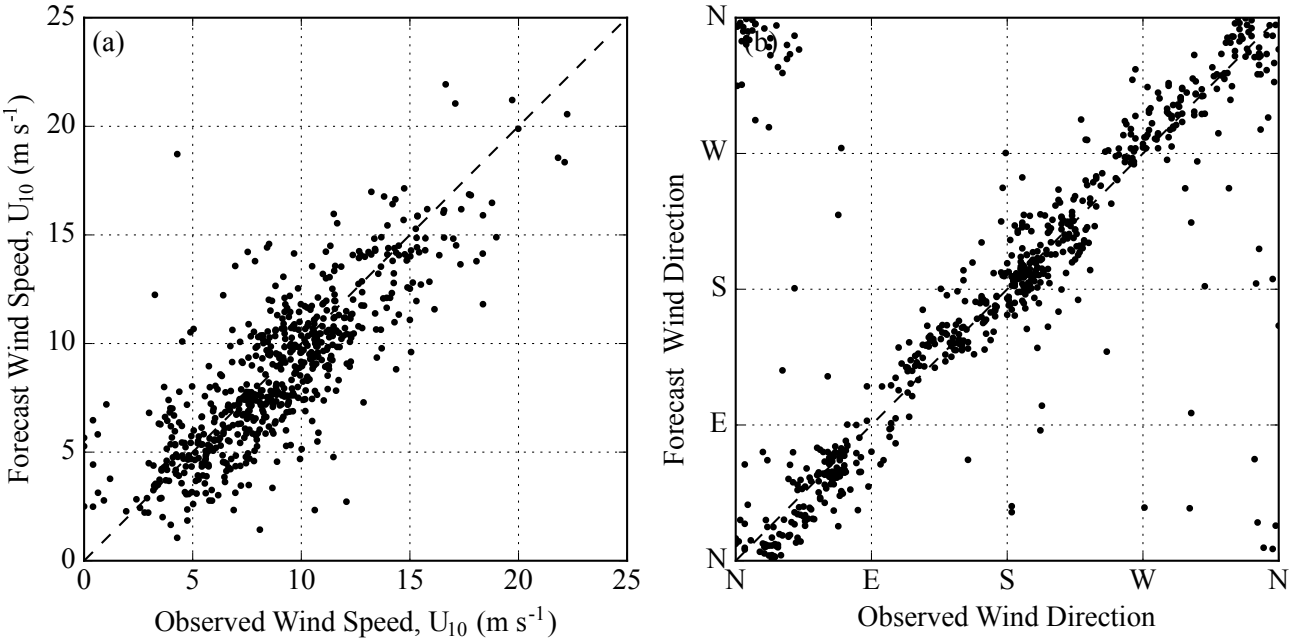


**Figure 3.1 :** (a) The hourly 10 m scalar wind speeds from the AMPS forecasts were compared to the corrected wind speed (see Section 2.1) observed on the R/V *Tangaroa*. (b) The hourly 10 m wind direction.

where *k* was the total number of parameters for a given model. The best model of surface flux was the model which minimized the AIC.

# 3. Results

*a. Comparisons Between Surface Meteorological Measurements and Model Forecasts*

To demonstrate that the transport simulations produced a meaningful link between the observations and surface fluxes, it was necessary to first validate the Antarctic Mesoscale Prediction System's meteorological fields against the record of observations from the Automated Weather Station (AWS) aboard the R/V *Tangaroa*. As described in the Section 2.a, the AWS measured wind speeds at 22.5 m, which were corrected to the 10 m reference height according to the COARE 3.5 bulk flux algorithms. The corrected wind speeds were compared to the 10 m wind speeds predicted by the AMPS forecasts by matching the location of the R/V *Tangaroa* to the nearest grid-cell within AMPS. This comparison is presented in Fig. 3.1. The correlation coefficients calculated for both the wind speed ($R = 0.81$) and wind direction ($R_\circ = 0.78$) between observations and forecasts were both significant ($p<0.01$), where $R_\circ$ represents the circular correlation coefficient (Fisher and Lee, 1986).

Despite the good agreement we found between the measured and forecast winds, there was no spatio-temporal correlation between the rain-equivalent snow rate measured aboard the R/V *Tangaroa* and the precipitation fields forecast by AMPS. However, the climatological distribution of the rain-equivalent snow rate was at least consistent between measurements and forecasts. This suggests that even if precipitation was not spatially consistent with our observations, it was at least as frequent, and of the right intensity within the AMPS forecasts. While comparing localized, discrete events like precipitation can be challenging, even comparing our measurements to grid cells within 100 km and within 6 hours of the R/V *Tangaroa* measurements did not produce a significant correlation.

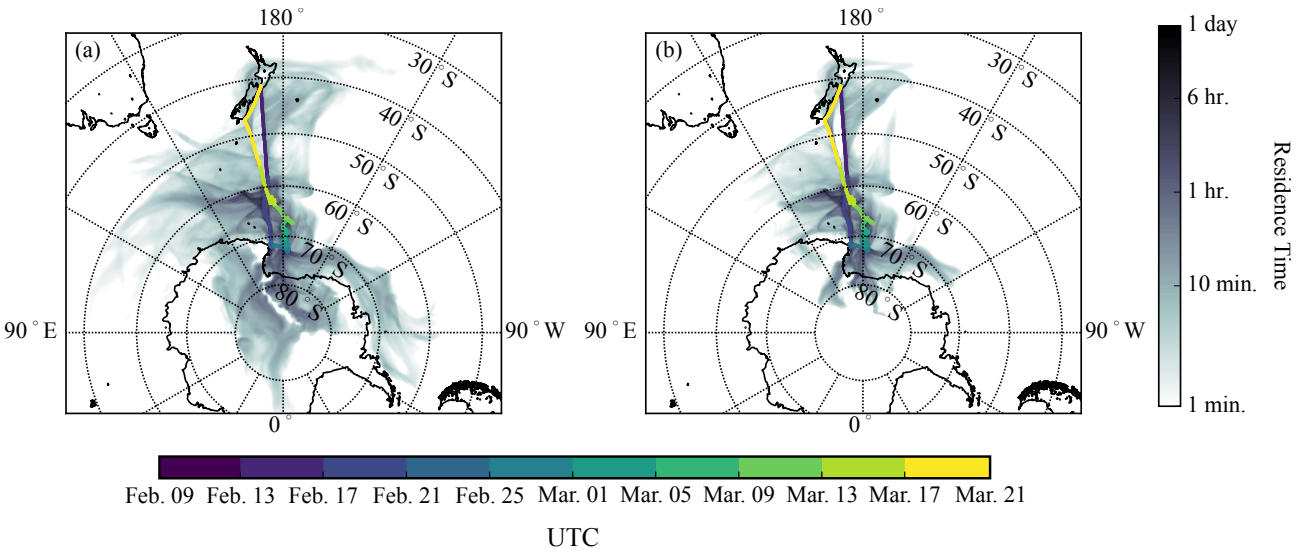


**Figure 3.2 :** (a) A map of the cumulative near-surface residence time derived from FLEXPART-WRF particle dispersion simulations. The model simulated the transport of $1\times10^5$ 0.2 $\mu$m particles in reverse time from the time of measurement to five days prior. The near-surface residence time is simply the total amount of time the particle spent below 100 m a.g.l. Within FLEXPART-WRF the transport of the particles was calculated according to meteorological forecasts from the Antarctic Mesoscale Prediction System (AMPS). (b) The same map, but now for a 48-hr. simulation. The colored line in both panels marks the track of the R/V *Tangaroa* throughout the voyage.

*b. Source–Receptor Modeling*

In Fig. 3.2a we show the cumulative five-day, near-surface, residence time for all of the source–receptor simulations described in Section 2.b. The track of the R/V *Tangaroa* throughout the voyage has also been shown for reference. As expected, the near-surface residence time was greatest near the R/V *Tangaroa*. This indicated that our measurements were most sensitive to surface fluxes near the ship. To understand how dry deposition might govern the concentration of SSPs, we also ran several FLEXPART-WRF simulations in which the dry deposition velocity was set to a fixed rate. However, the consistent turbulence of the atmosphere over the Southern Ocean meant that the simulated particles were often very evenly dispersed throughout the boundary layer. As a result, dry deposition was severely limited throughout all of the simulations. Predicted surface flux sensitivities within these simulations only began to diverge after 1–2 days had elapsed in simulation time; however, by then the residence time was typically less than 5% of what it was near the ship. Hence, dry deposition was not a strong factor controlling the concentration of SSPs.

It was evident from Fig. 3.2a, however, that our observations near the Ross Ice shelf were sensitive to non-marine sources. The fraction of the time the particles spent above non-marine surfaces throughout their five-day simulations increased rapidly as the R/V *Tangaroa* approached Cape Adare, Antarctica. Throughout this period we observed strong, southerly winds, which brought continental, Antarctic air across the Ross Ice Shelf. Intrusions of continental air into the MBL are a common phenomenon within the region (Coggins et al., 2014; Coggins and McDonald, 2015). Near the end of the observation period, after March 18$^{th}$, 2018, the source–receptor simulations showed that our measurements were also sensitive to surface fluxes from the South Island of New Zealand. This was a direct result of the strong northerlies we observed throughout our return transect.

As we identified in Section 3.1, the rain-equivalent snow rates forecast by AMPS were

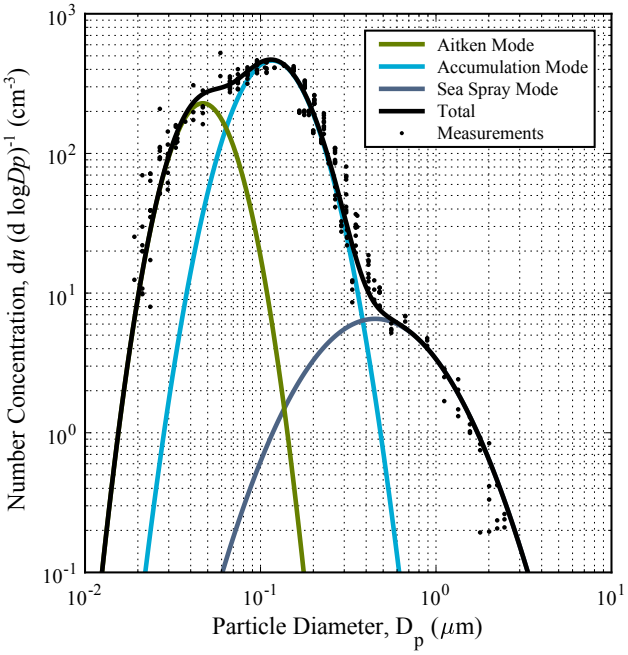


**Figure 3.3 :** Number concentration size spectra measured from the PCASP-100X (0.1–3$\mu$m) and the DMPS (0.02–0.3$\mu$m) on February 20$^{th}$, 2018 at 1300 UTC. Particle sizes have been corrected to 80% relative humidity (Gerber, 1985). Number concentrations for particles larger than 0.5 $\mu$m were used to constrain a single log-normal number concentration size distribution (“*SSP mode*”). This method has been used by other researchers (e.g. Modini et al. (2015) and Quinn et al. (2017)) to constrain the contribution of SSPs to the total number concentration size spectra. The Aitken and accumulation modes are shown for reference.

not well-correlated with snowfall intensity measured onboard the R/V *Tangaroa*. While the frequency of occurrence of these events seemed consistent, it is important to note that the wet deposition scheme used by FLEXPART-WRF implicitly assumed that in-cloud activation events only occurred within a precipitating cloud. Hence, the frequency of in-cloud scavenging events was almost certainly under-estimated within the source–receptor simulations. As Hertel et al. (1995) note, the magnitude of the loss of particles to in-cloud activation is almost always greater than either below-cloud scavenging or dry deposition. In fact, an activation event is always strong enough to terminate a particle trajectory within FLEXPART-WRF. Therefore, it was expected that the source–receptor modeling vastly overestimated the near surface residence time by continuing to advect particles that should have been completely scavenged by cloud. However, a lack of boundary layer cloud within the simulation did not stem from this issue alone. It has been well-established that there is currently a large shortwave radiation bias over the Southern Ocean (Bodas-Salcedo et al., 2014). Observations of cloud base height from radiosondes and ceilometer measurements throughout this same voyage showed that the shortwave radiation bias is related to the lack of low-level cloud and fog predicted within atmospheric models (Kuma et al., 2020). Therefore, it is reasonable to expect that even with an improved in-cloud activation scheme (e.g. Grythe et al. (2017)), FLEXPART-WRF still would have under-estimated the frequency of droplet activation events. This would have a substantial impact on our source–receptor calculations, resulting in significantly less ocean surface area contributing to the integral in Eq. (3.8). To visualize this effect, we have also shown the cumulative near surface residence time for a two-day simulation in Fig. 3.2b, instead of the five-day simulation shown in Fig. 3.2a. This is addressed further in Section 3.4.

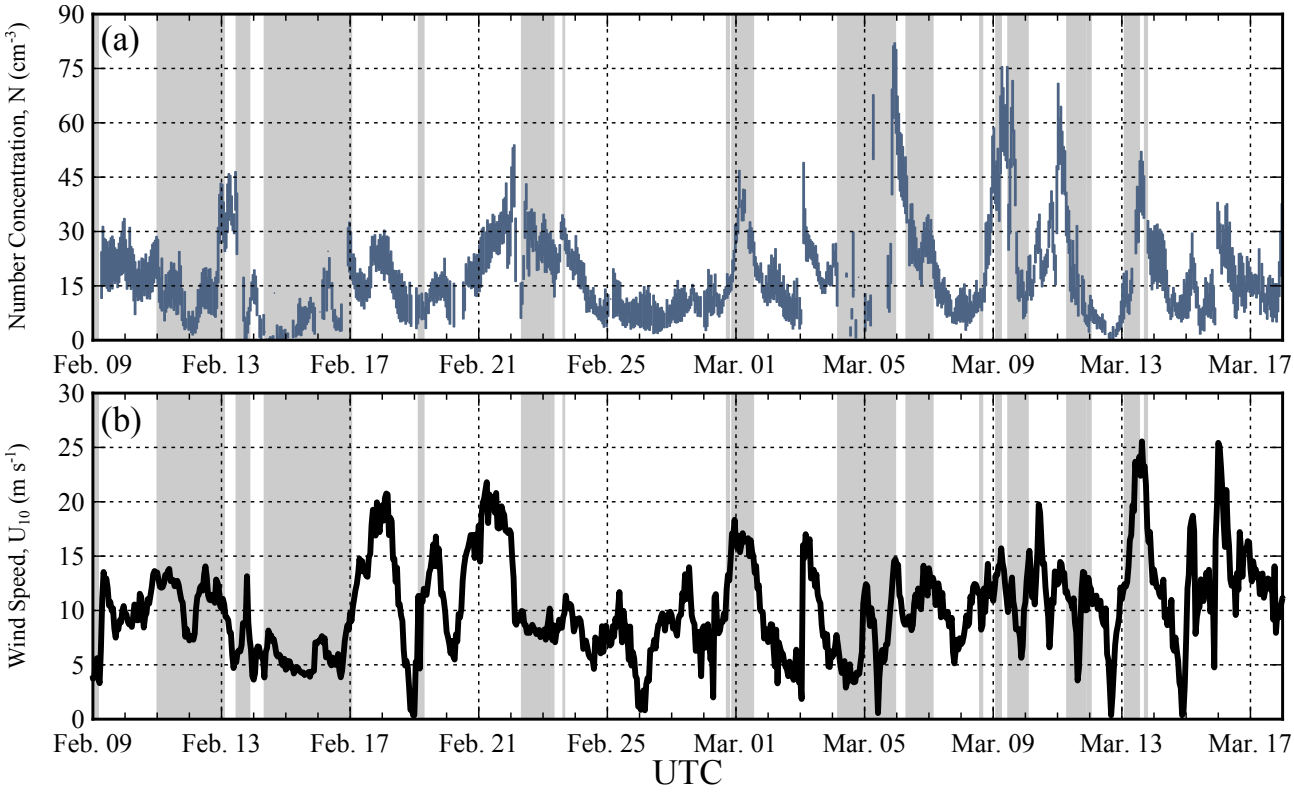


**Figure 3.4 :** (a) The average hourly number concentration of sea spray particles is shown for the entire campaign with periods of fog (RH>98%) or rain (>1 mm hr$^{-1}$) marked by the shaded areas. (b) The hourly 10 m wind speed.

*c. Number Concentrations of Sea Spray*

In Fig. 3.3 we show an example modal analysis of a number concentration size spectrum measured by the PCASP-100X and DMPS aboard the R/V *Tangaroa*. The size spectra were used to constrain three log-normal "*modes*" which represented the entire size distribution. The largest of these modes, the SSP mode, is so-named as it has been shown to be comprised almost solely of SSPs (Modini et al., 2015; Quinn et al., 2017). At each hour of observation throughout the voyage we constrained the SSP mode from the spectral measurements shown in Fig. 3.3, resulting in the time series of the total number concentration of SSPs shown in Fig. 3.4. In general it was sufficient to constrain the SSP mode from just the PCASP-100X measurements, so the measurements from the DMPS were not used in this study, but are shown for reference. Throughout the entire voyage, we observed the median and standard deviation of the geometric mean diameter of the SSP mode to be $0.4 \pm 0.05$ $\mu$m at a relative humidity of 80%. This agreed well with the observations of Quinn et al. (2017) in the Southern Ocean. This also agreed with the median dry diameter of SSPs measured from laboratory generated waves, 140–200 nm (Prather et al., 2013), since SSPs are twice as large at 80% relative humidity compared to dry conditions (Gerber, 1985).

In Fig. 3.4a, the total number concentrations of SSPs and the 10 m scalar wind speeds measured are shown from the beginning of the voyage, February 9$^{th}$, 2018, until March 18$^{th}$, 2018. Throughout the voyage, there were several periods when either fog or precipitation was observed at the ship. As expected, fog very efficiently scavenged the particles in the SSP mode through droplet activation processes, much more so than precipitation. However, the lack of observed particles during such events meant that the SSP mode could not be constrained. This is particularly evident around March 5$^{th}$, 2018. In the last three days of

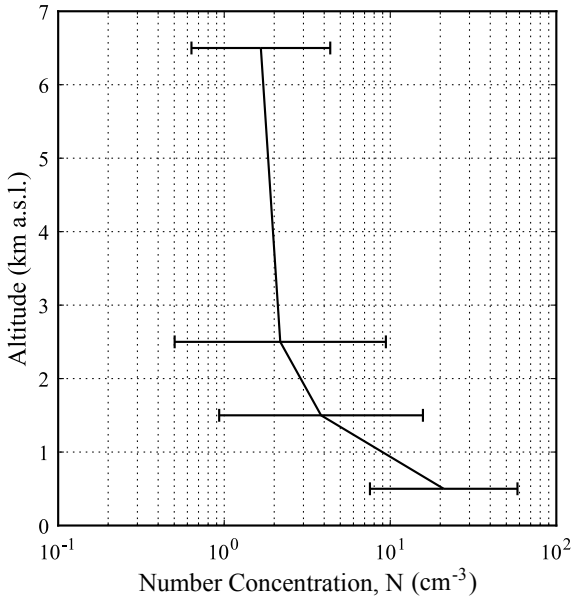


**Figure 3.5 :** The total number concentration of sea spray generated particles is shown as a function of altitude over the course of several flights aboard HIAPER, (RF 11–15). The ranges within each altitude bin show the minimum and maximum number concentration observed. Flights RF 11–15 took place on the following days, in order: Feb. 17$^{th}$, 18$^{th}$, 20$^{th}$, 21$^{st}$ and 24$^{th}$, 2018.

the voyage, March 18$^{th}$–21$^{st}$, 2018, we encountered strong northerly winds along the coast of New Zealand, which transported terrestrial particles to the R/V *Tangaroa*. The addition of these non-SSPs resulted in number concentration size spectra from which the SSP mode could not be constrained. As a result, measurements when fog or precipitation was observed at the ship, or when there was a significant influence from New Zealand were excluded from the regression analysis presented in the following section.

In Fig. 3.4b we also show the 10 m wind speed throughout the same period of measurement. We observed that when winds were light ($U_{10}$ < 4 m s$^{-1}$) the total number concentration of particles in the SSP mode was no more than 10 cm$^{-3}$, and had a median of 7 cm$^{-3}$. Light-wind periods ($U_{10}$<4 m s$^{-1}$) occurred 14% of the time in upwind conditions, as weighted by the near surface residence time. However, during a light-wind period on March 12$^{th}$, 2018, there appeared to be no particles at all. This agreed well with the transport modeling in Fig. 3.2, which showed that during all light-wind periods, except the period occurring on March 12$^{th}$, the particles had a significant near surface residence time over Antarctica. While the boundary layer over Antarctica is generally a very pristine environment, human activity from research stations near the Ross Ice shelf and exposed mountain faces both represent potential sources for the concentration of particles observed at low wind speeds. In the regression analysis that followed, the median concentration of SSPs observed at low wind speeds was removed from the observations (except for the period around March 12$^{th}$, 2018). After removing this background concentration, we calculated the hourly-averaged number concentration of particles in the SSP mode to be 9 cm$^{-3}$, with a maximum of 62 cm$^{-3}$.

In Fig. 3.5 we show the total number concentration of SSPs derived from the UHSAS number concentration size spectra onboard HIAPER. These measurements were taken over the course of several flights in February 2018 to illustrate the range of concentrations ob-

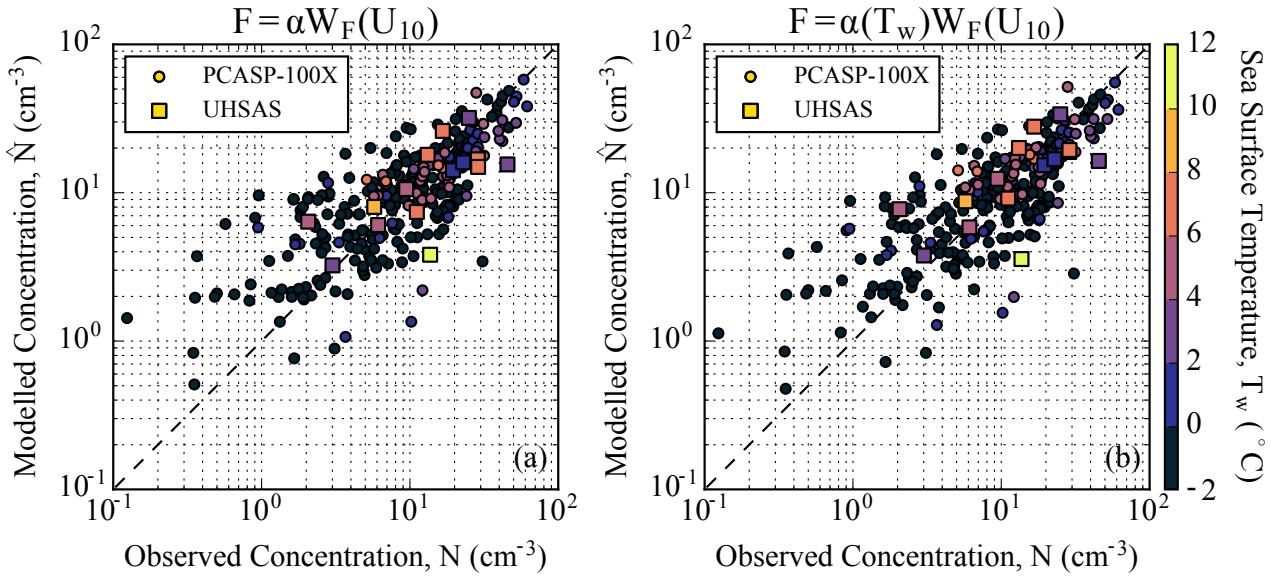


**Figure 3.6 :** (a) Predicted concentrations of sea spray generated particles from the best parameterization of surface flux are compared to measurements from two observation platforms: a PCASP-100X aboard the R/V *Tangaroa* and the UHSAS onboard HIAPER. The best parameterization for the surface flux, $F$, of these particles was a function of the wind speed over the ocean surface. Each model–measurement pair is colored according to the average SST, weighted by the near-surface residence time. (b) As in (a), but for a parameterization of surface flux which incorporated a linear function of SST in addition to the wind speed dependence.

served within each 1 km bin. The measurements within one kilometer of the Earth's surface were always determined to be below-cloud (if any cloud was present) and within the boundary layer. In contrast, all other bins were determined to be above cloud (if any cloud was present) and above the boundary layer. From Fig. 3.5 we can also identify that there was always at least 5–10 $cm^{-3}$ of SSPs in the boundary layer, which is consistent with the measurements at low wind speeds on board the R/V *Tangaroa*. As expected, there were also very few SSPs above the cloud, indicating that nearly all of these particles had been consumed during cloud formation.

*d. Regression Analysis*

Predicted SSP concentrations can be obtained by integrating Eq. (3.8); however, we have already identified that particle losses from in-cloud scavenging represented the greatest uncertainty to our source–receptor modeling. To address this within the regression analysis we allowed the simulation length, $t_0$, to vary as a free parameter within Eq. (3.8). In effect, this allowed the regression to estimate the return rate of a droplet activation event within a boundary layer cloud (e.g. fog or marine stratocumulus) or a significant precipitation event (>10 mm $hr^{-1}$). Either of these events would have efficiently scavenged the particle, thereby terminating its trajectory. This approach is similar to the Statistical Wet Deposition method used by other researchers, which prescribes the length of time it takes a surface flux of particles to fully mix into the boundary layer after a precipitation event or cyclone (e.g. Ovadnevaite et al. (2014)).

In Table 3.1 we have calculated the relative likelihood that a given surface flux parameterization fit the data as compared to the best parameterization, $W_F$. We used the relative probabilities in Table 1 to compare two parameterizations: for instance, modelling the flux with $W_F$ and a function of sea surface temperature was only 60% as likely to optimally fit our data as using $W_F$ alone. We also found that regardless of the surface flux parameter-

ization, the optimal simulation length, $t_0$ was 48 $\pm$ 3 hours. This is similar to the "*filling time*" Ovadnevaite et al. (2014) used to characterize surface fluxes of SSPs from their measurements in the North Atlantic. The filling time is a characteristic timescale used in the Statistical Wet Deposition Method for determining sea spray fluxes from a concentration time series (Lewis and Schwartz, 2004). Definition of the filling time varies by author. In Ovadnevaite et al. (2014), they interpret the filling time as "*...the time between the cyclone formation and subsequent arrival to [the measurement location]"* instead of "*the time since the last precipitation event as considered in Lewis & Schwartz (2004)"*. The filling time we determined is consistent with the average time that elapsed between the passage of seven separate cyclones we encountered throughout March, 2018. These cyclones provided widespread high winds and boundary layer cloud, resulting in high fluxes, but relatively short lifetimes for any suspended particulate. Hence, our finding is consistent with the definition of filling time given by Ovadnevaite et al. (2014).

According to the AIC, the best parameterization for the surface flux of SSPs, $F$, used the fetch parameterization for whitecaps, $W_F$ (Snyder and Kennedy, 1983; Xu et al., 2000):

$$\begin{aligned} \frac{\partial f}{\partial \log D_p} &= \frac{F}{\sqrt{2\pi}\log(2)} \exp\left[-\frac{\log^2\left(\frac{D_p}{0.4}\right)}{2\log^2(2)}\right] \\ F &= \alpha W_F(U_{10}) \\ \alpha &= 3.6 \times 10^7 \\ W_F(U_{10}) &= 1 - \Phi\left(\frac{6.5}{\sqrt{U_{10}}}\right) \end{aligned} \tag{3.11}$$

where $D_p$ is the particle diameter in $\mu$m at a relative humidity of 80%.

In Fig. 3.6a we show the model–measurement residuals for the best parameterization of surface flux. The model–measurement residuals have been color-coded according to the average SST. The average values of SST were weighted by the two-day, near-surface residence time. On average, the predicted concentrations did not appear to be biased positive or negative. However, a recent study by Jaeglé et al. (2011) showed that particle fluxes may significantly depend on SST. Changes in SST result in changes to the water viscosity. This is thought to modify the length of time for the whitecap to dissipate, $\tau$, which is part of the constant, $\alpha$. Hence, in order to compare to their result, we fit a linear correction term for the constant $\alpha$ presented in Eq. (3.11) as a function of the SST, $T_w$, finding:

$$\alpha(T_w) = 3.6 \times 10^7 (1 + 0.024 T_w) \tag{3.12}$$

**Table 3.1 :** The values listed in this table are the relative likelihood that a given parameterization of surface flux correctly predicted the observed number concentration of sea spray generated particles relative to the best parameterization. These values were calculated from the difference between the Aikake Information Criterion (AIC) of each parameterization and the AIC of the best parameterization ($AIC_b$) according to the following: $\exp(-0.5(AIC - AIC_b))$ (Burnham and Anderson, 2002). The AIC measures the log-likelihood that a given surface flux parameterization minimizes the residual sum of squares between predicted and observed concentrations while also penalizing parameterizations which include large numbers of parameters (Akaike, 1974). See Eq (3.6) for parameterization definitions.

| Surface Flux parameterization | $W_{PL}$[‡] | $W_C$[†] | $W_F$[§] | $W_{LLPL}$[††] |
|---|---|---|---|---|
| $F(U_{10})$ | $<1\times10^{-3}$ | $<1\times10^{-3}$ | 1 | 0.2 |
| $F(U_{10}, T_w)$ | $<1\times10^{-3}$ | $<1\times10^{-3}$ | 0.6 | $<1\times10^{-3}$ |

[‡]Power-Law; [†]Cubic; [§]Fetch; [††]Log-Logistic Power-Law.

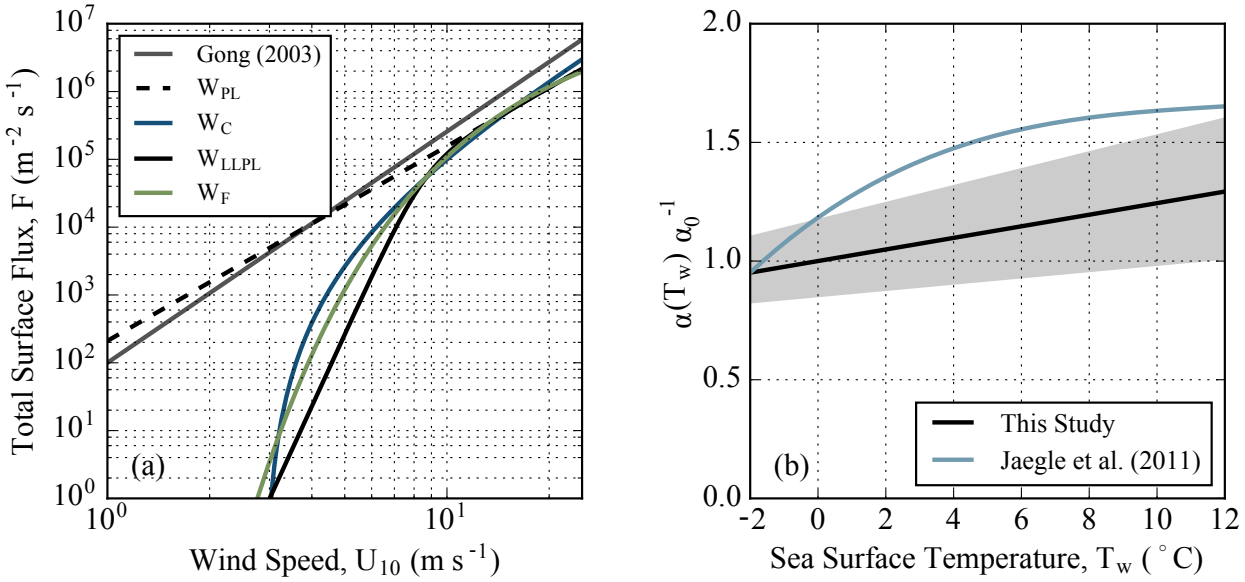


**Figure 3.7 :** (a) The best parameterization of the total surface flux of sea spray generated particles, $W_F$, is compared to calculations from the Gong (2003) parameterization. (b) The linear bias correction function found by the regression is compared to the function reported by Jaeglé et al. (2011), where their function has been shifted vertically to match the linear bias correction function at T = -2° C. The shaded region shows how uncertainty in the retrieved regression parameters propagated to prediction uncertainty.

The model–measurement residuals of the temperature-corrected parameterization, are shown in Fig. 3.6b. From Table 3.1 we can see that this did not substantially improve model fidelity. In both Figs. 3.6a and b we have also shown the model–measurement pairs for the SOCRATES observations within the boundary layer. Since these measurements were not included within the regression framework, the good agreement in both of these figures provides a measure of confidence that Eq. (3.11) produces reasonable results within the Southern Ocean region.

In Fig. 3.7a we show the predicted flux of SSPs from each of the models in Eq. (3.6) as a function of near-surface wind speed. The total particle flux predicted by Gong (2003) has also been shown for reference. In Fig. 3.7b we have compared the linear function of SST we recovered from the regression analysis to the polynomial function fit by Jaeglé et al. (2011). We have shifted the values of the polynomial function so that it matches our linear function at $T_w$ = -2°C. The slope of our linear function predicts that SST is not as significant a control of SSP surface flux as shown by Jaeglé et al. (2011). This may be a result of the distribution of our measurements across different SST regimes since 78% of our observations were related to waters in a narrow temperature range (-2–0°C). Hence, there would be little improvement to either the NSE or AIC for these samples. Still, as shown in Fig. 3.7b, the bias correction curve presented by Jaeglé et al. (2011) is clearly outside of the uncertainty bounds for the modest temperature dependence we observe within our dataset.

Finally, we compared the Nash-Sutcliffe model efficiency coefficient (NSE) for the best parameterization we found within our regression framework to two different parameterizations of SSP surface flux. The NSE is generally equivalent to $R^2$, but can also become negative when the average observed concentration provides a better fit to the data than the proposed parameterization. From Table 3.2 it is clear that Eq. (3.11) predicted concentrations of SSPs that were more consistent with our observations than predictions from either the Gong (2003) or the Jaeglé et al. (2011) parameterizations. Comparisons showed that

the Gong (2003) parameterization produced too many SSPs at all wind speeds.

For reference, we also performed the regression for the entire five-day simulation. In all of the parameterizations presented, the NSE decreased significantly for the longer simulation, consistent with our hypothesis that in-cloud droplet activation was not accurately simulated. In addition, surface fluxes predicted by $W_F$ when constrained by the five-day simulations were strictly smaller than surface fluxes predicted by $W_F$ when constrained by the two-day simulations, for all wind speeds. Therefore, our finding that the parameterization of Gong (2003) over-predicted the surface flux of SSPs was robust.

*e. Meta-Analysis of Whitecap Data*

In order to assess the conditions under which the parameterization presented above may be applicable, we analyzed global whitecap data from the literature. In Fig. 3.8b we have amalgamated 527 in situ ship-borne and tower observations of the surface coverage of whitecaps as a function of the 10 m wind speed, $U_{10}$ (Xu et al., 2000; Stramska and Petelski, 2003; Sugihara et al., 2007; Callaghan et al., 2008; Norris et al., 2013; Schwendeman and Thomson, 2015; Bell et al., 2017; Brumer et al., 2017; Jia and Zhao, 2019). Studies published after the year 2000 were used since they all employed some form of automated image processing. This meant that each whitecap measurement was a result of $>10^2$ images, a necessary minimum to have a convergent mean (Callaghan and White, 2009). The spatial coverage of these studies is shown in Fig. 3.8a, indicating that there is a good degree of coverage across surface temperature regimes within the database. In Fig. 3.8b we have shown three parameterizations for the whitecap coverage from the literature overlying the in situ measurements (Monahan and Ó Muircheartaigh, 1980; Callaghan et al., 2008; Hwang, 2018). We used the AIC to compare the existing parameterizations shown in Fig. 3.8b to the fetch model, which was fit to the data via non-linear least-squares regression. We found that the fetch model for whitecap development captured the variability in the database best, with the relative likelihood that the other models accurately captured the variability being $<10^{-3}$. It also did so with a continuous function, whereas the other models were piece-wise. The best fit for the whitecap data was as follows:

$$W_F = 1 - \Phi\left(\frac{6.2}{\sqrt{U_{10}}}\right) \tag{3.13}$$

We also sought to validate the dependence of SSP fluxes on SST. However, SST data within the works cited were either not included or simply summarized as a range of values encountered. Still, most voyages made their measurements within a fairly narrow SST band. Hence, we could test whether or not there was any dependence by using a voyage-average SST for each study. Using the AIC as a measure of the goodness of fit, we found that SST did not improve the regression. This is evident by visually comparing the observations of

**Table 3.2 :** The Nash-Sutcliffe model efficiency coefficient between the number concentration of SSPs predicted by a given surface flux parameterization and the observation conducted aboard the R/V *Tangaroa*. The time, $t_0$, is the length of time for which the Lagrangian particle dispersion parameterization simulated the movement of SSPs back in time. A negative value for the NSE implied that the mean of the observations was better at predicting the observed variance than the given parameterization, whereas a value of 1 would imply a perfect model–measurement fit.

| Surface Flux parameterization | NSE ($t_0$ = 48 hours) | NSE ($t_0$ = 120 hours) |
|---|---|---|
| (Gong, 2003) | <0 | <0 |
| (Jaeglé et al., 2011) | 0.22 | <0 |
| Eq. (3.11) | 0.67 | 0.52 |

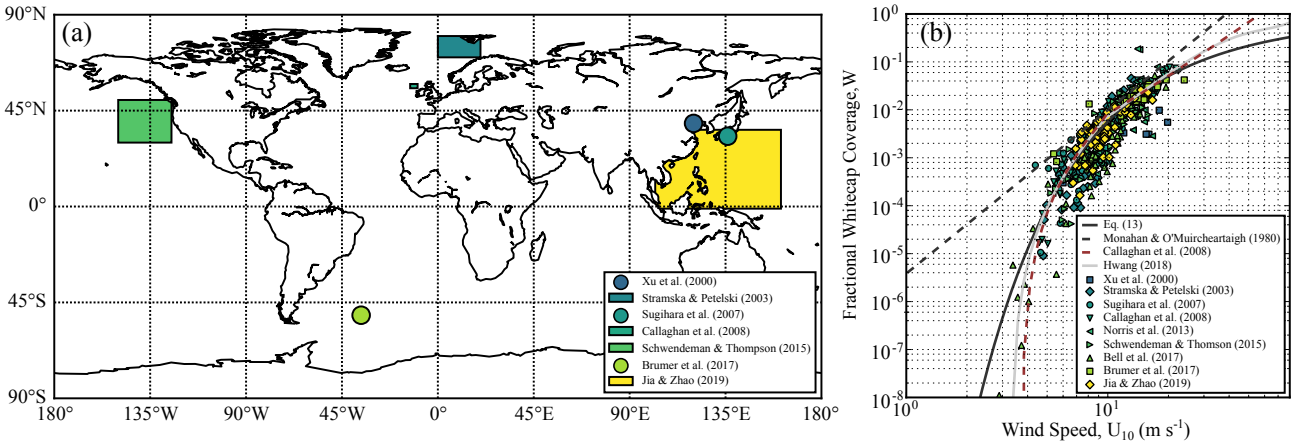


**Figure 3.8 :** (a) The spatial extent of shipborne and tower whitecap observations within the database assembled for the whitecap meta-analysis. Studies where the coordinates of the observations were not specified all took place in the North Atlantic. (b) The fractional coverage of the sea surface by whitecaps as a function of 10 m wind speed.

Jia and Zhao (2019), which took place in extremely warm seas ($T_w$ ~28°C), to the rest of the data points.

# 4. Discussion

*a. Meteorological Measurements*

In the previous section, we presented total number concentrations of SSPs within the Southern Ocean marine boundary layer as measured from two separate measurement platforms. These were compared to estimations of the total number concentration of SSPs derived from a source–receptor analysis. To assess the validity of the meteorological fields used within the source–receptor analysis, we compared the near-surface winds forecast by AMPS to our observations aboard the R/V *Tangaroa*. We found that the near-surface winds forecast by AMPS compared favorably to our observed winds with respect to both magnitude and direction. Previous studies have found large biases between AMPS forecasts and the true, local winds over the complex coastal topography of the Antarctic coastline (Bromwich et al., 2005; Jolly et al., 2016). However, ocean waves have much less surface roughness in comparison to the coastal topography of Antarctica, which would suggest that this may not be as substantial an issue over the ocean.

While the precipitation fields forecast by AMPS did not correlate well with our measurements, the climatological distribution of precipitation events within AMPS was consistent with our observations. However, within FLEXPART-WRF a lack of precipitation "*trickled up*" to the cloud layer: in the current version of FLEXPART-WRF, clouds are only present within a simulation if they are precipitating. As a result, scavenging of SSPs from in-cloud activation was likely poorly modeled within the AMPS–FLEXPART-WRF framework. As our own observational record showed, SSPs were strongly scavenged by boundary layer cloud (e.g. fog), particularly through February 15–17$^{th}$ and March 4–6$^{th}$, 2018. It is useful, however, to recall that clouds over the Southern Ocean are not very well represented within modern atmospheric models (Trenberth and Fasullo, 2010; Schuddeboom et al., 2019). Current era atmospheric models systematically under-predict the amount of low-lying cloud and fog relative to the true cloud observed over the Southern Ocean (Kuma et al., 2020). Hence, even if a state-of-the-art microphysical parameterization of in-cloud scavenging had been present in FLEXPART-WRF, it is likely that the scavenging of sea spray still would have

been under-estimated.

*b. Source–Receptor Modelling*

Once we had established that there was a missing sink of sea spray within our source–receptor framework, it was necessary to decouple this sink from each of the parameterizations of surface flux we tested within the regression analysis. This was accomplished by allowing the simulation length to vary as a free parameter within the regression analysis. The simulation length can be interpreted as the average length of time since a boundary layer in-cloud activation event (e.g. fog or low-cloud). From Table 3.2 it is evident that our observations were better reproduced for a fixed simulation length of two days, rather than the five days originally simulated. This agreed well with the "*filling time*" of 1.5–2 days used by Ovadnevaite et al. (2014) to constrain the surface flux of sea spray in the North Atlantic. While setting a voyage-wide simulation time may have been a gross approximation, it was likely the only approach in light of the present systematic cloud biases over the Southern Ocean.

*c. Regression Analysis*

By constraining the missing sink of sea spray within our model framework, we could finally compare how well the near-surface wind speed and SST predicted our observational record. We found that the fetch parameterization presented by Xu et al. (2000) and Snyder and Kennedy (1983) performed the best in our comparison as measured by the Nash-Sutcliffe model efficiency coefficient, NSE, and the Akaike Information Criterion, AIC. The parameterization, $W_F$, is so-named since the parameter $c_1$ is a function of the fetch. In our analysis we have assumed that this parameter was constant, since fetch does not significantly influence the degree of whitecapping in open seas (Hsu, 1986; Piazzola et al., 2002). Later, when we performed a similar regression analysis with a database of whitecap coverage observations, we found a slightly smaller value for $c_1$. When we compared Eq. (3.11) to Eq. (3.13), we found that $c_1$ retrieved from the whitecap regression was $6.2 \pm 0.2$, which was consistent with the value of $6.5 \pm 0.2$ we retrieved from the SSP regression. The sensitivity of $W_F$ means that Eq. (3.11) will under-estimate whitecap coverage globally and subsequently result in under-estimations of sea spray fluxes. However, we can compare to the value for $c_1$ retrieved when we only consider Southern Ocean whitecap data from Brumer et al. (2017) ($c_1 = 6.4 \pm 0.1$). Combined with the goodness of fit to the SOCRATES data (Fig. 7a), this provides a secondary measure of validation for the parameterization over the Southern Ocean. We can only conclude that for a global study, a value for $c_1$ of 6.2 may be more appropriate. For Southern Ocean specific studies a value for $c_1$ of 6.5 should be used.

Finally, we compared results from two other parameterizations for the surface flux of SSPs to our observations. We found that neither the Jaeglé et al. (2011) nor the Gong (2003) parameterization could predict the concentration of SSPs we observed over the Southern Ocean as well as Eq. (3.11). This is connected to how the Gong (2003) parameterization (which Jaeglé et al. (2011) re-scaled) scales the surface flux of SSPs with increasing wind speed. Within this parameterization, the scaling is estimated via a power-law relationship between the surface coverage of whitecaps and near-surface wind speed (Monahan and Ó Muircheartaigh, 1980). However, as we show in Fig. 3.8b, the parameterization presented by Monahan and Ó Muircheartaigh (1980) results in consistent over-estimations of the whitecap coverage. These over-estimations propagate through the SSP flux parameterization of Gong (2003) and lead to the over-estimations in concentrations we observe. In addition, the power-law predicts that there will always be a flux of sea spray from the ocean surface, despite it being well-established that whitecaps do not form until the wind speed over the

ocean exceeds 3–4 m $s^{-1}$. Even the re-scaled Gong (2003) parameterization presented in Jaeglé et al. (2011) did not match our observations well, either.

*d. The Effect of Sea Surface Temperature*

To understand differences between whitecapping in different regions, previous research has focused on wave parameters and SST. As Sugihara et al. (2007) and Goddijn-Murphy et al. (2011) have shown, there is a marked difference between observations of whitecaps in a pure windsea vs. a swell dominated sea. Indeed, when we fit $W_F$ to the whitecap data from Sugihara et al. (2007) we retrieved a value for $c_1$ of 6.1 $\pm$ 0.1 in a pure windsea (indicating higher spatial coverage of whitecapping) compared to 6.7 $\pm$ 0.1 when the winds were following swell or counter swell (indicating lower spatial coverage of whitecapping). This could potentially explain the difference between the value of $c_1$ we retrieved from our measurements and the one retrieved from the entire whitecap database. However, conversely, in a satellite-derived whitecap database, Albert et al. (2016) found that whitecaps were not dependent on wave parameters, but were actually modestly dependent on SST. They noted that the lack of dependence on wave parameters may have been a result of using wind history as a proxy for wave age and spatial averaging. However, we found that there was no dependence on SST within the database of in situ whitecap observations.

Of course, even if SST does not affect the fractional coverage of whitecaps, it can still affect the surface flux of particles through changes to viscosity. Results from laboratory studies are mixed: while two studies have clearly shown that the surface flux of sea spray should increase in warmer waters (Mårtensson et al., 2003; Sellegri et al., 2006), others found that that differences in seawater composition (Callaghan et al., 2014) and wave characteristics (Callaghan et al., 2012) could be much more important. Other laboratory results have even shown that increases in water temperature led to decreases in sea spray fluxes (Zábori et al., 2012a). To test whether or not changes in SST affected our own observations, we used SST as a second independent variable within the regression analysis. We found that the impact to the model–measurement fit was more modest than predicted by Jaeglé et al. (2011) (see Fig. 3.7b), and that the parameterization which only used wind speed (Eq. (3.11)) performed just as well. As we noted, this may have been a result of making observations in a very narrow range of SSTs, which would result in very small changes to the regression metrics we analyzed. However, from Fig. 3.6b we can see that the model–measurement residuals don't appear to be significantly biased from the 1:1 line at warm temperatures.

Ultimately, we should be cautious when implementing temperature correction functions for SSP fluxes. Consider that field observations have already clearly shown that the presence of swell inhibits the surface fraction of whitecaps for a given wind speed (Sugihara et al., 2007). Hence, global climatologies of swell could potentially explain the latitudinal trends in SSP flux expected (Jaeglé et al., 2011): swell rarely occurs in the tropics (where fluxes are expected to be higher), whereas swell frequently is present at high latitudes (where fluxes are expected to be lower) (Jiang and Chen, 2013). As a result, the resulting bias correction curve Jaeglé et al. (2011) derived from in situ and satellite observations of aerosol may be partially dependent on the presence (or absence) of swell. Yet, the curve attributed the latitudinal variations in flux necessary to fit their observations completely to variations in SST. Our own observations, which were made exclusively in the presence of swell, showed that the dependence of SSP fluxes on SST was much weaker than anticipated by Jaeglé et al. (2011), leading to a very negligible effect on model performance. We conclude that a more comprehensive global study of sea spray which fully controls for upwind wave and SST

conditions is needed in order to decouple these two effects. In the interim, models should be cautious in implementing functions which could potentially over-exaggerate radiative feedback loops.

*e. The Direct Radiative Effect*

As the goal of this study was to understand how SSPs might influence the local radiation budget, it would be useful to evaluate whether or not changes to the parameterization of SSP fluxes result in substantial changes within existing climate-chemistry models (CCMs). A recent study comparing the winter-time AOD over the Southern Ocean found that current era parameterizations (e.g. Gong (2003)) of sea spray within a climate-chemistry model (CCM) resulted in over-estimations of the AOD relative to satellite observations (Revell et al., 2019). However, in the austral summer, the opposite was observed: namely, a lack of particles formed from the nucleation of sulfate-gasses resulted in under-estimates of AOD. Within this same study, the parameterization of surface flux, $W_{PL}$, was implemented within the CCM to better constrain the contribution of SSPs to the total particle population (Revell et al., 2019). While $W_{PL}$ was not the best function determined by this work, it was similar in form to the Gong (2003) currently implemented within the CCM being studied, so it was an easy substitution. Since $W_{PL}$ had a Nash-Sutcliffe coefficient of 0.6 it also produced results that were consistent with Eq. (3.11). It is important to note that $W_{PL}$ was used to re-scale the size distribution of the Gong (2003) parameterization, so any changes would be related to differences in the scaling function and not to differences between size distributions. Results conclusively showed that the more conservative estimates of the surface flux of SSPs generated by $W_{PL}$ completely removed the bias in winter-time AOD that was previously observed. Therefore, we are confident that the parameterization for the surface flux of SSPs presented in Eq. (3.11) will result in better predictions of the abundance of SSPs within the Southern Ocean region. More importantly, Revell et al. (2019) show that it helps disentangle the potential compensating errors in predicting the AOD for studies interested in the more complicated gas phase and aqueous phase chemistry which produces sulfate particles from volatile marine precursors like dimethylsulfide.

As we have emphasized throughout this study, the MBL over the Southern Ocean region is home to the strongest surface winds over open ocean on Earth (Young, 1999). Surface winds also appear to be getting stronger: at Macquarie Island, winds have increased in intensity by 3 cm $s^{-1}$ per year from 1973–2011, with satellite data showing that winds over the Ross Sea increased by 0.5–1% through 1991–2008 (Hande et al., 2012a; Young et al., 2011). Within the Ross Sea region, this increase is related to the deepening of the Amundsen Sea low, an area of climatologically low pressure in the Southern Ocean which influences regional winds, sea-ice extent and temperature (Coggins and McDonald, 2015; Raphael et al., 2016). As we show throughout this study, sea spray has a highly non-linear relationship with wind speed. Given their large contribution to the CCN population (10–65%; Quinn et al. (2017)), AOD (Murphy et al., 1998; Revell et al., 2019), and cloud phase (McCluskey et al., 2018) over the Southern Ocean, these particles can have a significant buffering effect on the local climate. We would therefore encourage future studies interested in climate projections for the Southern Ocean to make use of Eq. (3.11) when predicting the surface flux of sea spray generated particles.

# 5. Conclusions

In this study, we described and optimized an existing parameterization for the surface flux of sea spray generated particles (SSPs) based on the 10 m wind speed in Eq. (3.11). Within our regression framework we found that the dependence of SSP fluxes on SST was very

weak in the temperature range of our observations ($T_w$ < 12 °C) and that it did not help to constrain additional variability in our data set. An external database of previously published whitecap observations was exploited to test the parameterization we used in this analysis and found no temperature dependence at all. While others have shown that temperature-dependent flux parameterizations seem to explain known latitudinal variations in SSP flux, the correction functions derived from such an analysis could potentially be a proxy for latitudinal variations in wave characteristics. Given the potential links between SSPs and the Southern Ocean radiation budget, we should be cautious to add feedback loops where none may exist.

Finally, the parameterization presented in this study is already being used to model the AOD and concentration of CCN in the region. Research has shown that the new parameterization vastly improved regional calculations of AOD, compared with previous parameterizations which over-predicted the surface flux of SSPs (Revell et al., 2019). We recommend that studies interested in aerosol–cloud interactions implement the parameterization as it has been shown to better constrain the contribution of SSPs to the CCN population.

# Classification of the Below-Cloud Mixing State Using In-Situ and Remotely-Sensed Measurements


## Abstract

*We demonstrate that the Spearman Rank correlation coefficient between the abundance of particulate surface area at sea–level and measurements of ceilometer backscatter can be used to classify the mixing state of the atmospheric layer beneath the lowest observed cloud. The accuracy of this new correlation-based method was compared to two methods of detecting boundary layer decoupling based on radiosonde measurements. Overall, an optimized version of the new methodology correctly determined the mixing state of the below-cloud layer for 76 $\pm$ 4% of the radiosondes available for comparison. Further, it was more accurate than another ground-based metric used to determine the boundary layer mixing state. For the majority of the time series in which the analysis could be applied, the new methodology classified the below-cloud boundary layer as well-mixed (54%), or else fog was present (27%), which indicated that particles observed at the surface often had a direct pathway into low-cloud (81%). In the remaining analysis period, the near-surface atmospheric layer was stable and the layer was decoupled from the overlying cloud (19%). However, forecasts from the Antarctic Mesoscale Prediction System revealed that conditions favouring a well-mixed below-cloud layer or the formation of fog were more frequently satisfied over the open Southern Ocean than those favouring near-surface stability. As a result, aerosol particles measured near sea-level are often tightly coupled to low-cloud formation in the region.*



## Plain Language Summary

Particles suspended in the atmosphere (aerosol) act as seeds for cloud droplet formation. The abundance of such particles directly influences the opacity of clouds, while their physical and chemical characteristics govern if and when those cloud droplets freeze. As a result, both the amount of solar radiation a cloud can reflect and the temperature of waters below are sensitive to the quantity and type of particles available to the cloud. We present a new methodology for understanding the conditions in which low-level clouds have direct access to the large and diverse reservoir of particles in the surface layer. We find that meteorological conditions which transfer particles from sea-level to low-level cloud are satisfied up to 81% of the time over the Southern Ocean. This suggests that the particles we observe near the surface almost always play a significant role in the formation of low-level cloud.


## 1. Introduction

Despite the small scale of aerosol–cloud interactions, errors in how they are represented within global climate models can cause significant climatological biases in the radiative balance. In particular, uncertainties in predicting cloud phase lead to substantial biases in the cold sector of Southern Ocean cyclones (Bodas-Salcedo et al., 2014). While the abundant

cyclones of the Southern Ocean (Irving et al., 2010) occur solely as a function of synoptic conditions, global climate model's predictions of cloud phase in the cold sector of Southern Ocean cyclones (Vergara-Temprado et al., 2018), and in the wider Southern Ocean (Schuddeboom et al., 2019), are extremely sensitive to the properties of particles in the underlying boundary layer. Understanding the conditions in which these particles can reach cloud base is therefore important in correctly predicting a cloud's optical properties.

As wind speeds have increased over the Southern Ocean (Young et al., 2011; Hande et al., 2012a), there is significant interest in how naturally-produced particles impact cloud formation and the optical properties of the resultant clouds (McCoy et al., 2015), and whether this interaction represents a substantial climate feedback (Korhonen et al., 2010). It is well–known that increasing the population of cloud condensation nuclei (CCN) directly increases the opacity of the overlying cloud (Twomey, 1977). Increases in wind speed over the open ocean will enhance the flux of sea spray particles (SSPs) from breaking waves (Hartery et al., 2020a). In most regions of the Southern Ocean SSPs are the only local source of ice-nucleating particles (INPs) (DeMott et al., 2016), a region almost entirely devoid of such particles (Bigg and Hopwood, 1963). While other, more potent, INPs like dust particles may be entrained into the boundary layer in specific seas (e.g. coastal seas near Patagonia), ice nucleating particles collected on Southern Ocean voyages have a much weaker surface activity than dust particles, which reflects the predominant abundance of sea spray (McCluskey et al., 2018). These particles can have a substantial influence on the radiative and physical properties of the resulting cloud. Not only are ice clouds much less opaque (Hu et al., 2010), they are much more likely to precipitate (Borys et al., 2003). Thus, changes in the abundance of SSPs may have significant impacts on cloud radiative properties.

One of the challenges in unravelling aerosol–cloud interactions over the Southern Ocean is that the region is frequently covered in cloud (80% of the time; Haynes et al. (2011)), resulting in a sparsity of boundary layer observations from space. While observational records of radiosondes from Macquarie Island provide rich data on the thermodynamic structure of the Southern Ocean boundary layer (Hande et al., 2012b), a lack of accompanying observations of CCN, INPs, and in situ microphysical properties of low-level cloud leaves a gap in our understanding of how these particles interact with cloud over the Southern Ocean. Previous research, such as the dedicated ACE-1 (Russell et al., 1998), SOCEX (Boers et al., 1998), HIPPO (Wofsy, 2011) and more recently SOCRATES (McFarquhar et al., 2020) campaigns have used aircraft observations to bridge this knowledge gap. However, aircraft can only fly in a limited range of conditions, as the strong vertical wind shear and icing conditions present within boundary layer cloud poses a significant threat. By contrast, ship–based measurements can be made in nearly all conditions. Here, we use measurements on the R/V *Tangaroa* during a voyage to the Ross Sea in 2018 to establish conditions in which particles near the surface are turbulently mixed to cloud base. Establishing conditions when sea-level measurements are relevant to cloud will enable future research to better exploit sea-level measurements in aerosol–cloud interaction studies, and adds value to the growing catalogue of near-surface measurements available from recent voyages.

# 2. Measurements

Over the course of a voyage between New Zealand and the Ross Sea, air was drawn from the mast of the R/V Tangaroa (∼20 m a.s.l.) to a shipping container laboratory (∼2 m a.s.l.) via 40 m of conductive hose. Within the laboratory, a passive cavity aerosol spectrometer probe (PCASP-100X; Droplet Measurement Technologies) and a differential mobility particle sizer (DMPS, TSI) measured the ambient concentration of particles suspended in the

atmosphere (Kremser et al., 2020). The PCASP measured the number concentration size spectra of particles suspended in the boundary layer in 30 size bins (0.1–3.0 $\mu$m) every minute. The DMPS measured the number concentration size spectra in the size range 0.02–0.3 $\mu$m every 10 minutes. Following Modini et al. (2015) and Quinn et al. (2017), we fit three lognormal size distributions to estimate the average diameter and number concentration of Aitken, accumulation and coarse mode particulate. With rare exception, coarse mode particulate is almost entirely composed of sea spray particles (SSPs) in the marine environment (Modini et al., 2015; Quinn et al., 2017); hence, we will refer to the coarse mode as the SSP mode throughout the remainder of this work. The PCASP was used exclusively to estimate the average size and abundance of SSPs, while the DMPS was used for the Aitken and accumulation mode particles. When data from the DMPS were not available, measurements from the PCASP were used to constrain the abundance and size of accumulation mode particles. Further details on sampling set-up and analysis, including correction factors for losses through the sampling line and methods for handling contamination from ship exhaust, are described in Hartery et al. (2020a) and Kremser et al. (2020). In parallel to the size-resolved particle concentration spectra generated by the SMPS and PCASP, the total number of cloud condensation nuclei (CCN) was measured using a CCN counter (CCNC-100; Droplet Measurement Technologies). The CCN counter sampled from the same sampling conduit that drew ambient air to the PCASP and DMPS. A measurement of the average number of ambient CCN was made twice an hour at intervals of 0.1% supersaturation between 0.2–1.0%.

A ceilometer (CHM-15K; Lufft) measured the total power of received light per laser pulse ($\lambda$ = 1064 nm), $P(t,z)$, over the R/V *Tangaroa* every minute at a resolution of 15 m. For each profile, the instrument also estimated the cloud base height, $z_{CBH}$. A raw quality control flag provided by the instrument was used to screen for field-of-view contamination from fog or residual precipitation on the outer optical window. A micro-rain radar (MRR-2; Metek) operated in close proximity was also used to detect and screen for precipitation events.

The NZ MetService's Automated Weather Station (AWS) was positioned above the bridge of the R/V *Tangaroa* at 22.5 m. Relevant measurements included ambient pressure, air temperature, relative humidity, long and shortwave radiation fluxes, wind speed, and wind direction. AWS measurements were corrected to a height of 10 m according to the COARE 3.5 bulk-flux algorithms (Edson et al., 2013) as detailed in Hartery et al. (2020a). The bulk seawater temperature was measured at a depth of 5.5 m below sea level with a thermistor (SBE38; Sea-Bird Scientific). We also used the COARE 3.5 bulk-flux algorithms (Edson et al., 2013) to calculate the sea skin temperature from the bulk temperature, accounting for long and shortwave fluxes (Edson et al., 2013).

Fifty-seven meteorological balloons were launched during the voyage. The radiosondes (iMet-ABx; InterMet) recorded pressure, relative humidity, temperature and wind speed. In quality control, two of the radiosondes were found to have a faulty relative humidity sensor and one had more than one faulty sensor, leaving 54 useful profiles of the boundary layer. The radiosondes were launched approximately twice daily once the ship crossed the 60$^{\text{th}}$ parallel.

Regional meteorological forecasts were downloaded from the Antarctic Mesoscale Prediction System (AMPS). AMPS initializes a new forecast every twelve hours, with subsequent output provided every three hours. AMPS provides forecasts within several nested spatial grids. However, only forecasts for the outermost spatial grid, "domain 1," were used as it was the only grid which fully contained the ship track. Domain 1 has a hor-

izontal resolution of 24 km and is a 544 × 412 grid centred on 90°S. AMPS uses the Mellor-Yamada-Janjic (MYJ) scheme, a 2.5-level closure model of turbulence, to predict the behaviour of the planetary boundary layer (PBL). AMPS calculates the height of the PBL to be the height at which the turbulent kinetic energy falls below a pre-determined threshold (Janjic, 2001). The AMPS data used in this study were downloaded from: `https://www.earthsystemgrid.org/project/amps.html`. To allow for a brief model spin-up, only forecasts between 3–12 hours were used (Jolly et al., 2016).

# 3. Methods

*a. Classification of the Below-Cloud Layer*

The suspended particle cross-sectional surface area, $A$, was calculated from the number concentration size spectra measured by the PCASP:

$$A(t) = \int \frac{\mathrm{d}n(t, D_p)}{\mathrm{d}\log D_p} \pi \left(\frac{D_p}{2}\right)^2 \mathrm{d}\log D_p \tag{4.1}$$

Where $D_p$ is the particle diameter and $n$ is the partial concentration of particles. Note that as this is a correlation-based study, a more exact treatment of the interaction of particulate with light which accounts for both Mie and Rayleigh scattering (e.g. Bohren and Huffman (1983)) is not strictly necessary. In addition, such calculations would necessitate a priori information about particle composition and morphology which were not available for this study. The geometric surface area is dominated by the sea spray and accumulation mode particles (97%, on average; Fig. 4.1d), which the PCASP can readily measure.

To classify the below-cloud layer mixing state, we calculated rolling Spearman Rank correlation coefficients centred on each hour of observation between the sea-level concentration of aerosol surface area, $A(t)$, and the total power of the backscattered light received by the ceilometer, $P(t,z)$. The Spearman Rank correlation coefficient was used as non-linearities related to the two-way transmission of light through an atmospheric layer are likely; however, the Pearson moment correlation coefficient produced qualitatively similar results. Before calculating the correlation coefficients, four quality control measures were implemented to ensure that the calculated correlation coefficients would be meaningful. First, the observations were screened based on the ceilometer's quality control flag and the ship contamination flag described in Kremser et al. (2020). Second, only backscatter retrieved from heights below the 10$^{\text{th}}$-percentile of CBH were studied to prevent contamination from cloud backscatter. Next, we performed a signal-to-noise analysis, where the signal-to-noise ratio (SNR) is defined as follows:

$$\mathrm{SNR} = \frac{P(t,z)}{P_{bg}(t)} \tag{4.2}$$

$P_{b,g}$ is the ceilometer's background signal, which the instrument measures at the end of its laser pulse cycle. We removed any data points from profiles which had a SNR less than two. Following the SNR analysis, the total power of backscattered light detected by the ceilometer, $P(t,z)$, was corrected for the background signal:

$$P_c(t,z) = P(t,z) - P_{bg}(t) \tag{4.3}$$

Following the initial quality control, rolling correlation coefficients were calculated between $A(t)$ and $P_c(t,z)$. This was completed in a two-step process. First, a sub-set of the time-series, $T$, was defined:

$$T = \left\{t_{i-\Delta t/2}, t_{i-\Delta t/2+1}, ..., t_{i+\Delta t/2}\right\} \tag{4.4}$$

where $t_i$ is a specific time in the observation period and $\Delta t$ defines the temporal width of the sub-set around $t_i$. In this work, temporal widths between 1 and 20 hours were studied. As observations were recorded every minute, the sub-set $T$ contained at least 60 data points and at most 1200. Spearman Rank Correlation coefficients, $r_s$, were then calculated as follows:

$$r_s(x,y) = \frac{cov(rank(x), rank(y))}{\sigma_{rank(x)}\sigma_{rank(y)}} \tag{4.5}$$

where $rank(x)$ is a function which assigns an integer ranking to each value of a set $x$; $cov(x,y)$ is the covariance of two sets of data, $x$ and $y$; and $\sigma_x$ is the standard deviation of the set $x$ (Spearman, 1904). Here, $x$ and $y$ are the sub-sets of $A(t)$ and $P_c(t,z)$ defined by $T$. Applying equations 4.4 & 4.5 to the entire time-series forms a matrix, $R_{\Delta t}(t,z)$. A detailed justification of this range of time-scales is provided in the discussion. Two additional post-processing procedures were implemented after the correlations were calculated. If a subset, $T$, contained less than 20 valid data points, then the correlation coefficient was labelled as not a number. For the remaining data, a significance test was performed for each correlation value to ensure that the value was significantly larger than zero ($p < 0.05$). If the calculated correlation coefficient failed the significance test, it was re-assigned a value of zero.

Once the fully quality-controlled correlation analysis had been completed, we developed a simple metric to classify whether the atmospheric layer below cloud was well-mixed with near-surface air. First, the average below-cloud correlation coefficient, $\overline{r_{bc}}$, was calculated. The value of $\overline{r_{bc}}$ was then compared to a threshold value, $r_t$: when $\overline{r_{bc}}$ exceeded the threshold, particles measured near the surface layer were considered to be well-mixed into the overlying cloud. Otherwise, the surface layer was considered to be decoupled from the cloud. If there were insufficient data points in $T$, then the correlation analysis was unable to classify the coupling state between the surface and cloud layer.

*b. Validation*

To validate the proposed methodology and classification metric, we compared results to four separate methods of determining the mixing state of the below-cloud layer. The first two methods were variations on a conventional radiosonde analysis, one was a surface-based method and the final method was a model-based method.

We compared the classification of the below-cloud mixing state according to the correlation metric to two methods for detecting boundary layer decoupling based on radiosonde profiles. The first method searched for maxima in the virtual potential temperature gradient ($\partial\theta_v\ \partial z^{-1}$) (Hande et al., 2012b). If a local maxima in the virtual potential temperature gradient was detected and found to exceed 10 K km$^{-1}$, then the height at which this occurred was labelled as the main inversion, or the boundary layer height. The method then searched for secondary maxima larger than 5 K km$^{-1}$ below the main inversion. If secondary inversions exists, then the boundary layer is decoupled (Hande et al., 2012b). To be consistent with our methodology, which can only classify the atmospheric layer below the lowest observed cloud, the below-cloud layer was only labelled as decoupled if a secondary inversion was located between the surface and the cloud.

A second method for detecting below-cloud decoupling was adapted from Truong et al. (2020). In this method, a main inversion was only identified if a local maximum in the virtual potential temperature gradient exceeded 14 K km$^{-1}$. To detect decoupling, the decoupling parameter $\mu$ was studied (Truong et al., 2020; Yin and Albrecht, 2000). The decoupling

parameter, $\mu$, is defined as follows:

$$\mu = -\left(\frac{\partial\theta}{\partial z} - \frac{0.608\theta}{1+0.608r}\frac{\partial r}{\partial z}\right) \tag{4.6}$$

where $r$ is the water vapour mixing ratio and $\theta$ is the potential temperature. Yin and Albrecht (2000) devised $\mu$ for their study of "transition layers" in the boundary layer, as it is more sensitive to changes in the water vapour mixing ratio than the vertical gradient of virtual potential temperature and is therefore more likely to detect subtle boundary layer features like decoupling. Decoupling of the boundary layer over the Southern Ocean was only detected when a value of $\mu$ exceeded 2.5 times its average value throughout the boundary layer (Truong et al., 2020). To be consistent with our method, we adapted the this method to only classify the below-cloud layer as decoupled if the threshold for $\mu$ was exceeded in the below-cloud layer (Truong et al., 2020). We used a simple optimization methodology to determine which combination of time-scale, $\Delta t$, and correlation threshold, $r_t$, best predicted the state of coupling between the surface and cloud layers as compared to the reference methods (Hande et al., 2012b; Truong et al., 2020).

To provide a benchmark for our methodology, we compared the optimized performance of the correlation-based method against another surface-based methodology for defining the mixing state of the below-cloud layer (Jones et al., 2011). Briefly, if the difference in height between the observed cloud base height (CBH) and lifted condensation level (LCL) exceeded 150 m, then the below-cloud layer was considered to be decoupled from the cloud (and well-mixed otherwise). For these calculations, the LCL was calculated from the AWS measurements, where the LCL represents the height at which a cloud is expected to form based on a model parcel of air adiabatically ascending through a well-mixed boundary layer (Romps, 2017). Here, we used the 1-hour averaged LCL and for consistency, the $10^{\text{th}}$-percentile of CBH within each hour.

While the radiosonde profiles collected throughout the voyage provided a robust benchmark for the new methodology, radiosonde data were available at most twice-a-day. To increase our confidence in the methodology, we compared its classification of the below-cloud layer to near-surface measures of atmospheric stability. We used two measures of near-surface atmospheric stability: the square of the Brunt-Väisälä Frequency, $N$, and the 10-m wind speed. Values of $N^2$ were calculated from the AWS measurements and the COARE 3.5 bulk-flux algorithms:

$$N^2 = \frac{g}{\theta_v}\frac{\partial\theta_v}{\partial z} \tag{4.7}$$

where $g$ is the gravitational acceleration, $\theta_v$ is the virtual potential temperature, and $z$ the height above sea level. This stability analysis was combined with forecasts from AMPS to qualitatively assess the conditions in which aerosol–cloud coupling was expected. As a coarse proxy for aerosol-cloud coupling, we investigated the difference in the LCL and the predicted planetary boundary layer height (PBL) in the AMPS forecasts. If the planetary boundary layer exceeded the lifted condensation level, then aerosol particles measured at the ocean surface were considered well-mixed to the minimum height where cloud could have occurred.

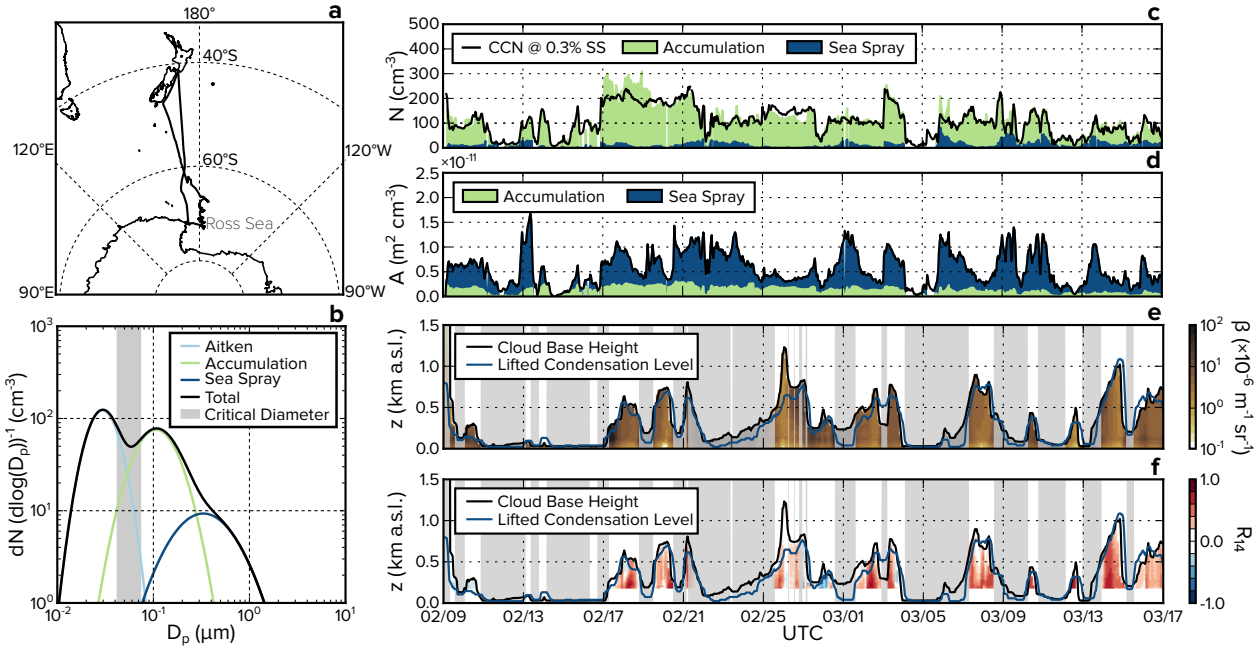


**Figure 4.1 :** (a) The track of the R/V *Tangaroa* during the Marine Environment and Ecosystem Voyage. (b) A typical size distribution for particles in the Southern Ocean. The expected range of cloud activation diameters for marine stratus is shown in grey. (c) The sea-level abundance of sea spray particles (SSPs; blue filled region) and accumulation mode particles (green filled region) is compared to the abundance of cloud condensation nuclei (CCN) at a supersaturation of 0.3% (black line). (d) The abundance of suspended surface area was calculated from the measured particle size distributions (Eq. 4.1). (e) A contour plot of the attenuated backscatter coefficient measured by the CHM-15K ceilometer. The lifted condensation level ($z_{LCL}$) and cloud base height ($z_{CBH}$) are also shown for reference. (f) Spearman Rank correlation coefficients between the sea-level abundance of particulate surface area and ceilometer backscatter are shown. Time periods when the ceilometer optical window was obscured, the cloud base was below 200 m, fog was present, or the aerosol sampling system was contaminated by ship exhaust are shaded.

# 4. Results

## *a. Time Series Analysis*

Throughout the voyage to and from the Ross Sea (voyage track shown in Fig. 4.1a), the number–size distribution of particulate was predominantly trimodal as seen in Fig. 4.1b. The representative number–size distribution shown in Fig. 4.1b was constructed by taking voyage wide averages of the total number, width and median size of the individual modes that were fit to the observations. The appearance of these modes is consistent with previous observations in marine settings (Bates et al., 1998; Quinn et al., 2017). A large majority of the particles in the smallest two modes, the Aitken (30 nm, $\sigma$ = 1.4) and accumulation modes (100 nm, $\sigma$ = 1.6), are thought to be produced as a single mode from homogeneous nucleation of volatile sulfate species, with mode separation occurring as a result of cloud-processing (Hoppel et al., 1986). These particles are nucleated in–situ from the condensation of oxidized marine gasses and grow via self-coagulation and condensation. In contrast, sea spray particles (400 nm, $\sigma$ = 2) are directly generated from breaking ocean waves, and tend to be much larger than particles in the Aitken and accumulation mode (Prather et al., 2013). Note that size statistics presented in this section have been corrected to a relative humidity of 80%. For sulfate and sea spray particles, a particle at a relative humidity of 80% is approximately twice as large compared to when it is dry (Gerber, 1985).

A representative size distribution of particles observed in the Southern Ocean marine boundary layer at a relative humidity of 80% is shown in Fig. 4.1b. The bifurcation of the

Aitken and accumulation modes occurs when these particles pass through non-precipitating cloud, since only the largest particles will be activated (Hoppel et al., 1986). Previous research has shown that the supersaturation of water vapour within nascent marine stratus is relatively modest (<0.3%; Hegg et al. (2009)). An estimation of the activation diameter based on a supersaturation of 0.3%, and a range of particle hygroscopicity parameters is also shown in Fig. 4.1b. The estimation of the range of activation diameter is based on the $\kappa$-Köhler model for a range of expected hygroscopicity values (Petters and Kreidenweis, 2007). This coincides well with the local minimum between the Aitken and accumulation mode.

Fig. 4.1c displays the number of particles in both the accumulation and sea spray modes, as these are the only particles relevant to cloud formation. This is compared to the number concentration of CCN measured at a fixed supersaturation of 0.3%. As expected, these two measurements are highly correlated. Across the entire voyage, SSPs did not comprise a substantial fraction of CCN (14%). However, in the latter half of the voyage we encountered several low pressure systems. These cyclones were accompanied by high winds, resulting in substantial wave-breaking and subsequent SSP generation in the region. This led to an enhanced relevance of SSPs to the total CCN population (20%).

Fig. 4.1d shows the abundance of suspended particle surface area. Despite the relatively low abundance of SSPs, the total amount of particulate surface area is strongly dominated by variations in their abundance. In Fig. 4.1e, the time series of attenuated backscatter profiles measured by a coincident ceilometer is shown, along with rolling averages of cloud base height and the lifted condensation level. As demonstrated both empirically and theoretically, if the difference between cloud base height and lifted condensation level is less than 150 m, the below-cloud layer can be considered well-mixed (Jones et al., 2011). As a result, it is clear that there was significant coupling between the surface layer and overlying cloud for much of the time-series.

*b. New Classification Methodology*

We used the Spearman Rank correlation analysis between suspended particle surface area at sea-level (Fig. 4.1d) and ceilometer backscatter from particles overhead (Fig. 4.1e) to assess whether our measurements at the surface were representative of the below–cloud population of CCN. Fig. 4.1f displays strong correlations between these two quantities over time-scales of 14 hours when fog, precipitation, or contamination from ship exhaust did not inhibit the analysis. This suggests that the Southern Ocean boundary layer was consistently well-mixed throughout this measurement campaign. We note that correlation coefficients could not be calculated below 200 m, as these data typically failed the SNR analysis. While one would normally expect a large backscattered signal close to a lidar, and thus a high SNR, the returning backscatter is not well-aligned with the FOV of the receiving optics in the near-range, resulting in a low SNR. As an additional control, the significance of the calculated correlation coefficients was assessed with a two-way t-test.

*c. Comparison to Radiosonde Analysis*

To validate the correlation analysis and establish the most accurate time-scale for calculating correlation coefficients, we analyzed the 57 radiosonde profiles recorded throughout the voyage. For each radiosonde, we used two gradient methods to detect whether or not the surface layer was decoupled from the cloud layer (Hande et al., 2012b). Out of the 57 radiosondes, three could not be used for analysis due to faulty sensors, and 21 were launched when the cloud base height was below 200 m. In such cases, there was insufficient ceilometer data to perform the correlation analysis, as the power of the returning backscatter was

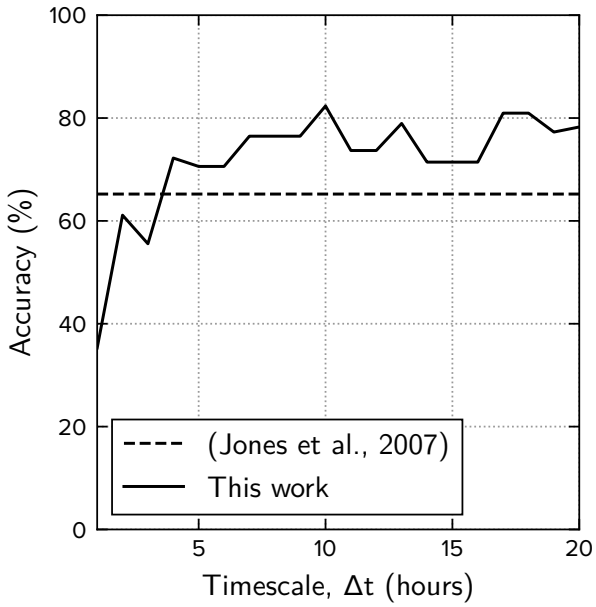


**Figure 4.2 :** The accuracy with which the new correlation metric correctly classified the mixing state of the below-cloud layer for different correlation time-scales, $\Delta t$. The accuracy of the method was calculated in reference to two radiosonde analyses which classifed the mixing state of the below-cloud layer based on thermodynamic gradients (N = 26; non-precipitating conditions, no fog, CBH>200 m) (Hande et al., 2012b; Truong et al., 2020). The accuracy of the proposed method can be compared to the accuracy of another ground-based methodology of determining the state of below-cloud mixing (Jones et al., 2011).

on the same order of magnitude as the instrument noise due to the FOV effects described earlier. In three additional cases, the gradient methods did not detect a boundary layer. As a result, there were only 30 radiosondes available for which the correlation analysis was valid. In the remaining 30 cases, the gradient methods differed only slightly. Overall, the below-cloud layer appeared well-mixed in 83% of profiles according to the criteria of Truong et al. (2020), and 90% of profiles according to Hande et al. (2012b).

The classifications of the below-cloud mixing state by the radiosonde analysis were used to define the optimal time-scale, $\Delta t$, and threshold, $r_t$, for the correlation analysis. For consistency, only the profiles for which both radiosonde methods agreed on the mixing state of the below-cloud layer were used as a reference when calculating the accuracy (N = 26). In Fig. 4.2, the accuracy of the correlation analysis in determining the mixing state of the below-cloud layer is shown as a function of time-scale. Across all time-scales, the threshold for detecting a well-mixed below-cloud layer was $\overline{r_{bc}} > 0$, where $\overline{r_{bc}}$ is the average correlation coefficient between sea-level and the $10^{\text{th}}$-percentile of cloud base height. As a benchmark, we have also shown the accuracy of another ground-based method for determining the below-cloud mixing state (Jones et al., 2011).

Fig. 4.2 demonstrates that the accuracy of the method increases from 35% to 76% as the time-scale increases until time-scales of 7 hours or longer are reached. Differences in accuracy at time-scales beyond 7 hours are negligible considering the sample size (N = 26). The increase in accuracy with increasing time-scale is a direct result of increasing the number of samples in the subset $T$ (defined in Eq. 4.4) used for calculating the correlation coefficient. While shorter time-scales are likely more representative of the time-scale of turbulence, there is also a higher likelihood that the remaining noise in the ceilometer observations will result in weaker correlations which fail the two-way t-test ($p > 0.05$). Increasing the

time-scale results in more consistent correlation coefficients across time-scales and more statistically significant results overall ($|R| > 0$, $p < 0.05$). The accuracy of this method also suggests that despite there being longer time-scale phenomena which could also correlate particulate surface area and backscatter (e.g. frontal systems, convective forcing at cloud top, precipitation, turbulent perturbations of relative humidity, air mass history, etc.), they are not likely to result in substantial misclassification of the below-cloud layer. However, considering that such long time-scale phenomena do exist and may be more prevalent in other regions or observation periods, correlation coefficients calculated over time-scales beyond those presented here should be avoided as false positives and false negatives are likely to become more abundant.

Finally, we compared the accuracy of our new methodology to another method of remotely classifying the below-cloud mixing state (Jones et al., 2011). In this case, the referenced method was only 65% accurate at determining the mixing state of the below-cloud layer, whereas the proposed method was 76% accurate when correlation time-scales greater than 7 hours were considered. While the set of radiosondes for which we could compare both methods was quite limited ($N = 26$), these results suggest that the proposed method more accurately classified the mixing state of the below-cloud layer than the referenced method ($p < 0.05$).

Overall, the correlation analysis found that the below-cloud layer was well-mixed for 14% of the entire time series and poorly-mixed just 5%. Fog was found to occur 7% of the time, where fog was diagnosed when the relative humidity was measured to be 100% and cloud base was less than 50 m. The remaining portion of the time series could not be analyzed, as one or more of the following occurred: the ceilometer's quality control flag was raised; the ship exhaust contaminated the aerosol sample; or, the cloud base was below 200 m but greater than 50 m, such that the entire profile of below-cloud backscatter failed the SNR analysis due to a lack of overlap between the FOV of the ceilometer's optical system and the returning backscatter. While this may seem like a large loss of the time-series, if a given radiosonde was only representative of conditions for the hour of measurements in which it was operating, then the radiosonde analysis provided data for just 7% of the time series. With the proposed correlation analysis, we were able to classify the boundary layer for 26% of the time series, a marked improvement.

*d. Comparison to Stability Analysis*

While the comparison to conventional radiosonde analyses provided some evidence that the correlation analysis accurately classified the below-cloud mixing state, it still seemed prudent to evaluate the analysis against other metrics of atmospheric mixing. Here, we examine expected rates of occurrence for aerosol-cloud coupling based on AMPS forecasts for the period of study.

First, the forecasts were compared to our observations from all available radiosondes, except those with non-functioning RH sensors. Table 4.1 provides a summary of various comparison statistics between forecasts and measurements. The statistics were only calculated below 3 km to restrict the comparison to relevant planetary boundary layer (PBL) and lifted condensation level (LCL) heights. These are presented in Table 4.1.

Overall, all of the selected variables were reasonably well correlated. However, there were minor biases worth mentioning. In Table 4.1, statistically significant biases between modelled and measured values of pressure, dew point temperature, and wind speed were observed ($p < 0.001$). Within AMPS, the height of the PBL is determined according to

**Table 4.1 :** This table summarizes statistics comparing measurements from radiosondes launched throughout the voyage and predictions from AMPS below 3 km (a.s.l.).

| Statistic | P (hPa) | T (K) | $T_d$ (K) | U (m $s^{-1}$) |
|---|---|---|---|---|
| RMSD | 2.0 | 1.2 | 3.2 | 2.7 |
| Bias | 0.3 | – | -0.8 | 0.7 |
| $R^2$ | 1 | 0.96 | 0.87 | 0.74 |

RMSD: Root Mean Squared Deviation

$R^2$: Pearson Correlation Coefficient

the turbulent kinetic energy profile (Janjic, 2001). This implies that the height of the PBL may have been under-estimated by AMPS. The dew point temperature was also negatively biased as a result of the over-abundance of water vapour in the AMPS boundary layer relative to observations. This implies that the LCL was also under-predicted. Still, considering the spatial and temporal scale of the AMPS forecasts, the agreement between model and measured values was quite good, and highly statistically significant ($p < 0.001$).

In Fig. 4.3a, the frequency of occurrence with which the depth of the planetary boundary layer exceeded the lifted condensation level is shown, based on forecasts from AMPS between 40 – 70 S (excluding areas less than 100 km from a coast). The frequency of occurrence is shown as a function of two variables which are often used to describe the stability of the near-surface atmospheric layer: the square of the Brunt-Väisälä frequency, $N^2$, and the 10-m wind speed, $U_{10}$. The results in Fig. 4.3a demonstrate that in near-neutral stability ($N^2 \sim 0$) and weak winds ($U_{10} \sim 0$), the layer below the LCL was less-likely to be well-mixed, as the PBL was too shallow. However, in all other cases, the boundary layer was likely well-mixed. Note that there was still a small percentage of the time when the layer below the LCL was well-mixed despite the near-neutral stability of the surface layer. While a well-mixed boundary layer would not be expected in such cases, the near-surface layer is typically much shallower than the LCL, and is therefore not always a perfect determinant of the mixing state of the entire layer below the LCL. However, it is clear that in most other conditions, the layer below the LCL is almost guaranteed to be well-mixed. Overall, The AMPS analysis in Fig. 4.3a provides a general rule of thumb: if the 10 m wind speed exceeds 8 m $s^{-1}$ then the boundary layer will be well-mixed to the LCL, regardless of the near-surface stability.

In Fig. 4.3c and d, the classification of the below-cloud layer according to the correlation metric calculated over time-scales of 7 and 14 hours is shown. We can see that despite the accuracy with which the correlation analysis at 7 hour and 14 hour time-scales classified the mixing state of the boundary layer (Fig. 4.2), the correlation metric calculated over a 14 hour time-scale provided a more qualitatively consistent result with the AMPS analysis. In comparing Figs. 4.3c & d, it is clear that the correlation metric calculated over a time-scale of 7 hours mis-classified the boundary layer more frequently, as a poorly mixed boundary layer is not expected to occur at all if $N^2 < -5 \times 10^{-3}$ $s^{-2}$ or $U_{10} > 8$ m $s^{-1}$ (Fig. 4.3a). In contrast, Fig. 4.3d shows that the correlation metric at a time-scale of 14 hours classified the below-cloud layer as decoupled only when the stability of the near-surface layer was near-neutral and winds were less than 8 m $s^{-1}$, consistent with the AMPS analysis. While only two time-scales are presented here, analysis at all time-scales longer than 14 hours produced qualitatively similar results. Finally, in Fig. 4.3b, it is clear that fog tended to occur only in both near-neutral stability ($N^2 > -5\times10^{-3}$ $s^{-2}$) and low winds, or stable conditions.

One limitation of this analysis is that cloud is not necessarily guaranteed to occur at the LCL. As such, a direct quantitative comparison between Figs. 4.3a, c & d is not possible, as

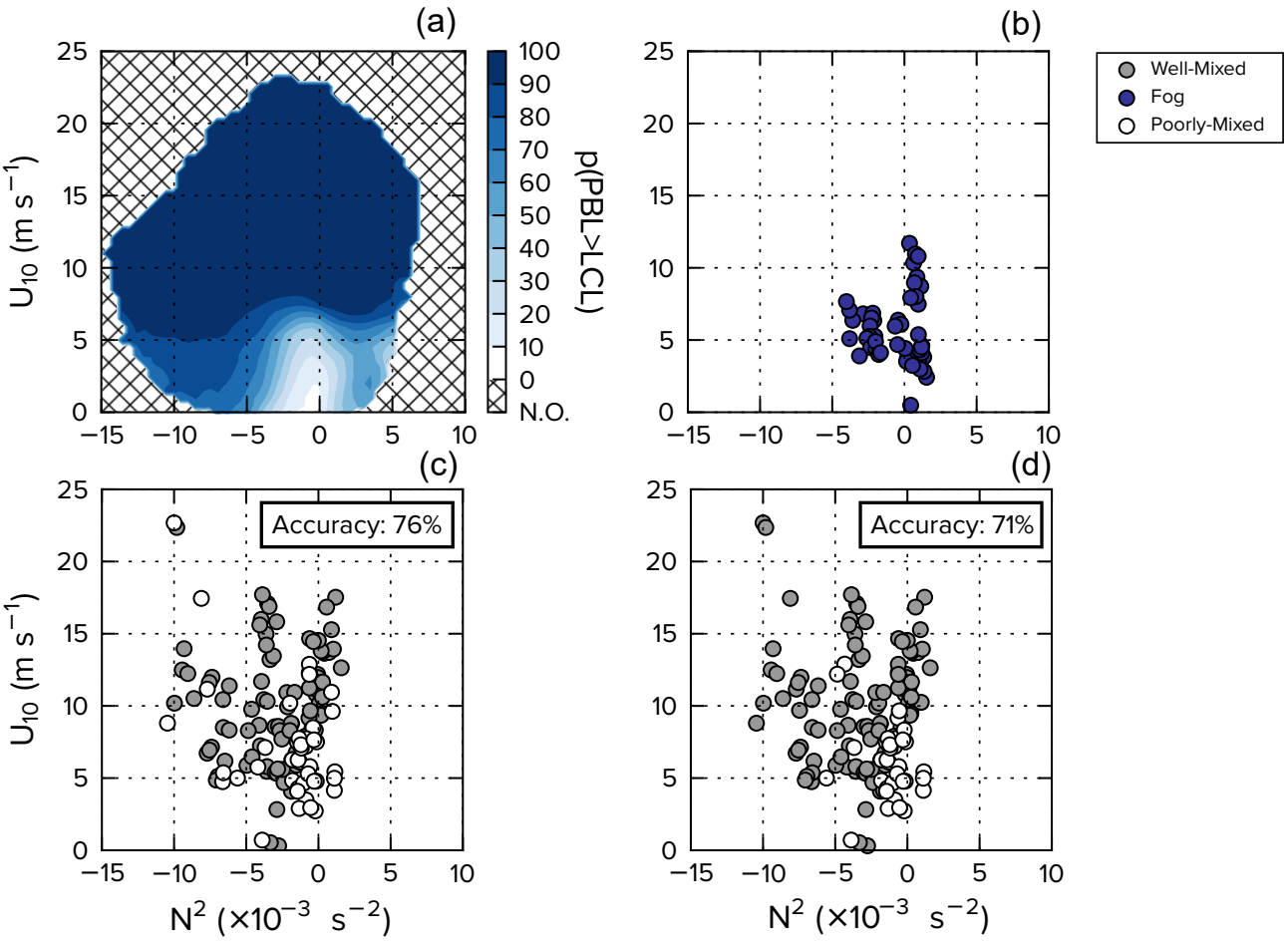


**Figure 4.3 :** (a) The frequency with which the height of the planetary boundary layer (PBL) predicted by AMPS was higher than the lifted condensation level (LCL) over the open Southern Ocean (40–70 S, >100 km from coastline) in February and March of 2018 (N.O. = Conditions occurred less than frequently than 0.001%). (b) The occurrence of fog (CBH < 50 m, RH = 100%). (c) The classification of the below-cloud layer based on correlation coefficients calculated over 7-hour timescales (non-precipitating conditions; CBH > 200 m). The measure of accuracy is in reference to the radiosonde analyses (Fig. 4.2). (d) As in (c), but for a time-scale of 14-hours.

cloud was always occurring in the subset of data we were able to analyze. Still, we found this figure to be a useful qualitative reference for our methodology. In addition, it demonstrates that even though the fraction of the time-series available for analysis via the correlation metric is low (26%; ∼10 days of observations), the conditions encountered within this subset of the data are representative of the wide set of conditions forecast by AMPS. As a result, statistics presented in the previous section can be used to conclude that in non-precipitating conditions, the below-cloud layer over the Ross Sea was likely well-mixed 54% of the time, poorly-mixed 19% of the time, and contained fog 27% of the time.

# 5. Discussion

In this work, we were interested in understanding often aerosol particles measured near the surface of the ocean were relevant to low cloud formation over the Southern Ocean. We proposed a new methodology, based on the correlation of particle surface area and ceilometer backscatter, which identified when aerosol particles observed at the surface were available to the lowest observed cloud. To validate the proposed methodology, we needed an accurate reference classification of the boundary layer against which we could compare our re-

sults. Here, we modified two radiosonde-based methodologies which determine the mixing state of the entire boundary layer (Hande et al., 2012b; Truong et al., 2020). Radiosonde-based methodologies were selected as the preferred reference methodology, as the observations were sensitive to fine thermodynamic changes in the boundary layer. These reference methodologies were modified to simply determine the mixing state of the atmosphere between the surface and the base of the lowest observed cloud. This allowed us to optimize the parameters of our proposed methodology (correlation time-scale, threshold of correlation strength) such that the predicted mixing state of the below-cloud layer best matched the referenced radiosonde methodologies. In the comparison (Fig. 4.2), the proposed correlation-based method correctly classified the mixing state of the below-cloud layer 76 $\pm$ 4% of the time for correlation time-scales greater then 7 hours. The accuracy of our method was then compared to a more simple metric for classifiying the mixing state of the below cloud layer, which was only accurate 65% of the time (Jones et al., 2011).

In a more qualitative comparison (Fig. 4.3), the classification of the below-cloud mixing state by the proposed methodology was also shown to be consistent with surface-based measurements of atmospheric stability and model predictions of turbulence in a wide range of conditions. The high accuracy of the new methodology's predictions in comparison to radiosonde-based methods, in situ observations of near-surface atmospheric stability, and model forecasts of boundary layer turbulence gives us high confidence that the proposed method is accurate even when reference data is not available.

With the accuracy of our proposed methodology validated against mutliple methods of determining the below-cloud mixing state, we can compare statistics to previous observations in the Southern Ocean. We find that while the below-cloud layer was often well-mixed, this was not always guaranteed. It is well-known that the marine boundary layer can stratify into a near-surface boundary layer and a sub-cloud layer (Garratt, 1994). In fact, radiosondes launched from Macquarie Island (54.62°S, 158.85°E) over the past two decades found that the boundary layer was well-mixed just 17.8% of the time (Hande et al., 2012b). In contrast, our time series analysis showed that in non-precipitating conditions, the below-cloud layer was well-mixed 54% of the time. This seems to be in stark contrast to the accuracy data presented in Fig. 4.2. However, the difference in frequency of occurrence comes primarily from a difference in the definition of decoupling. The method presented in this work was only designed to detect whether the boundary layer was well-mixed up to the lowest cloud. In contrast, the referenced method was originally designed to detect decoupling throughout the entire boundary layer (Hande et al., 2012b). However, multi-layer clouds are frequently observed over the Southern Ocean (Hande et al., 2012b). In such settings, the inversion atop the lowest cloud will tend to decouple the atmospheric layer beneath the cloud from the rest of the boundary layer. However, the surface is likely still coupled to the lowest cloud, as cloud was often present in the atmospheric layer beneath the decoupling height (Hande et al., 2012b). As previously described, we modified the radiosonde-based methodology (Hande et al., 2012b) to only classify the below cloud layer as decoupled if a secondary vitural potential temperature inversion occurred below the cloud. The accuracy data presented in Fig. 4.2 highlights that after this modification, classifications of the below-cloud mixing state from thhe proposed and referenced methodologies agree.

Overall, the results from the correlation analysis highlight that particles are almost always available to the lowest cloud (Fig. 4.1f). The percentage of time in which aerosol-cloud coupling occurred within the valid section of our time series is simply the sum total of the rates of occurrence of fog and a well-mixed below-cloud layer: 81%. Forecasts from AMPS

tend to agree, as the layer of the atmosphere below the LCL was found to be well-mixed 84% of the time over the Southern Ocean throughout February and March of 2018. As Kuma et al. (2020) noted, the ability to correctly predict the occurrence of low cloud is a critical necessity for improving the Southern Ocean shortwave radiation bias. The proposed method increases our understanding of these low clouds and the particles which help form them.

For instance, we found that the number of CCN at a supersaturation of 0.3% was consistent with the number of particles in the accumulation and sea spray mode. As a supersaturation of 0.3% is the expected water vapor supersaturation within marine stratocumulus (Hegg et al., 2009), this suggests that sea-level observations may provide a good constraint on the number of cloud droplets in a wide variety of conditions. We found that despite being readily-available to nascent clouds, sea spray particles were typically outnumbered by smaller, cloud-processed accumulation mode particles (Fig. 4.1c), consistent with previous studies (Quinn et al., 2017). However, in addition to abundance, the ice-nucleating ability of particles is known to be a strong determinant of cloud phase and albedo: a climate model which determined the primary nucleation of ice within low-level clouds according to the abundance and type of boundary layer ice-nucleating particles found that predictions of cloud opacity were significantly more accurate in the cold sector of Southern Ocean cyclones relative to simpler glaciation schemes (Vergara-Temprado et al., 2018). Though less numerous than accumulation mode particles, sea spray particles act as weak ice-nucleating particles (DeMott et al., 2016) in a region that is often devoid of more potent ice nuclei (e.g. dust) (McCluskey et al., 2018). This study highlights that sea spray particles are available to many more cloud systems than just within the cold sector of cyclones. As a result, climate models which implement glaciation schemes that connect the primary nucleation of ice to the microphysical properties of aerosol particles will likely see more widespread improvement to the Southern Ocean shortwave radiation bias. It also highlights that should models adopt more complex models of cloud glaciation, then they must also more carefully parameterize the flux of sea spray particles (Hartery et al., 2020a).

The new method does not come without limitations, however. Depending on the FOV of the ceilometer's optical receiver, the ability of the analysis to analyze below-cloud coupling in low cloud settings (CBH $< 200$ m) can be severely impaired. In addition, though we have provided a reasonably comprehensive validation of the appropriate time-scale for calculating correlation coefficients and the threshold for classification of the below-cloud layer, there are potentially instances where the correlation analysis could trigger false positives and false negatives in other synoptic settings. These include, but are not limited to, frontal systems, convective forcing at cloud top, precipitation, turbulent perturbations of relative humidity, air mass history, etc. Still, given the accuracy of the methodology as quantitatively compared to the radiosonde analyses, and qualitatively to a forecast analysis, we are confident in the results presented as they pertain to this specific region and period of study. As an added benefit, the proposed method uses instruments which function nearly autonomously, with little need for oversight or on-site personnel. In contrast, radiosonde programs require highly-trained personnel and can only be launched is a limited set of meteorological conditions. It becomes exceedingly difficult to successfully launch a radiosonde once winds surpass 15 m $s^{-1}$, or aboard a research vessel in unfavorable wave conditions. As a result, statistics of boundary layer mixing collected from radiosonde programs are likely skewed towards calm conditions. Finally, it is worth mentioning that there are likely unintended, negative consequences of leaving irretrievable sonde packages in the Southern Ocean.

# 6. Conclusions

In this work we presented a new technique for determining the state of boundary layer mixing based on the value of the Spearman Rank correlation coefficient calculated between sea-level observations of suspended particle surface area and ceilometer backscatter. When data was available, these correlations were often high, implying that particles measured at sea-level were well-mixed throughout the boundary layer and were therefore readily-available to nascent, low-level cloud. From this analysis, a simple metric was created to diagnose whether coupling occurred or not. This revealed that in non-precipitating conditions the boundary layer was well-mixed 54% of the time, contained fog 27% of the time, and was poorly-mixed just 19% of the time. This simple metric based on the correlation analysis was compared to two conventional radiosonde analyses. The correlation-based metric accurately classified the mixing state of the boundary layer 76% of the time, a noticeable improvement over the accuracy of a simpler ground-based method (65%). In addition, the frequency of occurrence of below-cloud mixing estimated by the correlation-based metric was qualitatively consistent with an analysis of mixing based on the near-surface stability within regional forecasts. We estimate that aerosol will have a direct pathway into low cloud either through a well-mixed below cloud layer or surface-level fog, 81% of the time when clouds are present. Thus, in situ sea-level observations of particulate offer substantial insight into cloud formation over the Southern Ocean in a wide set of conditions.

# Ice-Nucleating Particles over the Southern Ocean


## Abstract

*A new, approximate method for generating climatologies of ice-nucleating particles is leveraged to study the indirect radiative effects of sea spray particles over the Southern Ocean. Results indicate that a substantial fraction of the shortwave radiation bias over the Southern Ocean could be resolved by improving the parameterization of primary ice nucleation within global climate models. In addition, the strengths of sea spray radiative feedbacks within low-level mixed-phase cloud are estimated. It is demonstrated that a temperature-dependence within the parameterization of sea spray flux creates a radiative feedback loop which accelerates regional warming.*


## 1. Introduction

The Southern Ocean is a region almost devoid of ice-nucleating particles (INPs) (Bigg, 1973). These particles are typically made of solid material like mineral dust or organic detritus from microorganisms at the sea surface and initiate phase changes within cloud when they come in contact, or become immersed in super-cooled cloud droplets (Niedermeier et al., 2011). The few INPs observed in the Southern Ocean region are largely thought to be made of wind-swept organic detritus that become entrained within sea spray particles when waves break (DeMott et al., 2016; Vergara-Temprado et al., 2017). Recent observations have shown that the total number of INPs observed in the marine boundary layer can be predicted by the total surface area of sea spray particles (SSPs), supporting the idea that INPs in the region are wind-swept organic detritus from the sea surface (McCluskey et al., 2018). The phase of low-level cloud, and thus its opacity, are fundamentally connected to the abundance of such particles. Recent modeling studies have shown that the amount of shortwave radiation reflected by Southern Ocean clouds is very sensitive to a model's prediction of low-level cloud phase (Bodas-Salcedo et al., 2016). As INPs are the seeds of phase transition within cloud, the optical properties of these clouds are thus tied to the number of INPs available to them (Vergara-Temprado et al., 2018).

This thesis has confirmed not only the correct magnitude of sea spray fluxes, but established conditions in which these particles are available to low-level cloud. The correlation analysis presented in Hartery et al. (2020b) demonstrated that the boundary layer is frequently well-mixed, allowing nascent low-level Southern Ocean cloud to access the reservoir of cloud condensation and ice nuclei available within the boundary layer. In Hartery et al. (2020a), in-situ measurements were used as a baseline reference for model parameterizations, showing that global climate models that use the Gong (2003) (hereafter G03) model of sea spray flux severely over-estimated the amount of SSPs available in the boundary layer. Thus, while parameterizations of cloud phase improve substantially when primary ice nucleation is directly tied to seed particle characteristics (Vergara-Temprado et al., 2018), this may also introduce a substantial sensitivity to the abundance of SSPs within global climate

models. In this study, a simple method for generating short-term climatologies of SSPs is outlined. From this climatological analysis, the sensitivity of the shortwave reflectivity of low-level Southern Ocean cloud to parameterizations of the flux of SSPs, and their role as ice nucleating particles, will be studied.

# 2. Measurements

In situ measurements of suspended particles presented in this study have been described in Chapter 2 along with relevant quality control measures. The "wet" particle diameters of the PCASP-100X and GRIMM measurements were translated to a dry diameter basis using the parameterization of Gerber (1985). It was assumed that the PCASP-100X measured particles at ambient relative humidity, while the GRIMM, which was placed after the diffusion drier, measured particles at a relative humidity of 50%. A probability density function was then derived from the measurements after averaging them across the observation period. A sea spray mode was fit to the particle size distribution, as in Hartery et al. (2020a). The PDF was normalized by the total number of SSPs in this SSP mode.

A particle collection system was installed near the bridge of the Tangaroa (∼15 m a.s.l.). It consisted of a rain shelter, below which a single-use filter assembly was fixed in place. The filter assembly consisted of a Thermo-Scientific filter holder and polycarbonate membrane filter. Air was continuously drawn through the filter holder via a pump. After 24–48 h the pump was turned off, the filter assembly was removed, and a new filter assembly was installed. A gas meter placed in-line with the pump was used to calculate the total volume of air which passed through the filter paper. This volume varied according to exposure time, but was generally between 15–20 $m^3$. The collected filters were individually sealed and frozen for the remainder of the voyage (-20°C). Three blank filters were collected throughout the voyage. Over the entire voyage, 34 filters were collected (31 samples + 3 blanks). Many were damaged from precipitation and soot from the ship stacks. However, a shorter collection time was simply not feasible, as INPs are so sparse in the Southern Ocean boundary layer. Following the voyage, samples were sent to Colorado State University for processing. The methodology for counting INPs on filters is outlined in McCluskey et al. (2017). Finally, the number of INPs counted on the filters at a given temperature was normalized by the total dry surface area of SSPs measured by the PCASP-100X throughout the period to calculate the nucleation site density.

In this chapter, measurements of cloud droplet number size distributions measured during the second Southern Ocean Cloud Experiment (SOCEX) will be re-analysed. These were collected with a Forward Scattering Spectrometer Probe (FSSP) mounted on the wing of an aircraft. The aircraft departed and returned to Hobart, Australia, on 9 flights over the course of January and February, 1995 (Boers et al., 1998). The FSSP is an optical particle counter very similar in design to the PCASP-100X, providing measurements of cloud droplets with diameters in the range 2 – 47 $\mu$m. Thresholds for liquid water content (LWC > 0) measured by a King probe and the ambient relative humidity (RH > 90%) were used to screen each flight for clouds. The cloud droplet size spectra measured under these conditions were then averaged across the 8 flights for which data was available. Finally, a modified gamma distribution was fit to the data to approximate the average size distribution of droplets in low-level Southern Ocean cloud.

Forecasts from the Antarctic Mesoscale Prediction System (AMPS) were used as input data to pseudo-Lagrangian particle dispersion calculations as well as synoptic information to contextualize the results. The AMPS forecasts were generated by a polar variant of the

Advanced Weather and Research Forecasting model (WRF) on several domains of varying spatial extent and resolution (Bromwich et al., 2005; Powers et al., 2012). Only the widest domain was used, which has a resolution of 24 km $\times$ 24 km, as it includes the majority of the Southern Ocean. The AMPS forecasts were also used to generate cyclone-centered composites for several scalar forecast variables. The cyclone-centered forecasts were generated by searching for local minima in the surface pressure field. A 1000 km $\times$ 1000 km swath of data was then extracted around the center of the cyclone. These swathes were averaged over time. Only swathes with a center <1000 km from the R/V *Tangaroa* were included in the average.

As the primary goal of this study is to understand the sensitivity of low-level Southern Ocean cloud to the availability of ice nuclei in the boundary layer, it is also necessary to develop a climatology for the abundance of dust particles. The flux of dust particles (described later) is typically confined to arid regions with little vegetation. To identify these regions, monthly composites of the Normalized Difference Vegetation Index (NDVI) reported by the Advanced Very High Resolution Radiometer (AVHRR) were downloaded for February and March, 2018 from `https://ladsweb.modaps.eosdis.nasa.gov/`. The 0.05 $\times$ 0.05 degree values were sorted into the Antarctic Mesoscale Prediction system domain via nearest neighbour search.

Finally, observations of cloud optical thickness and cloud top height data from MODIS Terra and Aqua satellites were downloaded from: `https://ladsweb.modaps.eosdis.nasa.gov/`. These observations were used to generate zonal averages of cloud occurrence. The 1 km $\times$ 1 km measurements of cloud optical thickness and cloud top height were sorted into the AMPS domain via nearest neighbour search with no averaging.

# 3. Modeling

*a. Pseudo-Lagrangian Particle Dispersion*

To estimate the abundance of particles observed at a given location, two frames of reference are common. The Eulerian frame, standard within global climate models, discretizes the atmosphere into a connected grid and models the movement of material from cell-to-cell according to turbulence, diffusion, convection and advection. Thus, the Earth is the reference frame. In contrast, a Lagrangian model simulates the movement of an air parcel throughout the connected grid. Turbulence, diffusion, etc. are still applied, but now the air parcel is the frame of reference. Here, Lagrangian trajectories are described using the meteorological variables and grid of AMPS.

Along the Lagrangian trajectory, the change in the particle concentration within the air parcel, $dN$, is simply related to the volume flux of material into the grid-cell, $F_v$. However, recall that in Hartery et al. (2020b), the Southern Ocean boundary layer was often well-mixed. Thus, one could equivalently calculate the change to the particle concentration within the air parcel according to the interfacial air–sea flux $F_A$ into a grid-cell of base area, $A$, and volume, $V$:

$$\begin{aligned} \frac{dN}{d\mathcal{P}} &= F_v \\ \frac{dN}{d\mathcal{P}} &= \frac{A}{V}F_A = \frac{1}{h}F_A \end{aligned} \tag{5.1}$$

where $h$ is the height of a layer in contact with the ocean surface and $d\mathcal{P}$ is the length of time the parcel spends within this layer, where the surface layer is defined to extend from 0–100

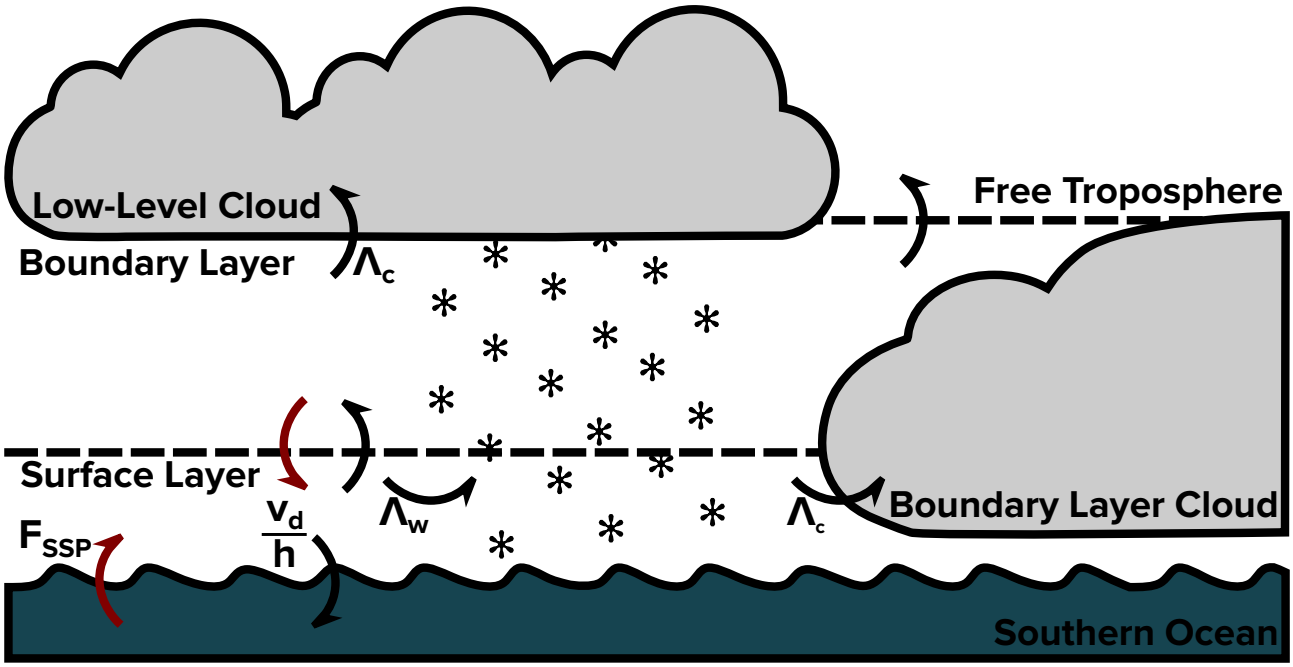


**Figure 5.1 :** An illustration of sources (red) and sinks (black) of SSPs within the Southern Ocean boundary layer.

m a.s.l. (Hartery et al., 2020a), and is always assumed to be turbulent. This assumption can be validated with AMPS, which estimates that the boundary layer over the Southern Ocean is deeper than 100 m, 88% of the time. Along its trajectory, particles emitted from the ocean surface only mix into the air parcel if it's within the surface layer. To estimate the abundance of particles, Eq. (5.1) is integrated over the Lagrangian path from some initial time $t_i$ to the observation time $t_0$:

$$N = \frac{1}{h} \int_{t_i}^{t_0} F_A d\mathcal{P} \tag{5.2}$$

However, to generate a climatology of particle abundance, one must simulate the back trajectory of at least one air parcel per grid-cell of the meteorological domain across a long period. Within FLEXPART-WRF, this would lead to a substantial computational footprint. Instead, a simplifying assumption is made. It is assumed that the center, $(x, y)$, of an air parcel follows surface winds:

$$\begin{aligned} \frac{dx}{dt} &= u_{10}(x, y, t) \\ \frac{dy}{dt} &= v_{10}(x, y, t) \\ U_{10} &= \left( {u_{10}}^2 + {v_{10}}^2 \right)^{\frac{1}{2}} \end{aligned} \tag{5.3}$$

This is not necessarily true and ignores features like the Ekman spiral. However, the goal of this study is not to create a standard climatology for the region, but to study the effect of parameterizations within a simple framework.

Variations in the deposition fields along the Lagrangian trajectories are accounted for in a similar manner to FLEXPART:

$$\begin{aligned} \frac{dM}{dt} &= -\left(\frac{v_d}{h} + \Lambda_w + \Lambda_c\right) M \\ \Lambda_w &= AI^B \end{aligned} \tag{5.4}$$

where $M$ is the abundance of particle mass, $v_d$ is the dry deposition velocity of the particles, $\Lambda_w$ is the mass scavenging rate of particles by precipitation, $I$ is the precipitation rate, A and B are coefficients for estimating mass scavenging by precipitation, and $\Lambda_c$ is the mass scavenging rate by cloud. To calculate $\Lambda_w$, the precipitation rate predicted by AMPS was used along with the scavenging parameters listed in Hartery et al. (2020a). For $\Lambda_c$, the mass, $M$, was set to 0 if the near-surface relative humidity surpassed 95%, as in-cloud activation is efficient and nearly instantaneous (Hertel et al., 1995). As in the Unified Model, a critical relative humidity less than 100% is used to identify cloud structures, since the spatial resolution of the AMPS domain results in a lower frequency of occurrence for total saturation than in reality.

To calculate the grid-cell residence time, $d\mathcal{P}$, FLEXPART-WRF assigns an initial mass to the air parcel, which is altered along the Lagrangian trajectory according to Eq. (5.4). The meteorological time step, $dt$, is then scaled by the ratio of the present value of $M(t)$, to its initial mass, $M_0$ to calculate the sensitivity $d\mathcal{P}$:

$$d\mathcal{P} = \frac{M}{M_0} dt \tag{5.5}$$

This approach reduces the influence of particles further upwind from the measurement according to the strengths of the various particle removal mechanisms along the Lagrangian trajectory. Since the mass $M$ is always scaled by the initial mass $M_0$, the selection of $M_0$ is arbitrary. For this reason, $M_0$ was set to 1. Ultimately, this method will over-estimate the amount of time particles spend within the boundary layer as it does not account for boundary layer detrainment (see Fig. 5.1). To estimate this loss, the length of time particles spent in the surface layer was measured as a fraction of the time spent in all atmospheric layers throughout the FLEXPART-WRF simulations presented in (Hartery et al., 2020a). This fraction, $f$, was then parameterized according to the length of the back-trajectory, where:

$$f = \frac{f_0}{1 + \left(\frac{t_0 - t}{t_{1/2}}\right)} \tag{5.6}$$

where $f_0$ and $t_{1/2}$ are the maximum fraction of time spent and the half-life of particles in the surface layer. These values were calculated to be 0.12 and 41 hours. Thus, the length of time particles spend within the surface layer now becomes:

$$d\mathcal{P} = f\frac{M}{M_0} dt \tag{5.7}$$

Finally, the change in concentration of SSPs along the Lagrangian path can be calculated:

$$\frac{dN}{dt} = \frac{f}{h}\frac{M}{M_0} F_{SSP}(1 - C_{ice}) \tag{5.8}$$

where $C_{ice}$ is the fractional coverage of sea ice and land, and $F_{SSP}$ is a parameterization of sea spray flux. The initial positions of all of the simulations are located at midpoints of the AMPS grid-cells. The system of equations is then integrated backwards through time from $t_0$, to 48 hours prior.

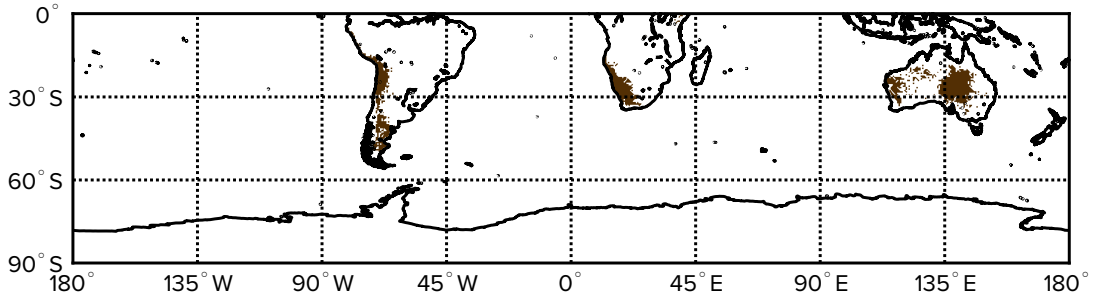


**Figure 5.2 :** A land mask showing potential dust-emitting regions. These were located using the NDVI reported by the AVHRR through February and March of 2018. Only grid-cells with an NDVI less than 0.15 are assumed to emit dust.

The modeled concentrations of SSPs generated by the pseudo-Lagrangian Particle dispersion model (PLPDM) are compared to the measured values presented in Hartery et al. (2020a) in Table 5.1. However, the predicted concentrations of SSPs are clearly biased low relative to the measured values. The bias stems from the fact that the average rates of deposition are also encapsulated by the factor, f. Tracking deposition was necessary, however, to capture the large spatial and temporal variability in the deposition fields. To remove this bias, the predicted concentrations from the new parameterization (Hartery et al., 2020a) (hereafter H20) within the PLPDM are normalized to the observations. This is a valid approach, as this parameterization has already been validated with FLEXPART-WRF, which is a much more robust model. This normalization factor is also applied to predictions from the Gong (2003) (G03) and the Jaeglé et al. (2011) parameterizations (hereafter J11) of sea spray flux. Overall, the PLPDM does a reasonable job of capturing the variance in the observations, considering that the coefficient of determination between the more sophisticated LPDM results and the observations was 0.67 in Hartery et al. (2020a).

*b. The Availability of Dust Particles*

It is well known that dust particles are much more efficient ice nuclei than SSPs (DeMott et al., 2010). Characterizing the availability of ice nuclei to low-level Southern Ocean cloud thus requires a reasonable approximation of the abundance of these particles in the region. Here, the flux of dust particles from continental regions is predicted according to Ginoux et al. (2001). It is assumed that these particles are emitted as a log-normal mode, with a median diameter, $d_{p,m}$, of 1 $\mu$m and a width, $\sigma$, of 2 following the observations of Niemand

**Table 5.1 :** Statistical comparisons between the predicted abundance of sea spray particulate and the measured values presented in Hartery et al. (2020a). Measurements took place in the Southern Ocean during the 2018 Marine Environment and Ecosystem Voyage. The normalized bias is a re-calculation of the model bias after normalizing the predicted abundance from H20 to the observations. $R^2$ is the square of the Pearson correlation coefficient.

| $F(U10)$ | $R^2$ | Bias | Normalized Bias |
|---|---|---|---|
| New Parameterization | 0.35 | 0.37 | 1 |
| Gong (2003) | 0.33 | 0.65 | 1.8 |
| Jaeglé et al. (2011) | 0.19 | 0.19 | 0.51 |

et al. (2012). Thus, the flux is given by:

$$\begin{aligned}\frac{\partial f}{\partial \log(d_p)} &= \frac{C{U_{10}}^3}{\sqrt{2\pi}\log(\sigma)} e^{-\frac{(\log(d_p)-log(d_{p,m}))^2}{2\log^2(\sigma)}} \\ F &= C{U_{10}}^3\end{aligned} \tag{5.9}$$

Where $C$ is a coefficient. Dividing the mass coefficient of $1\times10^{-9}$ kg s$^2$ m$^{-5}$ given by Ginoux et al. (2001) by the mass per particle, gives a value for C of $8.3\times10^3$ s$^2$ m$^{-5}$. Equation (5.9) simplifies the original formulation by not accounting for variations in local topography and surface moisture, which govern the abundance of available surface dust and the threshold velocity for entrainment, respectively (Ginoux et al., 2001). As in Ginoux et al. (2001), emissions of dust particles are restricted to arid regions based on the Normalized Difference Vegetation Index (NDVI) reported by the Advanced Very High Resolution Radiometer (AVHRR). Thus, the pseudo-Lagrangian particle dispersion calculation in Eq. (5.8) becomes:

$$\frac{dN_{DUST}}{dt} = \frac{f}{h}\frac{M}{M_0} F(U_{10}) C_D \tag{5.10}$$

Where $C_D$ is a land mask isolating regions with an NDVI less than 0.15. A contour plot in Fig. 5.2 is shown which identifies these regions.

*c. Estimating Ice Nuclei Concentrations*

The probability, $P$, that a particle of a specific diameter, $d_p$, will freeze can be determined by Poisson counting statistics, where (Vergara-Temprado et al., 2017):

$$\begin{aligned}a &= \pi {d_p}^2 \\ n_{i,x} &= e^{\alpha_x(T-273.15)+\beta_x} \\ P &= 1 - e^{-an_{i,x}} \\ &\approx an_{i,x}, \qquad\qquad (an_{i,x} \ll 1)\end{aligned} \tag{5.11}$$

where $n_{i,x}$ is the nucleation site density for particles of type $x$ (McCluskey et al., 2018; Niemand et al., 2012). For a given size distribution of particles of type $x$, $dn\ (d\log d_p)^{-1}$, the total concentration of ice nuclei, $N_{INP}$, is thus:

$$\begin{aligned}N_{INP,x} &= \int_\infty^\infty P \times \frac{dn}{d\log d_p} d\log d_p \\ &\approx \int_\infty^\infty n_{i,x} a \frac{dn}{d\log d_p} d\log d_p \\ &\approx \int_\infty^\infty n_{i,x} \pi {d_p}^2 \frac{dn}{d\log d_p} d\log d_p \\ &\approx n_{i,x} A_x \\ N_{INP} &= \sum_j n_{i,x} A_x\end{aligned} \tag{5.12}$$

where $A_x$ is the abundance of suspended surface area provided by particle of type $x$ (see Appendix A4), $N_x$ is the total number of particles of type $x$, and $j$ is a dummy variable that iterates over all available INP types. The assumed microphysical characteristics of sea spray and dust particles are presented in Table 5.2. Note that the ice-nucleating efficiency of a particle depends on the dry diameter. However, the pseudo-Lagrangian particle dispersion

calculations predict the size and abundance of particles at a relative humidity at 80%. To calculate the dry particle surface area, the dry particle diameter is calculated from the diameter at a relative humidity of 80% according to the empirical formulae described in Gerber (1985). Thus, the median particle diameter of 0.4 $\mu$m at 80% RH represents a dry diameter of 0.25 $\mu$m.

*d. Optical Characteristics of Low-Level Cloud*

Here, it is assumed that low-level clouds over the Southern Ocean obey the inverse relationship observed by Vergara-Temprado et al. (2018):

$$SW = SW_0 - \gamma \log(N_{INP}) \tag{5.13}$$

Where $SW$ is the amount of shortwave radiation reflected by low-level clouds (W m$^{-2}$), $N_{INP}$ is the concentration of INPs (L$^{-1}$) calculated in the previous section, and $SW_0$ and $\gamma$ are parameters which describe Eq. (5.13) for different cloud types. As the actual shortwave radiation budget results from clouds at all heights, absolute budgets will not be presented, only differences between two models. Thus:

$$\Delta SW = \gamma \log \left( \frac{N_{INP}}{\hat{N}_{INP}} \right) \tag{5.14}$$

where the diacritic $\hat{}$ is used to differentiate between two methods of predicting $N_{INP}$. Vergara-Temprado et al. (2018) noted that there were two distinct classes of clouds within their study with two separate values of $\gamma$, 2.6 and 5.7, and suggested that the latter is more common among Southern Ocean cloud. Differences in the shortwave reflectivity were only calculated if the abundance of INPs was in the range $1\times10^{-12}$–$1\times10^{0}$ L$^{-1}$ and only if the cloud temperature was below zero. Below or above the thresholds, the cloud will be super–cooled or completely glaciated, respectively.

To benchmark improvements to the description of INPs, the ice nucleation concentration within the global climate model needs to be estimated. According to Furtado and Field (2017), the mixed-phase parameterization in the Unified Model nucleates a mass of $1\times10^{-11}$ $kg_{ice}$ $kg_{air}{}^{-1}$ at a temperature of -10°C. However, converting this to an abundance of INPs requires assumptions about the cloud droplet size distribution. When describing the cloud droplet size distribution it is typical to use the modified gamma distribution:

$$\frac{dn}{dd_d} = \xi {d_d}^{\mu} e^{-\Lambda {d_d}^{\gamma}} \tag{5.15}$$

where $\xi$, $\mu$, $\Lambda$, and $\gamma$ are parameters which control the shape of the distribution. It is assumed that cloud droplets follow such a distribution and that ice nucleates evenly throughout the distribution. Then, the number of ice nuclei, $N_{INP}$ is calculated by re-arranging the following

**Table 5.2 :** Microphysical properties of INPs.

| $x$ | Sea Spray (SSP) | Dust (DUST) |
|---|---|---|
| $d_{p,m}$ ($\mu$m) | 0.25[a] | 1[c] |
| $\sigma_p$ | 2[a] | 2[c] |
| $\alpha$ | -0.545[b] | -0.517[c] |
| $\beta$ | 1.0125[b] | 8.934[c] |

[a] This work; [b] McCluskey et al. (2018); [c] Niemand et al. (2012)

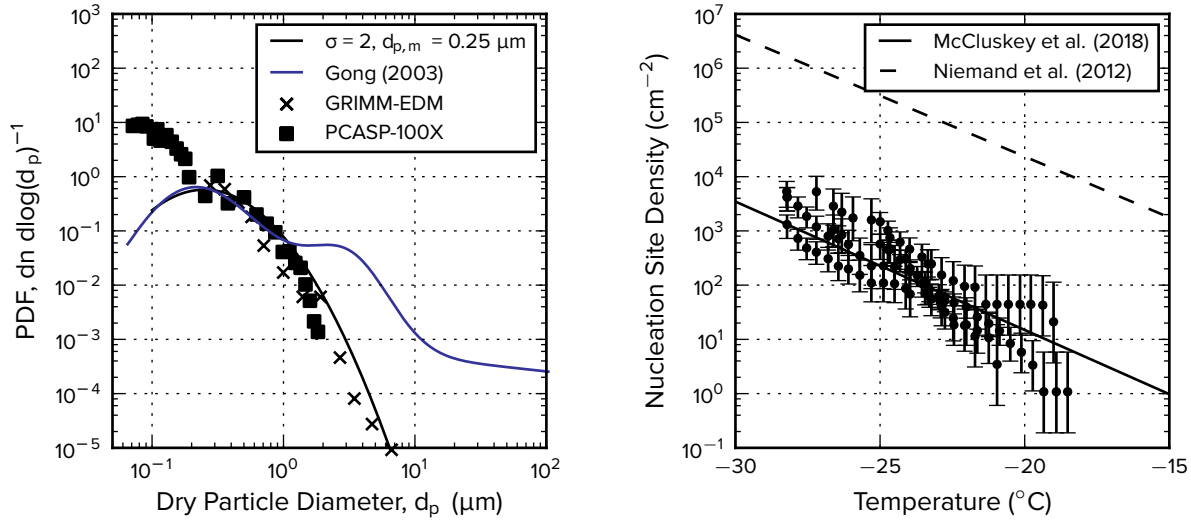


(a) (b)

**Figure 5.3 :** (a) The dry particle number size distribution over the entire observation campaign normalized by the concentration of SSPs. The mode dry diameter of the size distribution was ∼0.25 $\mu$m, while the ambient median diameter was ∼0.4$\mu$m. Corrections for diameter as a function of ambient RH were calculated according to Gerber (1985). Measurements from both the GRIMM and PCASP-100X are included. The normalized size distribution predicted by G03 is shown for comparison. (b) The number of nucleated ice crystals in a filter sample was measured as a function of temperature. This number was then divided by the average amount of available sea spray surface area to estimate the nucleation site density (NSD). Parameterizations of the NSD for sea spray and dust particles are shown (McCluskey et al., 2018; Niemand et al., 2012).

equations:

$$\begin{aligned} M &= \rho \nu N_{INP} \\ M &= w_0 \frac{P - e_w}{R_d T} \end{aligned} \tag{5.16}$$

where $\nu$ is the volume of ice generated per ice-nucleating particle (see Appendix A4), $\rho$ is the density of ice, $w_0$ is the initial seed mass of ice, $P$ is the pressure at cloud base, $e_w$ is the saturation vapour pressure of water, $R_d$ is the gas constant for dry air and $T$ is the temperature at cloud base.

# 4. Results

*a. Microphysical Properties of Sea Spray and Cloud Droplets*

As the number of INPs available to cloud depends on particle surface area, it is highly sensitive to parameterizations for the size distribution of particles. In Fig. 5.3 the probability density function of the number size spectra observations throughout the 2018 Marine Environment and Ecosystem Voyage is shown. The sea spray mode observed in Hartery et al. (2020a) is clearly outlined by the PCASP-100X and GRIMM observations. The spectra is presented as a function of the dry particle diameter. Dry particle diameter was calculated from the wet diameter according to the empirical parameterization given by Gerber (1985), since particle-bound water has little influence over the ice-nucleating ability of a particle. Note that the median dry diameter of the PDF is equivalent to a wet diameter of 0.4 $\mu$m when using the parameterization of Gerber (1985), consistent with the result presented in Hartery et al. (2020a). These observations, and the log-normal size distribution fit to them, are compared to the probability density function of G03. The PDF of G03 only fits the sea spray mode well below 1 $\mu$m. Above 1 $\mu$m it predicts many more large particles. While

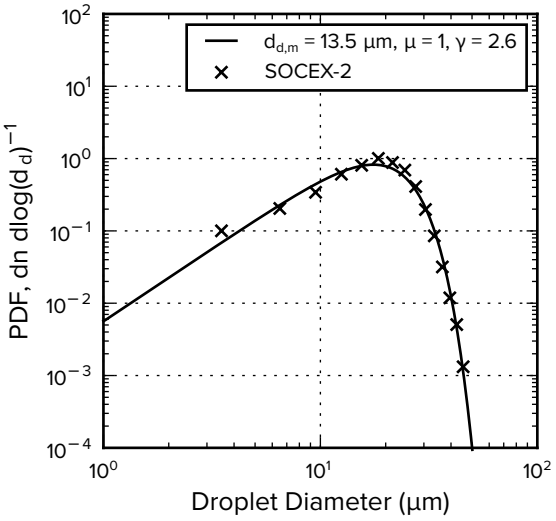


**Figure 5.4 :** A modified gamma distribution is fit to average cloud droplet size data from the Forward Scattering Spectrometer (FSSP). Data were collected during the second Southern Ocean Cloud Experiment, which took place in January and February of 1995 Boers et al. (1998).

these don't contribute substantially to the overall number of particles (7%), they dominate surface area (99%).

To quantify the number of INPs available to cloud, air samples were drawn through filter paper over 24–48 hours. The number of INPs collected on the filter were then measured at varying nucleation temperatures. Out of the 34 filter samples collected over the course of the voyage (31 samples + 3 blanks), only four were suitable for analysis. The rest had suffered some degree of wetting from precipitation, or soot-staining from ship stack emissions. Each of the filters analyzed had only been exposed for 24 hours, which minimized potential contamination but also led to greater measurement uncertainty. Measurements of the number of ice nucleation sites on the filters are shown in Fig. 5.3. The number of sites detected on a filter was divided by the total volume of air sampled by the filter to estimate the average concentration of INPs. This average was then normalized by the average amount of dry sea spray surface area measured by the PCASP-100X throughout the sample period to estimate the nucleation site density. It is clear that the density of ice nucleation sites is predicted well by the parameterization of McCluskey et al. (2018), supporting their conclusion that these INPs are produced by sea spray. For reference, the nucleation site density of dust particles is also shown (Niemand et al., 2012), which demonstrates that they are much more efficient INPs.

In order to estimate the number of INPs implicitly defined within the Unified Model, the typical cloud droplet size distribution observed within low-level clouds must be characterized. The Forward Scattering Spectrometer Probe (FSSP) measurements presented in Fig. 5.4 were made during the second Southern Ocean Cloud Experiment (SOCEX) in 1995. An average cloud droplet size distribution was fit to the average of all of the in-cloud measurements, finding values for the parameters $d_d$, $\mu$ and $\gamma$ of 13.5 $\mu$m, 1, and 2.6, respectively. Provided the clouds over the Southern Ocean are well-described by this standard droplet distribution, then according to Eq. (5.16), the initial seed mass of ice within the Unified Model is roughly equivalent to a number concentration of INPs of $\sim 4 \times 10^{-3}$ L$^{-1}$.

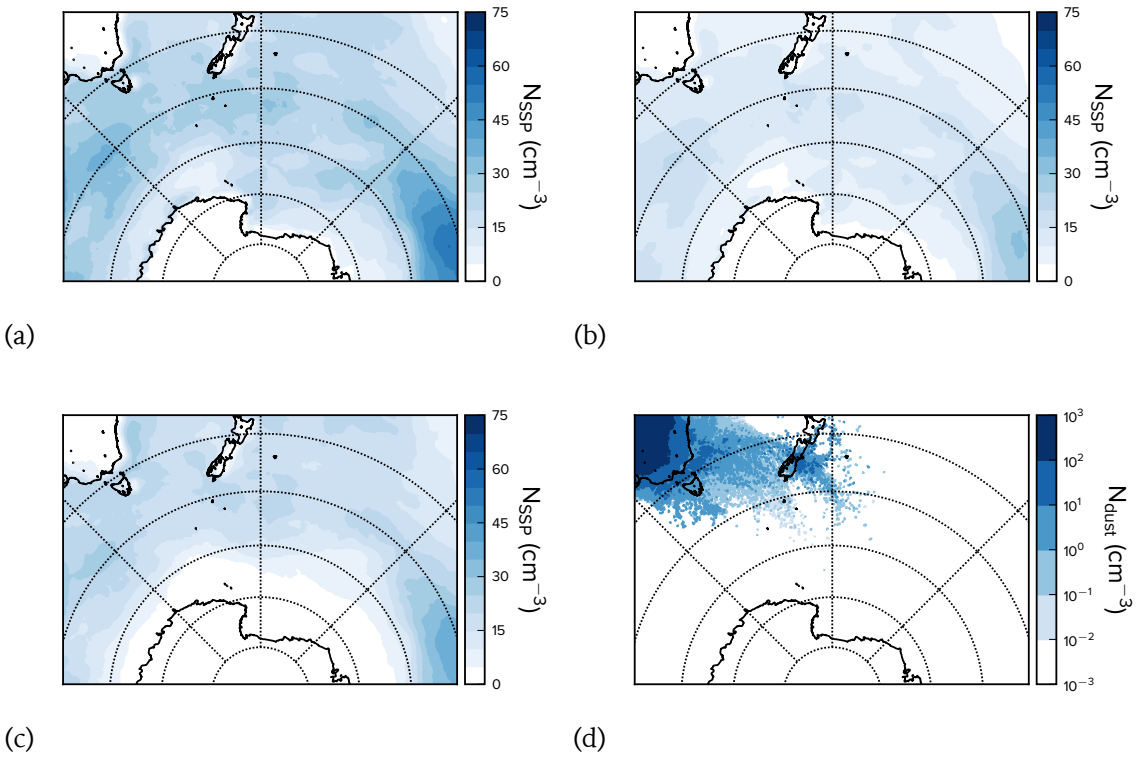


**Figure 5.5 :** (a) Pseudo-Lagrangian particle dispersion calculations were exploited to estimate the average abundance of SSPs (SSPs) based on model G03 for sea spray flux. (b) H20 (c) J11 (d) The average abundance of dust particles.

*b. Climatology of Sea Spray and Dust Particles*

Estimates for the abundance of sea spray particles within the Southern Ocean boundary layer were calculated for three different parameterizations describing the flux of these particles from the ocean surface. Examining the resultant climatological estimates of SSPs presented in Fig. 5.5a–c, SSPs are clearly most abundant between 50–60°S, regardless of which parameterization is used. Further south, SSPs are less abundant due to the lack of time back-trajectories spend over open waters. Further north, the wind speed over the ocean is less intense. The number of particles predicted by the new parameterization proposed in Hartery et al. (2020a), H20, and G03, typically differed by a factor of 1.8×. In contrast, predictions from J11 estimate that there are fewer SSPs in the boundary layer than estimated by H20 (0.47×).

We also find that despite being much more efficient ice nuclei (Fig. 5.3), wind swept dusts from Australia, Patagonia, and Africa are rarely present in the Southern Ocean boundary layer, consistent with other modeling studies (Vergara-Temprado et al., 2017; Ginoux et al., 2001). As a result, primary ice nucleation in low-level Southern Ocean cloud appears to be controlled by the abundance of SSPs.

*c. Cyclone-centered Analysis*

Recently, it has been observed that the largest biases in shortwave radiation between model and satellite estimates occur in the cold sector of Southern Ocean cyclones (Bodas-Salcedo et al., 2014; Vergara-Temprado et al., 2018). To understand whether this is related to the availability of INPs to clouds in this sector, the thermodynamic structure of a cyclone which passed by the R/V *Tangaroa* from March 1 – 2, 2018 is examined. The center of the cy-

clone was determined as the local minimum in surface pressure predicted by the Antarctic Mesoscale Prediction System (AMPS) as seen in Fig. 5.6a. Various scalar fields were then composited by re-centering them to the center of the cyclone and then averaging over time. These are presented in Fig. 5.6b–h.

From Fig. 5.6b it is obvious that the cold sector of the cyclone was to the southwest of the center, while the warm sector was to the northeast. As air moves clockwise about the center of Southern Hemisphere cyclones, warm surface air in the NE moved into the SE sector, where it cooled and saturated to form fog (see Fig. 5.6c). The lifted condensation level was thus very close to the ground in the warm sector, but higher everywhere else.

As expected, the highest near-surface winds occurred where the surface isobars were most closely packed. This occurred to the north of the cyclone center, near the cold front (Fig. 5.6e). As the height of the planetary boundary layer is mostly a function of the available turbulent kinetic energy (Janjic, 2001), this resulted in a deep planetary boundary layer within the warm sector (Fig. 5.6f).

In Fig. 5.6g, particle back-trajectories calculated by FLEXPART-WRF are shown for a particular observation on March 1, 2018 at 1500h. Though the back-trajectory shows that observations in the cold sector are sensitive to the region of the cyclone with the highest winds (see Fig. 5.6e), particles generated by those winds were advected through the low-level fog to the east of the cyclone center seen in Fig. 5.6c. These particles were thoroughly scavenged by the fog, resulting in low concentrations throughout the cold sector of the cloud (Fig. 5.6h).

To understand whether or not these particles significantly influenced the properties of low-level cloud, the criteria developed in Hartery et al. (2020b) were applied. In Fig. 5.7a, the average difference between the planetary boundary layer height and the lifted condensation level is shown across all of the cyclones encountered over the voyage. It demonstrates that in all sectors of the cloud, the planetary boundary layer was higher than the LCL. Overlain on this contour plot is the position of the R/V *Tangaroa* relative to the cyclone center. The position marker is colored according to the correlation analysis presented in Hartery et al. (2020b). Analysis of available ceilometer data showed that the boundary layer was either well-mixed (red) or fog was present (blue), as there were no observations of poor mixing (gray). Hence, SSPs were available to low-level cloud in all sectors of the Southern Ocean cyclones encountered throughout the Marine Environment and Ecosystem Voyage.

The number of INPs available to low-level cloud is not just a function of the abundance of sea spray and dust particles, but also the temperature of the cloud itself. In Fig. 5.7b the number of INPs available at the lifted condensation level is shown. Despite there being fewer SSPs in the SW sector than the NW sector, the difference in temperature between these two regions resulted in more INPs being available to cloud in the SW sector.

With this established, the sensitivity of low-level mixed-phase cloud to changes in the primary ice nucleation parameterization was calculated (Eq. 5.14). In Fig. 5.7c the difference in shortwave reflectivity of low-level mixed-phase clouds is shown. This is compared to the shortwave reflectivity for a fixed value of the ice nuclei concentration of $4\times10^{-3}$ $L^{-1}$, a value determined based on the average cloud droplet size distribution observed in low-level Southern Ocean cloud during the SOCEX campaign and the initial seed mass of primary ice within the Unified model (Furtado and Field, 2017).

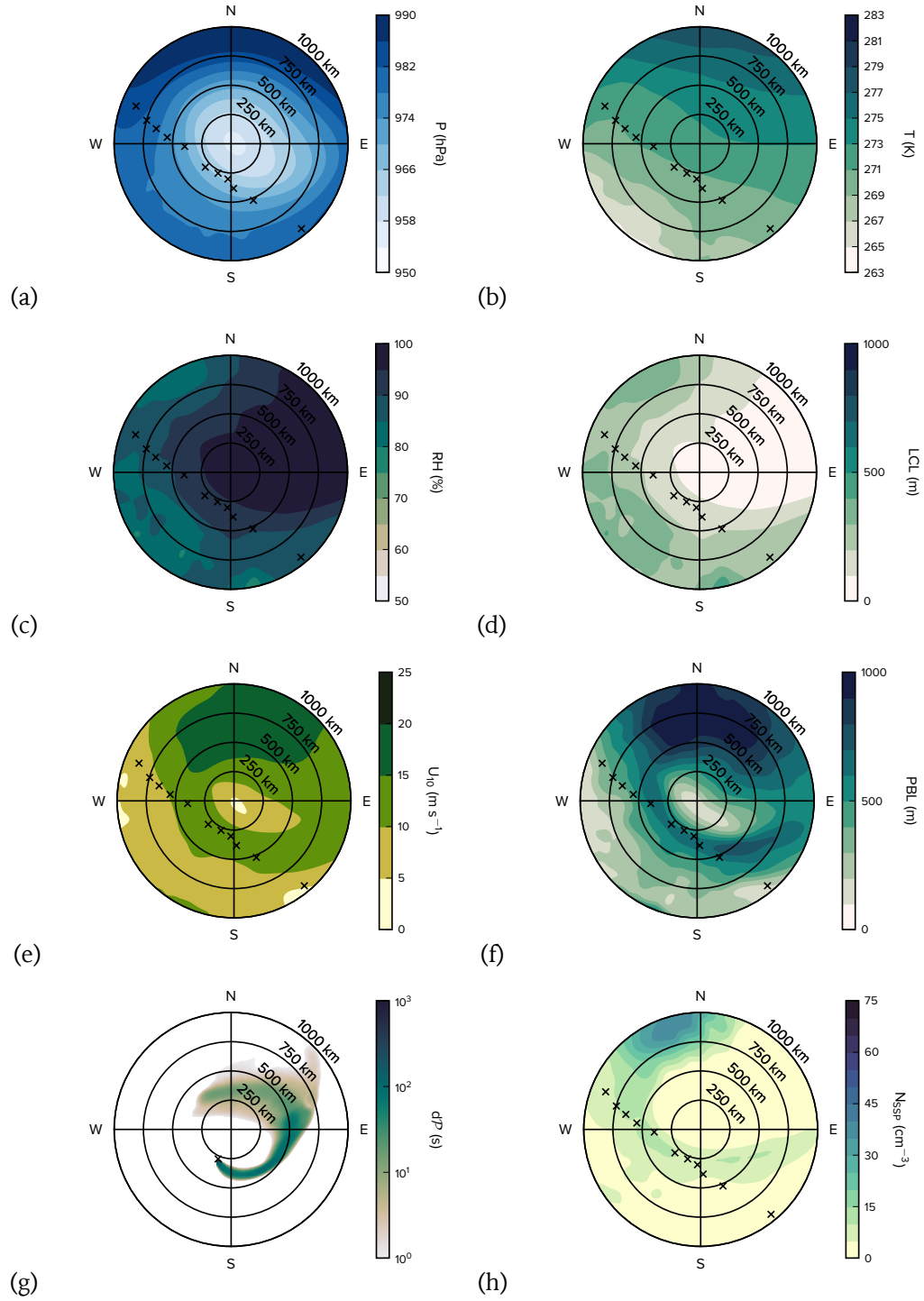


**Figure 5.6 :** Cyclone-centered composites for a Southern Ocean cyclone that passed by the R/V *Tangaroa* on March 1st–2nd, 2018. In each composite the ship location is marked by the × symbol. (a) Surface pressure. (b) Air temperature at 22.5 m. (c) Relative humidity at 22.5 m. (d) The lifted condensation level. (e) The wind speed at 10 m. (f) The difference between the planetary boundary layer height and the lifted condensation level. (g) The cumulative time particles spent below 100 m a.s.l. along 48-hr back-trajectories modeled by FLEXPART-WRF. (h) The total number of SSPs predicted by the pseudo-Lagrangian trajectory calculation.

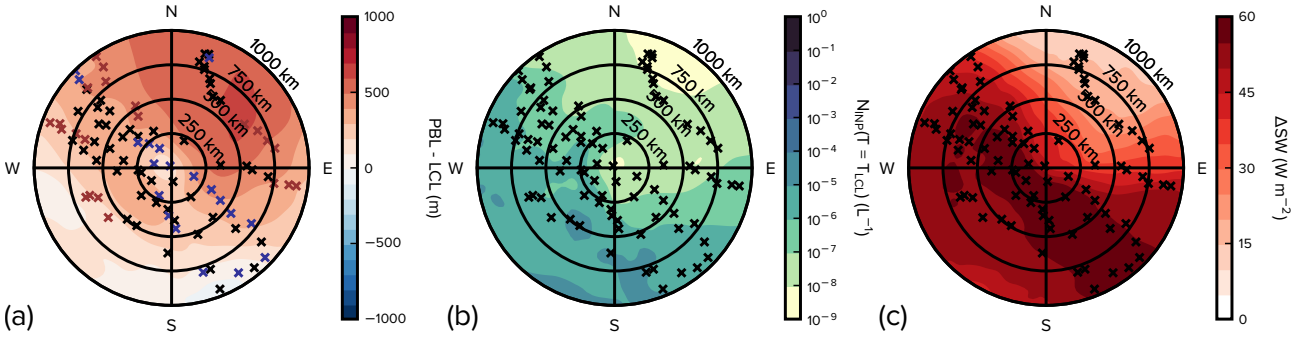


**Figure 5.7 :** (a) The difference between the height of the Planetary Boundary Layer (PBL) and Lifted Condensation Level (LCL) predicted by AMPS. The track of the R/V *Tangaroa* is colored corresponding to whether the boundary layer was well-mixed (red), poorly-mixed (gray), fog was present (blue), or the ceilometer was obscured by accumulated precipitation on the optical window (black). (b) The abundance of ice-nucleating particles at the temperature of the lifted condensation level, $T_{LCL}$, calculated from the PLPDM analysis. (c) The difference in shortwave reflectivity of low-level mixed-phase cloud. Differences were calculated between a proposed model, which varies the initial seed mass of ice nucleated within mixed-phase clouds according to the number of available ice-nucleating particles (b), versus the current model (Furtado and Field, 2017), which nucleates a fixed seed mass of ice. Differences are only calculated where mixed-phase clouds can occur ($T_{LCL} < 273.15$).

Differences are only calculated where mixed-phase cloud is expected to occur ($T_{LCL} < 273.15$ K). As a result, the largest differences are in the colder sectors of the cloud. As identified previously, differences in the shortwave reflectivity of low-level mixed-phase clouds are small in the warm sector (Vergara-Temprado et al., 2018). Within this region, mixed-phase cloud is less likely to occur (see Fig. 5.6d).

*d. The Southern Ocean Radiation Bias*

To generate a more robust comparison between parameterizations of sea spray flux and their predictions of INPs (Fig. 5.5), estimates of sea spray particle abundance from the more robust dispersion model, FLEXPART-WRF were used. In Fig. 5.8a ice nuclei concentrations predicted by G03 and H20 are compared directly to filter sample observations. In general, the number of INPs generated by H20 closely matches the observations. In contrast, G03 over-predicts the concentration of INPs by a factor of 20×.

Consequently, the net change to the shortwave reflectivity of Southern Ocean clouds is dependent on which parameterization of sea spray flux a model implements. In Fig. 5.8b, the net change to the shortwave reflectivity of low-level mixed-phase cloud over the Southern Ocean is presented. In generating this comparison, the predicted difference in shortwave radiation calculated in Eq. (5.14) was multiplied by the zonal cloud occurrence rate derived from MODIS observations. The ranges shown in Fig. 5.8 reflect the different sensitivities, $\gamma$, to ice nuclei concentrations observed by Vergara-Temprado et al. (2018). Estimations of $\Delta$SW are given for the existing parameterization of sea spray flux within the Unified Model, G03, and the new model, H20.

Overall, the difference between using a fixed value of primary nucleated ice and calculating it with the empirical approximation in Eq. (5.18) is stark, with some clouds near 65°S seeing differences of up to 30 W $m^{-2}$. To put this result into context, the model–satellite shortwave radiation bias observed by Kay et al. (2016) is also shown, noting that this bias was observed in the Community Earth System Model, not the Unified Model. Despite this, biases of this magnitude are present among all global climate models that participated in the Cloud Feedback Model Inter-comparison Project (Trenberth and Fasullo, 2010). From

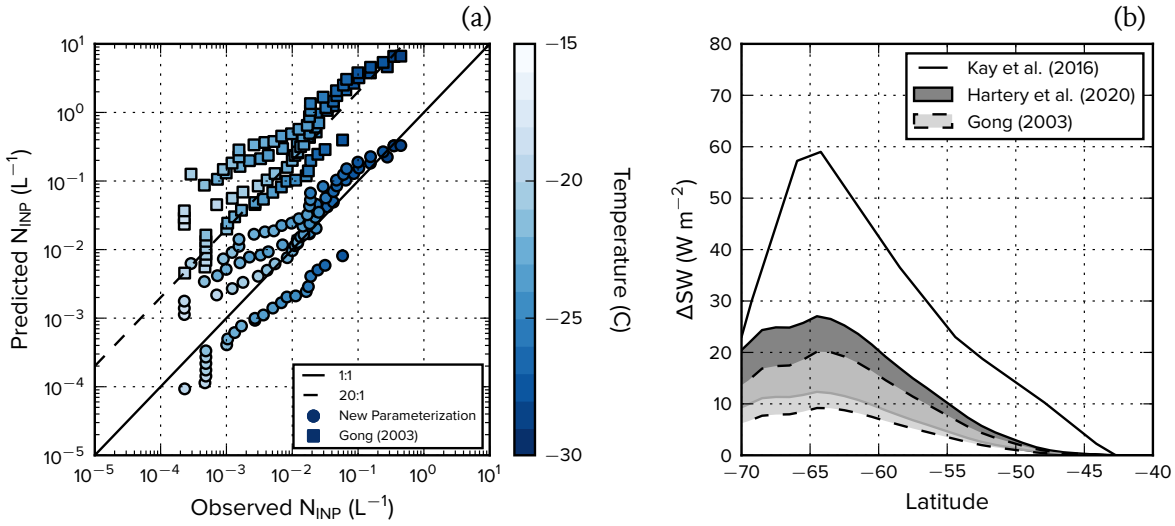


**Figure 5.8 :** (a) The number of INPs predicted by a new parameterization of sea spray flux (H20; Hartery et al. (2020a)), and old parameterization of sea spray flux (G03; Gong (2003)) and the ice-nucleating ability of those particles (McCluskey et al., 2018). (b) The zonal mean difference in shortwave radiation reflected by Southern Ocean cloud when assuming a constant initial seed mass, versus predicting the concentration of ice nuclei based on the different parameterizations of sea spray flux.

this comparison, it is apparent that changing the primary ice nucleation parameterization within the Unified model could potentially resolve a sizable fraction of the shortwave radiation bias. The same calculation based on predictions of the number of SSPs generated by G03 is also shown. In general, the clouds reflected 10 W $m^{-2}$ less shortwave radiation as G03 produced more ice-nucleating particles.

*e. The Sensitivity of Low-Level Southern Ocean Cloud to Climate Perturbations*

As the abundance of SSPs has been implicated in climate feedback loops (Korhonen et al., 2010), it would be useful to leverage this framework to understand the extent to which SSPs can moderate or accelerate warming. To do this, the sea spray particle climatologies were re-generated after increasing near surface wind speeds and sea surface temperatures by 1 m $s^{-1}$ and 1 K. The differences in shortwave reflectivity for these perturbations are shown in Fig. 5.9. Increasing the wind speed resulted in more SSPs in all parameterizations. Despite large differences in the dependence of sea spray fluxes on wind speed among the parameterizations, there weren't substantial differences between the resulting sensitivities shown in Fig. 5.9, indicating that for every 1 m $s^{-1}$ increase to the surface wind speed, shortwave reflectivity will decrease by at most 1.5 W $m^{-2}$. This results from the wind-speed component of the G03 and H20 parameterizations being approximately tangent to each other at 10 m $s^{-1}$, which is the average wind speed over the Southern Ocean.

However, J11 adds another environmental sensitivity, as the flux of sea spray is also a function of sea surface temperature. The magnitude of this sensitivity is similar in magnitude to the sensitivity observed for wind speed. Each of these sensitivities represents a positive feedback loop, whereby the increase in SSPs leads to a decrease in the shortwave reflectivity of low-level, mixed-phase clouds.

*f. A Single-Moment Model of Primary Ice Nucleation*

As the new model of sea spray flux produces reasonable concentrations of SSPs (Hartery et al., 2020a), and INPs (Fig. 5.8a), it would be useful to generate a new parameterization

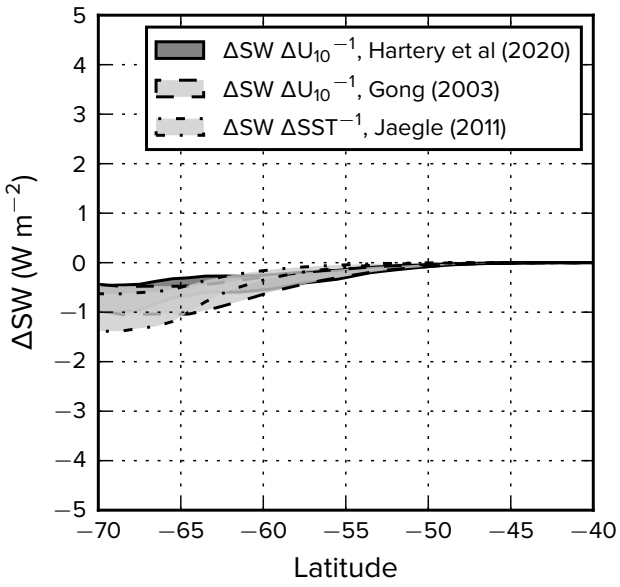


**Figure 5.9 :** Small variations in near-surface wind speeds and sea surface temperature were applied to the AMPS data to generate hypothetical future climates. The resulting differences in the number of boundary layer ice-nucleating particles generated by these future climatologies were then used to estimate changes to the shortwave reflectivity of low-level mixed-phase cloud. $\Delta$SW $\Delta U_{10}{}^{-1}$ indicates the change in shortwave reflectivity for an increase to near-surface wind speeds of 1 m s$^{-1}$, while $\Delta$SW $\Delta$SST$^{-1}$ indicates a change for an increase to sea surface temperature of 1 K.

for the seed mass of ice to be used in single-moment microphysical models. First, Eq. (5.16) is rearranged to generate an expression for $w_{0,x}$, the contribution to the seed mass $w_0$ from INPs of type $x$:

$$w_{0,x} = \rho\nu\, A_x N_x n_{i,x}\, \frac{R_d T}{3(P-e)} \tag{5.17}$$

To calculate $\nu$ and $A$, microphysical parameters describing the ice-nucleating efficiency of sea spray and dust particles were used along with values of $d_p$, and $\sigma_p$ from the PCASP-100X measurements and values of $d_d$, $\gamma$ and $\mu$ from the FSSP measurements (See Table 5.2 and Fig. 5.3c). Thus, the total mass of primary ice nucleated within a cloud is:

$$\begin{aligned} w_0 =& \rho\frac{R_d T}{P-e_w}\left(c_{SSP}N_{SSP}e^{-0.545(T-273.15)} + c_{DUST}N_{DUST}e^{-0.517(T-273.15)}\right) \\ \approx& \rho\frac{R_d T}{P-e_w}\left(c_{SSP}N_{SSP} + c_{DUST}N_{DUST}\right)e^{-0.531(T-273.15)} \end{aligned} \tag{5.18}$$

where $c_{SSP}$ and $c_{DUST}$ are $3.5\times10^{-26}$ and $1.6\times10^{-21}$, respectively. As expected, the initial seed mass is substantially more sensitive to the number of available dust particles, as they are larger and more efficient ice nuclei (Niemand et al., 2012). For a relatively small abundance of dust particles, 100 L$^{-1}$, the initial seed mass is of the same order of magnitude as the default value of $w_0$ within the Unified Model. Despite this, dust particles are rarely present even in small quantities within the Southern Ocean boundary layer (see Fig. 5.5d). Consider that the average abundance of sea spray particles was always observed to be less than 100 cm$^{-3}$. Even at this upper limit, the amount of ice nucleated by equation 5.18 would be just 5% of the amount that is currently nucleated in the Unified model.

# 5. Discussion

Results from global climate models suggest that cold sector Southern Ocean clouds are more sensitive to changes in the parameterization of ice nucleation than clouds in the warm sector, which seem to be modeled well (Bodas-Salcedo et al., 2016; Vergara-Temprado et al., 2018). The results from the cyclone-centered analysis can explain the physical source of these biases. For one, the cold sector is aptly named: the relatively cool near-surface temperatures and lack of moisture in the cold sector give rise to colder, higher clouds. In contrast, mixed-phase cloud is much less likely to occur in the warm sector, which is dominated by warm fog. Thus, changes to the abundance of INPs won't significantly affect the optical properties of low-level cloud in the warm sector.

Differences between the shortwave radiation reflected by mixed-phase clouds can also be significant depending on a model's underlying assumptions about INPs. In Fig. 5.7b the average difference in shortwave reflectivity of low-level mixed-phase cloud between the two assumptions about primary ice nucleation was shown. The first assumption, made by the Unified Model, is that the initial seed mass of ice nucleated in a mixed-phase cloud is fixed at $1 \times 10^{-11}$ $kg_{ice}$ $kg_{air}{}^{-1}$, which is equivalent to $4 \times 10^{-3}$ INPs per liter of air. When the number of INPs was calculated according to the abundance of sea spray and dust particles, low-level cloud became much more opaque, as the average abundance of INPs at the lifted condensation level was closer to $1 \times 10^{-6}$ $L^{-1}$ (Fig. 5.7b). However, this also reveals that the radiation balance estimated by a model is sensitive to how sea spray particles are generated within that model.

In Hartery et al. (2020a), parameterizations describing the flux of SSPs from breaking waves were compared. The abundance of SSPs calculated from Lagrangian particle back-trajectories demonstrated that G03 leads to systematic over-estimates of this quantity. On average, the abundance of SSPs predicted by the Gong (2003) equation was 1.8$\times$ larger than the measured value. However, this only partially explains the differences in the radiative properties of low-level, mixed-phase cloud observed in Fig. 5.8b. In Fig. 5.3a, G03 predicted many more supermicron particles than the observations suggest. As these particles have substantially more surface area, they are much more efficient ice nuclei. The lack of such droplets within the spectra presented suggests that these drops may not be efficiently transferred up to the altitude of the sampling conduit on the Marine Environment and Ecosystem Voyage ($\sim$20 m). We note that calculations of particle losses presented in Chapter 2 indicated that the sampling conduit successfully transferred ambient particulate to the particle counting instrumentation. Transfer efficiencies exceeded 50%, and were on average 90%, for all particles between 0.003–9 $\mu$m in diameter. As such, our observations are representative of particles in the supermicron size range, and thus their absence is not related to sampling biases. This result is supported by more recent laboratory studies, which have found that the formation of supermicron droplets is significantly less than suggested by Gong (2003) (Prather et al., 2013). Overall, the abundance of supermicron particles within the G03 parameterization leads to an eight-fold increase in the number of ice nucleation sites for a given concentration of SSPs. Combined with the two-fold over-prediction of particle concentrations, this leads to the near twenty-fold bias in predicting the number of INPs (Fig. 5.8a) and the considerable differences in predicted shortwave reflectivity of Southern Ocean cloud (Fig. 5.8b). This result is supported by recent modelling studies, too: when calculating the number of INPs within the Community Aerosol Model, McCluskey et al. (2019) observed model-observation discrepancies of up to 10$\times$ for 69% of the measurements from the CAPRICORN campaign in the Southern Ocean, and for 93% of measurements at Mace Head, Ireland. Within CAM5, the flux of SSPs is modelled via the schemes of Mårtensson

et al. (2003) and Monahan et al. (1986), with the latter being the original study which G03 is based on. Note that CAM5 does add an additional sea surface temperature dependent term to its calculation of SSP flux (Liu et al., 2016). Thus, even though estimates of the number of SSPs from G03 may improve when using a sea-surface temperature dependent term, it will not account for the over-prediction of aerosol surface area, which more strongly governs the availability of ice nucleation sites.

Finally, a simple climate sensitivity analysis was presented. In this analysis, variations to the shortwave reflectivity of low-level mixed-phase cloud were measured for small perturbations to sea surface temperature and surface wind speeds. Despite differences between G03 and H20, a 1 m $s^{-1}$ increase in wind speed produced a similar decrease in shortwave reflectivity in both models. However, what's more striking is that an increase to sea surface temperatures with J11 produces a similar decrease to the shortwave reflectivity. Sea spray parameterizations with a temperature-dependent term are gaining use in models as they reduce known latitudinal biases in the estimation of sea spray particle abundance. However, this implies that as the sea surface continues to warm over the next century, the flux of SSPs will grow, providing more INPs to low-level mixed-phase cloud. Subsequently, these low-level clouds will become less opaque to incoming shortwave radiation, allowing sea surface temperatures to warm further, creating a feedback loop. However, the extent to which sea surface temperature moderates or enhances sea spray flux is still a source of debate, as laboratory studies continue to disagree on the magnitude and even direction of alterations to the flux of SSPs (Mårtensson et al., 2003; Sellegri et al., 2006; Zábori et al., 2012b). Field observations disagree, too: recent observations from the North Atlantic Aerosol and Marine Ecosystems Study find that it is not the number flux of particles which depends on the sea surface temperature, but the average size of the particles generated (Saliba et al., 2019). In Hartery et al. (2020a), it was proposed that variations in wave characteristics offer a valid, alternative explanation for latitudinal variations in the magnitude of sea spray fluxes. The database of whitecap observations presented in the study confirmed that the presence of swell inhibited wave-breaking. Thus, if it were only wave characteristics which governed the magnitude of sea spray flux, then this radiative feedback loop could be broken. However, it does not rule out that sea surface temperature may still alter the flux of sea spray particles. It simply suggests that more robust observations which accurately account for upwind variations in both sea surface temperature and wave-field characteristics are needed to generate precise parameterizations.

However, even if wind speed and wave-field characteristics completely constrained the variability in the flux of sea spray particles, sea surface temperature is still likely to influence the availability of ice-nucleating material at the ocean surface. While the amount of sea spray surface area was successful at characterizing the average number of INPs that were observed (Fig. 5.3b), there was still an order of magnitude of variability around the main trend. These variations could be related to variations in the source areas of the sea spray particles, as the surface availability of biological material is highly spatially and temporally heterogeneous. As temperature is related to biological activity, it is therefore likely that increases to the surface temperature of the Southern Ocean will increase the density of nucleation sites within sea spray particles. However, even this simple relationship may be complicated: variations in the availability of nutrients can have large effects on the biological activity at the ocean surface (Harvey, 2007) and the resulting concentrations of INPs (Irish et al., 2019).

Still, the feedback loop relating increases to wind speed to decreases in cloud opacity is

real and its magnitude is insensitive to the parameterization of sea spray flux used. As the Amundsen Sea Low strengthens over the coming decades (Coggins and McDonald, 2015; Raphael et al., 2016), wind speeds and sea spray flux will increase too. However, the increases to wind speed alone will result in substantially smaller changes to the shortwave radiation balance than if they are also compounded by changes to sea surface temperature.

Ultimately, the increased shortwave reflectivity in low-level mixed-phase clouds partially explains the large and well-known model–measurement biases in the radiation balance over the Southern Ocean. Though the improvements calculated herein were compared to the results of Kay et al. (2016), which is based on the Community Earth System Model, estimations of the shortwave radiation bias within the Unified Model show that the magnitude of the bias may only be as large as 25 W $m^{-2}$ over the Southern Ocean (Schuddeboom et al., 2019). As Schuddeboom et al. (2019) found, tuning model parameters related to the secondary formation of ice can result in improvements to this bias over the Southern Ocean, but often at the expense of other regions. Secondary formation of ice, sometimes referred to as riming or contact freezing, occurs when primary ice collides with super-cooled liquid drops. This process can rapidly scavenge super-cooled liquid droplets within the cloud, which drastically alters its shortwave reflectivity. While tuning secondary ice formation processes produced mixed results over the globe (Schuddeboom et al., 2019), tying primary ice nucleation to the physicochemical properties of the local particulate is likely to result in very targeted alterations to the radiation budget of the Southern Ocean as it is one of few global regions unaffected by dust particles. Despite this, these results are only suggestive. Throughout this analysis a model result from Vergara-Temprado et al. (2018) was assumed to be applicable to climatologies of sea spray particles generated from many under-lying assumptions. Thus, the exact magnitude of these changes could vary considerably. Still, the parameterization presented in Eq. (5.18), being based entirely on in situ observations, is a valuable starting point for climate model research. We re-emphasize that while the results presented in this work are thought-provoking, Eq. (5.18) was only tested against the parameterization in the Unified model by proxy. As such, a proper implementation of Eq. (5.18) into the Unified Model is necessary in order to completely validate its fitness for describing primary ice nucleation.

# 6. Conclusions

In this study, controlling factors for the number of ice nuclei available to Southern Ocean cloud were discussed. Overall, the number of ice-nucleating particles (INPs) observed in the Southern Ocean boundary layer could be accurately modeled based on the suspended surface area of sea spray particles (SSPs). This supports the hypothesis that wind-swept organic detritus is the primary ice nucleation agents in the region. Then, estimates for changes to the shortwave reflectivity of low-level mixed-phase cloud over the Southern Ocean were calculated using a recent model sensitivity result. Given the number of assumptions made throughout this work, the magnitude of these changes are potential upper bounds rather than expected outcomes. However, the results show that the amount of primary ice nucleated within the Unified Model is likely several orders of magnitude larger than the mass that would be nucleated from the available ice nucleation sites. Overall, correctly estimating the number of INPs resulted in noticeable reductions to regional shortwave radiation biases.

This framework was also exploited to test the sensitivity of low-level cloud to small changes in climate. Models that include a temperature-dependent term in their prediction of sea spray particle flux risk introducing a radiative feedback loop over the Southern Ocean that would accelerate warming. Further research needs to account for the effects of

wave characteristics and sea surface temperature on the flux of SSPs as well as the effects of sea surface temperature and nutrient availibility on the density of nucleation sites within SSPs to better understand whether or not such a feedback is realistic. In the interim, offline corrections for the flux of SSPs based solely on latitude would be a reasonable means of managing short-term and long-term accuracy in global climate models. Finally, in situ observations within the Southern Ocean boundary layer were condensed into a relatively compact parameterization for the amount of primary ice nucleated within cloud. This will hopefully be useful to climate models with a single-moment model of cloud phase.

# Conclusions & Implications

This thesis explored indirect connections between natural fluxes of particles from the Southern Ocean and the balance of incoming and outgoing shortwave radiation. Global climate models (GCMs) currently predict that a significant surplus of shortwave radiation enters the Earth system relative to satellite observations over the Southern Ocean (Trenberth and Fasullo, 2010). These biases result from errors in how GCMs predict cloud abundance, opacity, and phase (Bodas-Salcedo et al., 2016). Thus, in-situ measurements collected onboard the R/V *Tangaroa* provide a rare glimpse into the dynamic boundary layer below Southern Ocean cloud. As particles within this layer can act as nucleation points within nascent clouds, the detailed particle size spectra collected over the course of the Marine Environment & Ecosystem Voyage provide invaluable measurements of indirect effects on low-level clouds. Hence, the goals of this thesis were to provide more accurate parameterizations for the production of such particles within GCMs and to characterize how variations in their abundance and physicochemical characteristics could indirectly influence the opacity of Southern Ocean cloud.

This assessment began with a source–receptor analysis in Chapter 3, which was published in the *Journal of Geophysical Research: Atmospheres* (Hartery et al., 2020a). In this study, a Lagrangian particle dispersion model was used to directly connect the abundance of sea spray particles (SSPs) measured on the R/V Tangaroa to the ocean surface that generated them. This created a robust framework in which parameterizations for the flux of particles generated by breaking waves could be validated against in-situ measurements. This framework was also used to optimize parameters within an existing model of the surface flux of SSPs. This model used the wind speed over the ocean as the sole predictor variable. The improved model established that the real flux of SSPs generated by the Southern Ocean is smaller than currently predicted by GCMs at all wind speeds. Further, GCMs predict that the flux of particles from the Southern Ocean scales logarithmically with the near-surface wind speed; however, the improved parameterization demonstrated that below 4 m $s^{-1}$, particles are not being generated at all, consistent with other field observations (Schwendeman and Thomson, 2015). Further, the parameterization predicted that the flux of particles tapers off to a constant value above 30 m $s^{-1}$. This is consistent with observations of the near-surface wind stress in high-intensity cyclones (Huang and Jaeglé, 2017), which found that after a critical wind speed is reached, the amount of momentum transferred from the boundary layer to the Southern Ocean decreases with increasing wind speed. As the transfer of momentum from the boundary layer to the sea surface is the fundamental physical mechanism for generating waves, it is reasonable to expect that the number of particles generated by those waves must also attenuate.

The source–receptor analysis also provided a framework to assess how other environmental variables affect the flux of SSPs. The results indicated that the dependence of SSP fluxes on sea surface temperature was weak in the temperature range of the in-situ observations ($T_w < 12$ °C) and that it did not constrain additional variability within the data set. In that chapter, a database of previously published whitecap observations was also compiled.

The database demonstrated that the percentage of the ocean surface covered in whitecaps is nearly independent of sea surface temperature. This result conflicts with a recent parameterization proposed by Jaeglé et al. (2011), which found that the surface flux of SSPs is highly sensitive to changes in sea surface temperature. The dependence of this parameterization on sea surface temperature helps reconcile the strong latitudinal variations in the abundance of SSPs across the globe (Jaeglé et al., 2011). However, sea spray flux may also be strongly influenced by variations in wave characteristics. In summer, swell persists over the ice-free Southern Ocean; whereas, in the tropics, the ever-changing winds prevent any significant swell from propagating (Jiang and Chen, 2013). The presence of swell does significantly inhibit the frequency of wave-breaking in the open ocean (Sugihara et al., 2007). This could explain why the flux of SSPs from the Southern Ocean is smaller than from the tropics for the same wind speed. It does not rule out, however, that temperature also influences the flux of particles. Instead, it suggests that a more detailed global analysis is required to decouple these two effects, as temperature-dependent parameterizations for the flux of SSPs derived in the absence of a proper control for upwind wave characteristics may generate parameterizations that are overly sensitive to sea surface temperature. As the ranges of swell and sea surface temperature encountered during the voyage were relatively narrow, the in-situ measurements collected on the R/V *Tangaroa* were not well-posed to determine the relative contribution of either effect. However, the data generated (Hartery et al., 2020c) will be invaluable to future research on this topic as they constrain fluxes of particulate at the extremes of wind speed, wave height and sea surface temperature.

However, SSPs within the Southern Ocean boundary layer won't significantly alter the balance of shortwave radiation. Viewed from space, the Southern Ocean is frequently obscured by cloud, and as a result, the scattering of light by these particles is only minor relative to the cloud above. As aircraft observations from the SOCRATES campaign demonstrated in Chapter 3, SSPs are thoroughly scavenged by low-level cloud, leaving few such particles in the free troposphere to scatter incoming solar radiation. Hence, these particles can only influence the balance of incoming shortwave radiation indirectly, by modifying the optical characteristics of low-level Southern Ocean cloud.

In Chapter 4, in-situ and remote-sensing observations made aboard the R/V *Tangaroa* were used to understand the conditions in which boundary layer particles would be available to low-level cloud over the Southern Ocean. A simple correlation analysis between two measures of suspended particle surface area showed that the boundary layer was often well-mixed between the ocean surface and cloud base height. Hence, the particles observed near sea-level are highly relevant to the ubiquitous low-level cloud in the region. In the remaining number of cases when the boundary layer was not well-mixed, the near-surface atmosphere was neutrally-stable and the wind over the ocean was calm. An analysis of AMPS forecasts over the broader Southern Ocean showed that conditions for a well-mixed below-cloud layer, or the formation of fog, are satisfied 80% of the time, consistent with statistics from our time series analysis.

These first chapters successfully characterized both the abundance and availability of particles to Southern Ocean cloud. Thus, in the final chapter, this thesis attempted to estimate the sensitivity of Southern Ocean cloud to changes in the microphysical parameterizations within GCMs. First, it was observed that the abundance of ice-nucleating particles (INPs) measured in the Southern Ocean boundary layer closely matched a parameterization based on the abundance of sea spray particle surface area (McCluskey et al., 2018). The goodness of fit between our observations and this parameterization supports the hypothesis that

**Figure 6.1 :** March, 2018 – Ross Sea. A small wave laps up against a large iceberg, both shrouded by marine stratocumulus. This photo was featured on the cover of the *Journal of Geophysical Research: Atmospheres* Volume 125, Issue 6.

wind-swept organic detritus from the ocean surface, which is internally-mixed with sea spray, is the primary ice nucleation agent in the region (DeMott et al., 2016). To estimate the effect this might have on the phase and radiative properties of low-level clouds, we generated simple climatologies of sea spray and dust particles. These climatologies agreed with our in situ measurements, indicating that dust particles are rarely present in the Southern Ocean boundary layer. We then combined this parameterization with observations from the Southern Ocean Cloud Experiment (Boers et al., 1998) to develop a simple model for the amount of primary ice nucleated within cloud, based on the number of sea spray and dust particles in the boundary layer. The climatologies of sea spray and dust particles demonstrated that the amount of ice generated by this new parameterization is orders of magnitude smaller than the fixed amount of ice nucleated within GCM clouds. A recent model sensitivity analysis (Vergara-Temprado et al., 2018) was leveraged to show that correcting this bias would result in substantial improvements to the shortwave reflectivity of low-level clouds over the wider Southern Ocean region. Though the climatologies resulted from many underlying assumptions that may not always hold, they were thus useful in demonstrating the relevance of primary ice nucleation to the regional radiation balance, motivating the integration of more realistic parameterizations within GCMs.

Finally, the climatologies generated within this last chapter were exploited to test the sensitivity of low-level cloud to small changes in climate. The results showed that including a temperature-dependent term in the prediction of sea spray particle flux introduces a radiative feedback loop over the Southern Ocean that accelerates warming. This is a counterpoint to the established hypothesis that SSPs are climate moderators (Korhonen et al., 2010). A proper quantification of the magnitude and direction of this feedback loop is contingent not only on developing globally-accurate parameterizations of SSPs, but accurate predictions for

the relative abundance of biological material within the sea-surface micro-layer. Thus, despite having a relatively weak influence on cloud reflectivity in warmer regions (Quinn et al., 2017), SSPs may have a large climatic influence near Antarctica. Again, as the climatologies presented in the final chapter were based on many assumptions, a proper quantification of the effect this new parameterization has on the regional radiation balance would require it to be tested within a GCM. Still, the magnitude of the effects observed in Chapter 5 indicates that the primary nucleation of ice within clouds and the production of sea spray particles constitutes a substantial radiative feedback mechanism within the Earth System. The parameterizations described in Chapter 3 and Chapter 5 should be useful starting points in this respect.

# Further Work

While this thesis was primarily dedicated to the abundance and indirect radiative effects of sea spray particles (SSPs), they are certainly not the only relevant atmospheric constituent measured during the Marine Environment & Ecosystem voyage. In terms of abundance, particles in the accumulation mode tended to make up the majority of cloud condensation nuclei. Thus, the number of cloud droplets within low-level Southern Ocean cloud is more strongly determined by the processes which generate these particles. However, the formation of accumulation and Aitken mode particles is much more complicated than for SSPs, as it depends on the abundance of trace, volatile gasses within the atmosphere. Some of the knowledge presented in this thesis is still illuminating in this regard. For instance, in Chapter 3 a parameterization for the surface coverage of whitecaps was constrained to a global database of whitecap observations. This could inform how GCMs describe the flux of precursor gasses from the air–sea interface, as gas exchange is enhanced by the formation of whitecaps (Bell et al., 2017). A study which characterizes the extent to which this parameterization enhances gas exchange, and ultimately particle abundance could be enlightening.

In terms of direct measurement, future voyages to the Southern Ocean could measure fluxes of gasses, like dimethyl sulfide (DMS), across the air–sea interface. In 2012, the Surface Ocean Aerosol Production campaign measured fluxes of DMS from pelagic waters near New Zealand. However, the wave characteristics and the surface temperature of the Southern Ocean are unique. Hence, the exchange of gasses across the air–sea interface could be substantially altered in this environment. Further, sulfate particles are not formed directly from DMS; rather, they are produced from the oxidized by-products of it. Future studies in the region should thus endeavour to measure more gasses in the atmosphere, such as both methanesulfonic acid (MSA), a well-known particle precursor gas. High-quality measurements which can characterize the connections between the seawater abundance of DMS (and its precursor dimethylsulfoniopropionate) and the atmospheric abundance of MSA would add substantial value to the chemistry schemes within GCMs.

Of course, even if a model can generate the necessary particle precursor gasses, it must also accurately predict the nucleation of new particles from them. In this respect, pertinent data collected during the Marine Environment & Ecosystem Voyage was not explored throughout this thesis. On February 11$^{th}$, 2018, while leaving the continental shelf, a boundary layer nucleation event was observed. However, one case study, alone, could not provide sufficient evidence to warrant any substantial changes to parameterizations within GCMs. Hence, this thesis focussed more heavily on the abundance of SSPs, as measurements of their abundance were nearly continuous throughout the voyage. Still, nucleation events within the boundary layer are rare: the abundant particle surface area provided by SSPs in this layer acts as a sink for any volatile gasses, inhibiting nucleation. Hence, the phenomenon is typically restricted to the free troposphere. This case study could provide a unique glimpse into the mechanism of particle formation. As a colleague was measuring concentrations of DMS dissolved in surface waters throughout the voyage, a time-series analysis could determine whether or not there were substantial spikes in the concentration of dissolved DMS which

**Figure 7.1 :** March 2017 – Campbell Plateau. The sun sets over the Southern Ocean.

pre-empted the boundary layer nucleation event.

As much more knowledge can be extracted from the measurements presented in Chapter 2, they are thus extremely valuable to the wider scientific community, as the Southern Ocean is a data-sparse region. Thus, in the short-term, efforts will be focused on publishing a paper which describes the full suite of atmospheric observations made over the course of the Marine Environment and Ecosystem Voyage: measurements of particulate, measurements from meteorological sensors, remote-sensing observations, radiosonde observations, trace gas observations, etc. As of this writing, a manuscript led by Dr Stefanie Kremser has been submitted to the journal, *Earth System Science Data*, based in part on the material presented in Chapter 2. Data presented in this thesis, as well as many other oceanic and atmospheric measurements, are available at: `https://zenodo.org/record/4060237#.X_R40NhKiMo`.

This thesis concluded several times that more comprehensive measurements which constrain the effects of sea surface temperature and wave characteristics are needed to accurately parameterize sea spray flux. This could, in practice, be accomplished by improved in-situ observational efforts. However, one could also study these effects in the laboratory with wave tank experiments. This would allow researchers to fully decouple the many environmental factors which enhance or inhibit the flux of sea spray. However, as was identified near the end of Chapter 5, the extent to which sea spray particles modulate cloud phase is strongly determined by the abundance of biological material entrained into the droplets. Hence, while the parameterization of McCluskey et al. (2018) fit the data from the Marine Environment and Ecosystem Voyage well, to what extent will this be true in future climates? If surface biological material were to become more abundant, then even if sea spray flux remained unchanged, the resulting particles would become much more efficient ice-nucleating particles. As sea surface biological material is highly spatio-temporally heterogeneous, this could explain the remaining variability in the efficiency of sea spray

particles observed in Chapter 5. Understanding how to reasonably constrain that variability within GCMs presents a substantial challenge. Both laboratory and field measurements could be highly illuminating in this regard. For instance, future voyages should endeavour to make more observations of the number of ice-nucleating particles. A source-receptor analysis, like the one used throughout this thesis, would form a framework through which paramaterizations could then be developed. As only four samples were processed over the entire voyage, it is unlikely that the observations presented in this thesis could provide such a robust parameterization; however, they might still unveil the main environmental drivers which vary the ice-nucleating efficiency of sea spray particles. Thus, a brief study could attempt to identify the environmental factors which led to the observed variability in nucleation site density. Future laboratory studies could also allow for a more detailed analysis as to how efficiently surface biological material is entrained into sea spray. Does the thickness of the sea-surface micro-layer enhance the ice-nucleating efficiency of particles? Can only certain types of material be entrained into particulate? Are certain species of phytoplankton more, or less, efficient? This type of detail is likely only resolvable within a laboratory study.

Finally, Chapter 5 offered substantial insight into how GCMs should parameterize the primary nucleation of ice. The new parameterization developed within the chapter will undoubtedly be useful to climate models, as it depends on variables that are available within most climate models which simulate aerosol: the number density of sea spray and dust particles, as well as the temperature and pressure of the cloud level. While the effects observed within Chapter 5 were thought-provoking, the many assumptions underlying the calculations meant that the conclusions drawn about the improvement to the Southern Ocean shortwave radiation bias may be premature. Thus, a proper assessment within a global climate model is necessary in order to realistically characterize the effect of SSPs on the regional and global radiation balance.

Thus, a thorough understanding of how particles interact with clouds could take many more decades. While this thesis hopefully answered many questions, it only raised more. Ultimately, however, it would be foolish to miss the vast forest of knowledge contained within global climate models for these singular trees: each new study only adds more certainty to our climate future. How we sustainably mitigate undesirable changes to our climate is not just a matter of further investment in science, but continued public engagement and prudent policy-making.

# Appendices

## A1. Co-Authored Publications

1. I contributed analysis of ERA-Interim wind-speeds and MODIS Aqua/Terra aerosol optical depth (AOD) relationships over the Southern Ocean (Fig. 4) in the following:

   L. E. Revell, S. Kremser, S. Hartery, M. Harvey, J. P. Mulcahy, J. Williams, O. Morgenstern, A. J. McDonald, V. Varma, L. Bird, and A. Schuddeboom: "The sensitivity of Southern Ocean aerosols and cloud microphysics to sea spray and sulfate aerosol production in the HadGEM3-GA7.1 chemistry–climate model", *Atmospheric Chemistry and Physics*, **19** (24), 2019

2. I helped run the radiosonde program on the R/V *Tangaroa* during the 2018 Marine Environment and Ecosystem Voyage, results of which are presented within:

   P. Kuma, A. J. McDonald, O. Morgenstern, S. P. Alexander, J. J. Cassano, S. Garrett, J. Halla, S. Hartery, M. J. Harvey, S. Parsons, G. Plank, V. Varma, and J. Williams: "Evaluation of Southern Ocean cloud in the HadGEM3 general circulation model and MERRA-2 reanalysis using ship-based observations", *Atmospheric Chemistry and Physics*, **20** (11), 2020

3. A manuscript detailing all atmospherically-relevant data collected over the course of the Marine Environment and Ecosystem Voyage, based in part on information in Chapter 2, has been submitted to the journal Earth System Science Data:

   S. Kremser, M. Harvey, P. Kuma, S. Hartery, A. Saint-Macary, J. McGregor, A. Schuddeboom, M. von Hobe, S. T. Lennartz, A. Geddes, R. Querel, A. McDonald, M. Peltola, K. Sellegri, I. Silber, C. S. Law, C. J. Flynn, A. Marriner, T. C. J. Hill, P. Demott, C. C. Hume, G. Plank, G. Graham, and S. Parsons: "Southern Ocean Cloud and Aerosol data: a compilation of measurements from the 2018 Southern Ocean Ross Sea Marine Ecosystems and Environment voyage", *Earth System Science Data* (submitted), 2020

## A2. Data Availability

1. Estimations of the number of sea spray particles, 10-m wind speeds, and geospatial data related to Chapter 3 have been archived with PANGAEA:

   S. Hartery, M. Harvey, P. Kuma, and A. McDonald: *Number Concentrations of Sea Spray Particles in the Ross Sea (February - March, 2018)*, PANGAEA: `https://doi.pangaea.de/10.1594/PANGAEA.909249`, 2020c

2. All further data pertaining to this thesis is publicly available via Zenodo: `https://zenodo.org/record/4060237#.X_R40NhKiMo`.

# A3. Properties of Size Distributions

**Lognormal Distribution**

The size distribution of sub-micron particles is well-described by the sum of 3–4 lognormal size distributions. The normalized log-normal distribution, $n$, is defined by two parameters: $\sigma$, which describes the width of the distribution and $x_m$, the mode diameter.

$$\frac{dn}{d\log(x)} = \frac{1}{\sqrt{2\pi}\log(\sigma)} e^{-\frac{(\log(x)-\log(x_m))^2}{2\log^2(\sigma)}} \tag{1}$$

The raw moments of the log-normal distribution are given by the following (J. Aitchison, 1957):

$$m_i = \int_{-\infty}^{\infty} x^i \frac{dn}{d\log(x)} d\log x = {x_m}^i e^{\frac{i^2\log^2(\sigma)}{2}} \tag{2}$$

The total number of particles, the mode particle diameter and width of a certain particle mode (e.g. Aitken, accumulation, sea spray) are $N$, $d_p$, and $\sigma$, respectively. Thus, the total suspended surface area (A), mass (M) and volume per particle ($\nu$) are:

$$\begin{aligned} A =& 4\pi N m_2 = 4\pi N \left(\frac{d_p}{2}\right)^2 e^{2\log^2(\sigma)} \\ M =& \frac{4}{3}\pi\rho N m_3 = \frac{4}{3}\pi\rho N \left(\frac{d_p}{2}\right)^3 e^{\frac{9\log^2(\sigma)}{2}} \\ \nu =& \frac{4}{3}\pi \left(\frac{d_p}{2}\right)^3 e^{\frac{9\log^2(\sigma)}{2}} \end{aligned} \tag{3}$$

**Modified Gamma Distribution**

In contrast, cloud droplet and rain size distributions are better represented by a modified gamma distribution. The modified gamma distribution, $n$, is defined by the parameters $\xi$, $\mu$, $\Lambda$, and $\gamma$:

$$\frac{dn}{dx} = \xi x^\mu e^{-\Lambda x^\gamma} \tag{4}$$

Its moments are given by the following (Petty and Huang, 2011):

$$m_i = \int_0^\infty x^i \frac{dn}{dx} dx = \frac{\xi}{\gamma} \frac{\Gamma\left(\frac{\mu+i+1}{\gamma}\right)}{\Lambda^{\frac{\mu+i+1}{\gamma}}} \tag{5}$$

where $\Gamma(x)$ is the gamma function, an analytic continuation of the factorial function across the real numbers. The median diameter is also defined by the following relation (Petty and Huang, 2011):

$$x_m = \left(\frac{\mu}{\Lambda\gamma}\right)^{1/\gamma} \tag{6}$$

Thus, for a droplet size distribution, the volume per particle is:

$$\begin{aligned} \nu =& \frac{4}{3}\pi\Lambda^{-3/\gamma} \frac{\Gamma\left(\frac{\mu+4}{\gamma}\right)}{\Gamma\left(\frac{\mu+1}{\gamma}\right)} \\ =& \frac{4}{3}\pi {d_{d,m}}^3 \left(\frac{\gamma}{\mu}\right)^{3/\gamma} \frac{\Gamma\left(\frac{\mu+4}{\gamma}\right)}{\Gamma\left(\frac{\mu+1}{\gamma}\right)} \end{aligned} \tag{7}$$

where $d_{d,m}$ is the median droplet diameter.

# References


Akaike, H.: "A new look at the statistical model identification", *IEEE Transactions on Automatic Control*, **19** (6), 1974.

Albert, M. F. M. A., M. D. Anguelova, A. M. M. Manders, M. Schaap, and G. de Leeuw: "Parameterization of oceanic whitecap fraction based on satellite observations", *Atmospheric Chemistry and Physics*, **16** (21), 2016.

Albrecht, B.: "Aerosols, Cloud Microphysics, and Fractional Cloudiness", *Science*, **245** (4923), 1989.

Andreae, M. and W. Barnard: "The marine chemistry of dimethylsulfide", *Marine Chemistry*, **14** (3), 1984.

Andreas, E. L., L. Mahrt, and D. Vickers: "An improved bulk air–sea surface flux algorithm, including spray-mediated transfer", *Quarterly Journal of the Royal Meteorological Society*, **141** (687), 2015.

Ayash, T., S. Gong, and C. Q. Jia: "Direct and Indirect Shortwave Radiative Effects of Sea Salt Aerosols", *Journal of Climate*, **21** (13), 2008.

Bao, J.-W., C. W. Fairall, S. A. Michelson, and L. Bianco: "Parameterizations of Sea-Spray Impact on the Air–Sea Momentum and Heat Fluxes", *Monthly Weather Review*, **139** (12), 2011.

Baron, P. A. and K. Willeke: *Aerosol Measurement: Principles, Techniques, and Applications*, John Wiley and Sons, Inc., 2001.

Bates, T. S., B. J. Huebert, J. L. Gras, F. B. Griffiths, and P. A. Durkee: "International Global Atmospheric Chemistry (IGAC) project's first aerosol characterization experiment (ACE 1): Overview", *Journal of Geophysical Research: Atmospheres*, **103** (D13), 1998.

Bell, T., S. Landwehr, S. D. Miller, W. J. de Bruyn, A. H. Callaghan, B. Scanlon, B. Ward, M. Yang, and E. S. Saltzman: "Estimation of bubble-mediated air–sea gas exchange from concurrent DMS and $CO_2$ transfer velocities at intermediate–high wind speeds", *Atmospheric Chemistry and Physics*, **17** (14), 2017.

Bigg, E. K. and S. C. Hopwood: "Ice Nuclei in the Antarctic", *Journal of the Atmospheric Sciences*, **20** (3), 1963.

Bigg, E.: "Ice nucleus concentrations in remote areas", *Journal of the Atmospheric Sciences*, **30** (6), 1973.

Bodas-Salcedo, A., P. G. Hill, K. Furtado, K. D. Williams, P. R. Field, J. C. Manners, P. Hyder, and S. Kato: "Large Contribution of Supercooled Liquid Clouds to the Solar Radiation Budget of the Southern Ocean", *Journal of Climate*, **29** (11), 2016.

Bodas-Salcedo, A., K. D. Williams, M. A. Ringer, I. Beau, J. N. Cole, J.-L. Dufresne, T. Koshiro, B. Stevens, Z. Wang, and T. Yokohata: "Origins of the solar radiation biases over the Southern Ocean in CFMIP2 models", *Journal of Climate*, **27** (1), 2014.

Boers, R., J. Jensen, and P. Krummel: "Microphysical and short-wave radiative structure of stratocumulus clouds over the Southern Ocean: Summer results and seasonal differences", *Quarterly Journal of the Royal Meteorological Society*, **124** (545), 1998.

Bohren, C. F. and D. R. Huffman: "Absorption and scattering by a sphere", *Absorption and scattering of light by small particles*, 1983.

Borys, R. D., D. H. Lowenthal, S. A. Cohn, and W. O. J. Brown: "Mountaintop and radar measurements of anthropogenic aerosol effects on snow growth and snowfall rate", *Geophysical Research Letters*, **30** (10), 2003.

Brioude, J., D. Arnold, A. Stohl, M. Cassiani, D. Morton, P. Seibert, W. Angevine, S. Evan, A. Dingwell, J. D. Fast, R. C. Easter, I. Pisso, J. Burkhart, and G. Wotawa: "The Lagrangian particle dispersion model FLEXPART-WRF version 3.1", *Geoscientific Model Development*, **6** (6), 2013.

Brockman, J.: "Sampling and transport of aerosols", Chap. 8, *Aerosol Measurement: Principles, Techniques, and Applications*, P. A. Baron and K. Willeke, John Wiley and Sons, Inc., 2001.

Bromwich, D. H., A. J. Monaghan, K. W. Manning, and J. G. Powers: "Real-Time Forecasting for the Antarctic: An Evaluation of the Antarctic Mesoscale Prediction System (AMPS)", *Monthly Weather Review*, **133** (3), 2005.

Brumer, S. E., C. J. Zappa, I. M. Brooks, H. Tamura, S. M. Brown, B. W. Blomquist, C. W. Fairall, and A. Cifuentes-Lorenzen: "Whitecap Coverage Dependence on Wind and Wave Statistics as Observed during SO GasEx and HiWinGS", *Journal of Physical Oceanography*, **47** (9), 2017.

Burnham, K. P. and D. R. Anderson: *Model Selection and Multimodel Inference*, Springer-Verlag New York, 2002.

Cadle, R. D., W. H. Fischer, E. R. Frank, and J. P. Lodge: "Particles in the Antarctic Atmosphere", *Journal of the Atmospheric Sciences*, **25** (1), 1968.

Callaghan, A. H., M. D. Stokes, and G. B. Deane: "The effect of water temperature on air entrainment, bubble plumes, and surface foam in a laboratory breaking-wave analog", *Journal of Geophysical Research: Oceans*, **119** (11), 2014.

Callaghan, A., G. de Leeuw, L. Cohen, and C. D. O'Dowd: "Relationship of oceanic whitecap coverage to wind speed and wind history", *Geophysical Research Letters*, **35** (23), 2008.

Callaghan, A. H., G. B. Deane, M. D. Stokes, and B. Ward: "Observed variation in the decay time of oceanic whitecap foam", *Journal of Geophysical Research: Oceans*, **117** (C9), 2012.

Callaghan, A. H. and M. White: "Automated Processing of Sea Surface Images for the Determination of Whitecap Coverage", *Journal of Atmospheric and Oceanic Technology*, **26** (2), 2009.

Carslaw, K. S., L. A. Lee, C. L. Reddington, K. J. Pringle, A. Rap, P. M. Forster, G. W. Mann, D. V. Spracklen, M. T. Woodhouse, L. A. Regayre, and J. R. Pierce: "Large contribution of natural aerosols to uncertainty in indirect forcing", *Nature*, **503**, 2013.

Charlson, R. J., J. E. Lovelock, M. O. Andreae, S. G. Warren, et al.: "Oceanic phytoplankton, atmospheric sulphur, cloud albedo and climate", *Nature*, **326** (6114), 1987.

Coggins, J. H. J. and A. J. McDonald: "The influence of the Amundsen Sea Low on the winds in the Ross Sea and surroundings: Insights from a synoptic climatology", *Journal of Geophysical Research: Atmospheres*, **120** (6), 2015.

Coggins, J. H. J., A. J. McDonald, and B. Jolly: "Synoptic climatology of the Ross Ice Shelf and Ross Sea region of Antarctica: k-means clustering and validation", *International Journal of Climatology*, **34** (7), 2014.

DeMott, P. J., A. J. Prenni, X. Liu, S. M. Kreidenweis, M. D. Petters, C. H. Twohy, M. S. Richardson, T. Eidhammer, and D. C. Rogers: "Predicting global atmospheric ice nuclei distributions and their impacts on climate", *Proceedings of the National Academy of Sciences*, **107** (25), 2010.

DeMott, P. J., T. C. J. Hill, C. S. McCluskey, K. A. Prather, D. B. Collins, R. C. Sullivan, M. J. Ruppel, R. H. Mason, V. E. Irish, T. Lee, C. Y. Hwang, T. S. Rhee, J. R. Snider, G. R. McMeeking, S. Dhaniyala, E. R. Lewis, J. J. B. Wentzell, J. Abbatt, C. Lee, C. M. Sultana, A. P. Ault, J. L. Axson, M. Diaz Martinez, I. Venero, G. Santos-Figueroa, M. D. Stokes, G. B. Deane, O. L. Mayol-Bracero, V. H. Grassian, T. H. Bertram, A. K. Bertram, B. F. Moffett, and G. D. Franc: "Sea spray aerosol as a unique source of ice nucleating particles", *Proceedings of the National Academy of Sciences*, **113** (21), 2016.

Edson, J. B., V. Jampana, R. A. Weller, S. P. Bigorre, A. J. Plueddemann, C. W. Fairall, S. D. Miller, L. Mahrt, D. Vickers, and H. Hersbach: "On the Exchange of Momentum over the Open Ocean", *Journal of Physical Oceanography*, **43** (8), 2013.

Fisher, N. I. and A. J. Lee: "Correlation Coefficients for Random Variables on a Unit Sphere or Hypersphere", *Biometrika*, **73** (1), 1986.

Fong, D. C.-L. and M. Saunders: "LSMR: An Iterative Algorithm for Sparse Least-Squares Problems", *SIAM J. Sci. Comput.*, **33** (5), 2011.

Fossum, K. N., J. Ovadnevaite, D. Ceburnis, M. Dall'Osto, S. Marullo, M. Bellacicco, R. Simó, D. Liu, M. Flynn, A. Zuend, and C. O'Dowd: "Summertime Primary and Secondary Contributions to Southern Ocean Cloud Condensation Nuclei", *Scientific Reports*, **8** (1), 2018.

Furtado, K. and P. Field: "The Role of Ice Microphysics Parametrizations in Determining the Prevalence of Supercooled Liquid Water in High-Resolution Simulations of a Southern Ocean Midlatitude Cyclone", *Journal of the Atmospheric Sciences*, **74** (6), 2017.

Garratt, J.: "Review: the atmospheric boundary layer", *Earth-Science Reviews*, **37** (1), 1994.

Gerber, H. E.: *Relative-humidity parameterization of the Navy Aerosol Model (NAM)*, Naval Research Lab, 1985.

Ginoux, P., M. Chin, I. Tegen, J. M. Prospero, B. Holben, O. Dubovik, and S.-J. Lin: "Sources and distributions of dust aerosols simulated with the GOCART model", *Journal of Geophysical Research: Atmospheres*, **106** (D17), 2001.

Goddijn-Murphy, L., D. K. Woolf, and A. H. Callaghan: "Parameterizations and Algorithms for Oceanic Whitecap Coverage", *Journal of Physical Oceanography*, **41** (4), 2011.

Gong, S. L.: "A parameterization of sea-salt aerosol source function for sub- and super-micron particles", *Global Biogeochemical Cycles*, **17** (4), 2003.

Gras, J. L., S. I. Jimi, S. T. Siems, and P. B. Krummel: "Postfrontal nanoparticles at Cape Grim: observations", *Environmental Chemistry*, **6** (6), 2009.

Grythe, H., N. I. Kristiansen, C. D. Groot Zwaaftink, S. Eckhardt, J. Ström, P. Tunved, R. Krejci, and A. Stohl: "A new aerosol wet removal scheme for the Lagrangian particle model FLEXPART v10", *Geoscientific Model Development*, **10** (4), 2017.

Grythe, H., J. Ström, R. Krejci, P. Quinn, and A. Stohl: "A review of sea-spray aerosol source functions using a large global set of sea salt aerosol concentration measurements", *Atmospheric Chemistry and Physics*, **14** (3), 2014.

Gunn, R.: "The statistical electrification of aerosols by ionic diffusion", *Journal of Colloid Science*, **10** (1), 1955.

Hande, L. B., S. T. Siems, and M. J. Manton: "Observed Trends in Wind Speed over the Southern Ocean", *Geophysical Research Letters*, **39** (11), 2012.

Hande, L. B., S. T. Siems, M. J. Manton, and D. Belusic: "Observations of wind shear over the Southern Ocean", *Journal of Geophysical Research: Atmospheres*, **117** (D12), 2012.

Hara, K., K. Osada, M. Kido, K. Matsunaga, Y. Iwasaka, G. Hashida, and T. Yamanouchi: "Variations of constituents of individual sea-salt particles at Syowa station, Antarctica", *Tellus B*, **57** (3), 2005.

Hartery, S., M. Harvey, P. Kuma, and A. McDonald: *Number Concentrations of Sea Spray Particles in the Ross Sea (February - March, 2018)*, PANGAEA: `https://doi.pangaea.de/10.1594/PANGAEA.909249`, 2020c.

Hartery, S., P. Kuma, M. Harvey, and A. McDonald: "Quantification of Boundary Layer Mixing over the Southern Ocean Using In-Situ and Remotely-Sensed Measurements", *Earth and Space Science Open Archive, a pre-print service for Geophysical Research Letters*, 2020b.

Hartery, S., D. Toohey, L. Revell, K. Sellegri, P. Kuma, M. Harvey, and A. McDonald: "Constraining the Surface Flux of Sea Spray Particles from the Southern Ocean", *Journal of Geophysical Research: Atmospheres*, **125** (4), 2020a.

Harvey, M.: "The iron CLAW", *Environmental Chemistry*, **4** (6), 2007.
Hawcroft, M., J. M. Haywood, M. Collins, A. Jones, A. C. Jones, and G. Stephens: "Southern Ocean albedo, inter-hemispheric energy transports and the double ITCZ: global impacts of biases in a coupled model", *Climate Dynamics*, **48** (7), 2017.
Haynes, J. M., C. Jakob, W. B. Rossow, G. Tselioudis, and J. Brown: "Major Characteristics of Southern Ocean Cloud Regimes and Their Effects on the Energy Budget", *Journal of Climate*, **24** (19), 2011.
Hegg, D. A., D. S. Covert, H. H. Jonsson, and R. Woods: "Differentiating natural and anthropogenic cloud condensation nuclei in the California coastal zone", *Tellus B: Chemical and Physical Meteorology*, **61** (4), 2009.
Henzing, J. S., D. J. L. Olivié, and P. F. J. van Velthoven: "A parameterization of size resolved below cloud scavenging of aerosols by rain", *Atmospheric Chemistry and Physics*, **6** (11), 2006.
Herbert, R. J., B. J. Murray, T. F. Whale, S. J. Dobbie, and J. D. Atkinson: "Representing time-dependent freezing behaviour in immersion mode ice nucleation", *Atmospheric Chemistry and Physics*, **14** (16), 2014.
Hermann, M., B. Wehner, O. Bischof, H.-S. Han, T. Krinke, W. Liu, A. Zerrath, and A. Wiedensohler: "Particle counting efficiencies of new TSI condensation particle counters", *Journal of Aerosol Science*, **38** (6), 2007.
Hertel, O., J. Christensen, E. H. Runge, W. A. Asman, R. Berkowicz, M. F. Hovmand, and Ø. Hov: "Development and testing of a new variable scale air pollution model—ACDEP", *Atmospheric Environment*, **29** (11), 1995.
Hicks, B. B., D. D. Baldocchi, T. P. Meyers, R. P. Hosker, and D. R. Matt: "A preliminary multiple resistance routine for deriving dry deposition velocities from measured quantities", *Water, Air, and Soil Pollution*, **36** (3), 1987.
Hogan, R. J., M. D. Behera, E. J. O'Connor, and A. J. Illingworth: "Estimate of the global distribution of stratiform supercooled liquid water clouds using the LITE lidar", *Geophysical Research Letters*, **31** (5), 2004.
Hoppel, W. A., G. M. Frick, and R. E. Larson: "Effect of nonprecipitating clouds on the aerosol size distribution in the marine boundary layer", *Geophysical Research Letters*, **13** (2), 1986.
Hsu, S. A.: "A Mechanism for the Increase of Wind Stress (Drag) Coefficient with Wind Speed over Water Surfaces: A Parametric Model", *Journal of Physical Oceanography*, **16** (1), 1986.
Hu, Y., S. Rodier, K.-m. Xu, W. Sun, J. Huang, B. Lin, P. Zhai, and D. Josset: "Occurrence, liquid water content, and fraction of supercooled water clouds from combined CALIOP/IIR/MODIS measurements", *Journal of Geophysical Research: Atmospheres*, **115** (D4), 2010.
Huang, J. and L. Jaeglé: "Wintertime enhancements of sea salt aerosol in polar regions consistent with a sea ice source from blowing snow", *Atmospheric Chemistry and Physics*, **17** (5), 2017.
Huang, Y., S. T. Siems, M. J. Manton, A. Protat, and J. Delanoë: "A study on the low-altitude clouds over the Southern Ocean using the DARDAR-MASK", *Journal of Geophysical Research: Atmospheres*, **117** (D18), 2012.
Hwang, P. A.: "High-Wind Drag Coefficient and Whitecap Coverage Derived from Microwave Radiometer Observations in Tropical Cyclones", *Journal of Physical Oceanography*, **48** (10), 2018.
Irish, V. E., S. J. Hanna, Y. Xi, M. Boyer, E. Polishchuk, M. Ahmed, J. Chen, J. P. D. Abbatt, M. Gosselin, R. Chang, L. A. Miller, and A. K. Bertram: "Revisiting properties and con-

centrations of ice-nucleating particles in the sea surface microlayer and bulk seawater in the Canadian Arctic during summer", *Atmospheric Chemistry and Physics*, **19** (11), 2019.
Irving, D., I. Simmonds, and K. Keay: "Mesoscale Cyclone Activity over the Ice-Free Southern Ocean: 1999–2008", *Journal of Climate*, **23** (20), 2010.
Ito, T.: "Study of background aerosols in the Antarctic troposphere", *Journal of atmospheric chemistry*, **3** (1), 1985.
J. Aitchison, J. A. C. B.: *The Lognormal Distribution*, Cambridge University Press, 1957.
Jaeglé, L., P. K. Quinn, T. S. Bates, B. Alexander, and J.-T. Lin: "Global distribution of sea salt aerosols: new constraints from in situ and remote sensing observations", *Atmospheric Chemistry and Physics*, **11** (7), 2011.
Janjic, Z. I.: *Nonsingular implementation of the Mellor-Yamada level 2.5 scheme in the NCEP Meso model*, National Center for Environmental Prediction (NCEP), 2001.
Jeffery, C. and P. Austin: "Homogeneous nucleation of supercooled water: Results from a new equation of state", *Journal of Geophysical Research: Atmospheres*, **102** (D21), 1997.
Jia, N. and D. Zhao: "The Influence of Wind Speed and Sea States on Whitecap Coverage", *Journal of Ocean University of China*, **18** (2), 2019.
Jiang, H. and G. Chen: "A Global View on the Swell and Wind Sea Climate by the Jason-1 Mission: A Revisit", *Journal of Atmospheric and Oceanic Technology*, **30** (8), 2013.
Jolly, B., A. J. McDonald, J. H. J. Coggins, P. Zawar-Reza, J. Cassano, M. Lazzara, G. Graham, G. Plank, O. Petterson, and E. Dale: "A Validation of the Antarctic Mesoscale Prediction System Using Self-Organizing Maps and High-Density Observations from SNOWWEB", *Monthly Weather Review*, **144** (9), 2016.
Jones, C. R., C. S. Bretherton, and D. Leon: "Coupled vs. decoupled boundary layers in VOCALS-REx", *Atmospheric Chemistry and Physics*, **11** (14), 2011.
Kaleschke, L., A. Richter, J. Burrows, O. Afe, G. Heygster, J. Notholt, A. M. Rankin, H. K. Roscoe, J. Hollwedel, T. Wagner, and H.-W. Jacobi: "Frost flowers on sea ice as a source of sea salt and their influence on tropospheric halogen chemistry", *Geophysical Research Letters*, **31** (16), 2004.
Kay, J. E., C. Wall, V. Yettella, B. Medeiros, C. Hannay, P. Caldwell, and C. Bitz: "Global Climate Impacts of Fixing the Southern Ocean Shortwave Radiation Bias in the Community Earth System Model (CESM)", *Journal of Climate*, **29** (12), 2016.
Korhonen, H., K. S. Carslaw, P. M. Forster, S. Mikkonen, N. D. Gordon, and H. Kokkola: "Aerosol climate feedback due to decadal increases in Southern Hemisphere wind speeds", *Geophysical Research Letters*, **37** (2), 2010.
Kremser, S., M. Harvey, P. Kuma, S. Hartery, A. Saint-Macary, J. McGregor, A. Schuddeboom, M. von Hobe, S. T. Lennartz, A. Geddes, R. Querel, A. McDonald, M. Peltola, K. Sellegri, I. Silber, C. S. Law, C. J. Flynn, A. Marriner, T. C. J. Hill, P. Demott, C. C. Hume, G. Plank, G. Graham, and S. Parsons: "Southern Ocean Cloud and Aerosol data: a compilation of measurements from the 2018 Southern Ocean Ross Sea Marine Ecosystems and Environment voyage", *Earth System Science Data* (submitted), 2020.
Kuma, P., A. J. McDonald, O. Morgenstern, S. P. Alexander, J. J. Cassano, S. Garrett, J. Halla, S. Hartery, M. J. Harvey, S. Parsons, G. Plank, V. Varma, and J. Williams: "Evaluation of Southern Ocean cloud in the HadGEM3 general circulation model and MERRA-2 reanalysis using ship-based observations", *Atmospheric Chemistry and Physics*, **20** (11), 2020.
Kyrö, E.-M., T. Grönholm, H. Vuollekoski, A. Virkkula, M. Kulmala, and L. Laakso: "Snow scavenging of ultrafi ne particles: field measurements and parameterization", *Boreal Environment Research*, **14**, 2009.
Lana, A., T. Bell, R. Simó, S. Vallina, J. Ballabrera-Poy, A. Kettle, J. Dachs, L. Bopp, E. Saltzman, J. Stefels, et al.: "An updated climatology of surface dimethlysulfide concentrations and emission fluxes in the global ocean", *Global Biogeochemical Cycles*, **25** (1), 2011.

Lewis, E. and S. Schwartz: *Sea Salt Aerosol Production: Mechanisms, Methods, Measurements and Models – A Critical Review*, American Geophysical Union, 2004.

Liu, X., P.-L. Ma, H. Wang, S. Tilmes, B. Singh, R. C. Easter, S. J. Ghan, and P. J. Rasch: "Description and evaluation of a new four-mode version of the Modal Aerosol Module (MAM4) within version 5.3 of the Community Atmosphere Model", *Geoscientific Model Development*, **9** (2), 2016.

Lock, A. P., A. R. Brown, M. R. Bush, G. M. Martin, and R. N. B. Smith: "A New Boundary Layer Mixing Scheme. Part I: Scheme Description and Single-Column Model Tests", *Monthly Weather Review*, **128** (9), 2000.

Markowski, G. R.: "Improving Twomey's Algorithm for Inversion of Aerosol Measurement Data", *Aerosol Science and Technology*, **7** (2), 1987.

Mårtensson, E., E. Nilsson, G. de Leeuw, L. Cohen, and H.-C. Hansson: "Laboratory simulations and parameterization of the primary marine aerosol production", *Journal of Geophysical Research: Atmospheres*, **108** (D9), 2003.

McCluskey, C. S., P. J. DeMott, P.-L. Ma, and S. M. Burrows: "Numerical Representations of Marine Ice-Nucleating Particles in Remote Marine Environments Evaluated Against Observations", *Geophysical Research Letters*, **46** (13), 2019.

McCluskey, C. S., T. C. J. Hill, R. S. Humphries, A. M. Rauker, S. Moreau, P. G. Strutton, S. D. Chambers, A. G. Williams, I. McRobert, J. Ward, M. D. Keywood, J. Harnwell, W. Ponsonby, Z. M. Loh, P. B. Krummel, A. Protat, S. M. Kreidenweis, and P. J. DeMott: "Observations of Ice Nucleating Particles Over Southern Ocean Waters", *Geophysical Research Letters*, **45** (21), 2018.

McCluskey, C. S., T. C. J. Hill, F. Malfatti, C. M. Sultana, C. Lee, M. V. Santander, C. M. Beall, K. A. Moore, G. C. Cornwell, D. B. Collins, K. A. Prather, T. Jayarathne, E. A. Stone, F. Azam, S. M. Kreidenweis, and P. J. DeMott: "A Dynamic Link between Ice Nucleating Particles Released in Nascent Sea Spray Aerosol and Oceanic Biological Activity during Two Mesocosm Experiments", *Journal of the Atmospheric Sciences*, **74** (1), 2017.

McCoy, D. T., S. M. Burrows, R. Wood, D. P. Grosvenor, S. M. Elliott, P.-L. Ma, P. J. Rasch, and D. L. Hartmann: "Natural aerosols explain seasonal and spatial patterns of Southern Ocean cloud albedo", *Science Advances*, **1** (6), 2015.

McFarquhar, G. M., C. Bretherton, R. Marchand, A. Protat, P. J. DeMott, S. P. Alexander, G. C. Roberts, C. H. Twohy, D. Toohey, S. Siems, Y. Huang, R. Wood, R. M. Rauber, S. Lasher-Trapp, J. Jensen, J. Stith, J. Mace, J. Um, E. Järvinen, M. Schnaiter, A. Gettelman, K. J. Sanchez, C. S. McCluskey, L. M. Russell, I. L. McCoy, R. Atlas, C. G. Bardeen, K. A. Moore, T. C. J. Hill, R. S. Humphries, M. D. Keywood, Z. Ristovski, L. Cravigan, R. Schofield, C. Fairall, M. D. Mallet, S. M. Kreidenweis, B. Rainwater, J. D'Alessandro, Y. Wang, W. Wu, G. Saliba, E. J. T. Levin, S. Ding, F. Lang, S. C. Truong, C. Wolff, J. Haggerty, M. J. Harvey, A. Klekociuk, and A. McDonald: "Observations of clouds, aerosols, precipitation, and surface radiation over the Southern Ocean: An overview of CAPRICORN, MARCUS, MICRE and SOCRATES", *Bulletin of the American Meteorological Society*, 2020.

Modini, R. L., A. A. Frossard, L. Ahlm, L. M. Russell, C. E. Corrigan, G. C. Roberts, L. N. Hawkins, J. C. Schroder, A. K. Bertram, R. Zhao, A. K. Y. Lee, J. P. D. Abbatt, J. Lin, A. Nenes, Z. Wang, A. Wonaschütz, A. Sorooshian, K. J. Noone, H. Jonsson, J. H. Seinfeld, D. Toom-Sauntry, A. M. Macdonald, and W. R. Leaitch: "Primary marine aerosol-cloud interactions off the coast of California", *Journal of Geophysical Research: Atmospheres*, **120** (9), 2015.

Monahan, E. C., D. E. Spiel, and K. L. Davidson: "A Model of Marine Aerosol Generation Via Whitecaps and Wave Disruption", *Oceanic Whitecaps: And Their Role in Air-Sea Exchange Processes*, E. C. Monahan and G. M. Niocaill, Springer, 1986.

Monahan, E. C.: "Oceanic Whitecaps", *Journal of Physical Oceanography*, **1** (2), 1971.
Monahan, E. C. and I. Ó Muircheartaigh: "Optimal Power-Law Description of Oceanic Whitecap Coverage Dependence on Wind Speed", *Journal of Physical Oceanography*, **10** (12), 1980.
Murphy, D., J. Anderson, P. Quinn, L. McInnes, F. Brechtel, S. Kreidenweis, A. Middlebrook, M. Pósfai, D. Thomson, and P. Buseck: "Influence of sea-salt on aerosol radiative properties in the Southern Ocean marine boundary layer", *Nature*, **392**, 1998.
Nam, C., S. Bony, J.-L. Dufresne, and H. Chepfer: "The 'too few, too bright' tropical low-cloud problem in CMIP5 models", *Geophysical Research Letters*, **39** (21), 2012.
Nash, J. and J. Sutcliffe: "River flow forecasting through conceptual models part I — A discussion of principles", *Journal of Hydrology*, **10** (3), 1970.
Niedermeier, D., R. A. Shaw, S. Hartmann, H. Wex, T. Clauss, J. Voigtländer, and F. Stratmann: "Heterogeneous ice nucleation: exploring the transition from stochastic to singular freezing behavior", *Atmospheric Chemistry and Physics*, **11** (16), 2011.
Niemand, M., O. Möhler, B. Vogel, H. Vogel, C. Hoose, P. Connolly, H. Klein, H. Bingemer, P. DeMott, J. Skrotzki, and T. Leisner: "A Particle-Surface-Area-Based Parameterization of Immersion Freezing on Desert Dust Particles", *Journal of the Atmospheric Sciences*, **69** (10), 2012.
Norris, S. J., I. M. Brooks, B. I. Moat, M. J. Yelland, G. de Leeuw, R. W. Pascal, and B. Brooks: "Near-surface measurements of sea spray aerosol production over whitecaps in the open ocean", *Ocean Science*, **9** (1), 2013.
Ortiz-Suslow, D. G., B. K. Haus, S. Mehta, and N. J. M. Laxague: "Sea Spray Generation in Very High Winds", *Journal of the Atmospheric Sciences*, **73** (10), 2016.
Ovadnevaite, J., A. Manders, G. de Leeuw, D. Ceburnis, C. Monahan, A.-I. Partanen, H. Korhonen, and C. D. O'Dowd: "A sea spray aerosol flux parameterization encapsulating wave state", *Atmospheric Chemistry and Physics*, **14** (4), 2014.
Petters, M. D. and S. M. Kreidenweis: "A single parameter representation of hygroscopic growth and cloud condensation nucleus activity", *Atmospheric Chemistry and Physics*, **7** (8), 2007.
Petty, G. W. and W. Huang: "The Modified Gamma Size Distribution Applied to Inhomogeneous and Nonspherical Particles: Key Relationships and Conversions", *Journal of the Atmospheric Sciences*, **68** (7), 2011.
Piazzola, J., P. Forget, and S. Despiau: "A sea spray generation function for fetch-limited conditions", *Annales Geophysicae*, **20** (1), 2002.
Polar Meteorology Group: *Antarctic Mesoscale Prediction System (AMPS) Domain 1 Forecasts*, Byrd Polar Research Center, Ohio State University. Data retrieved from Climate Data Gateway at NCAR: `https://www.earthsystemgrid.org/project/amps.html`, 2018.
Popinet, S., M. Smith, and C. Stevens: "Experimental and Numerical Study of the Turbulence Characteristics of Airflow around a Research Vessel", *Journal of Atmospheric and Oceanic Technology*, **21** (10), 2004.
Pósfai, M., J. Li, J. R. Anderson, and P. R. Buseck: "Aerosol bacteria over the Southern Ocean during ACE-1", *Atmospheric Research*, **66** (4), 2003.
Powell, M. D., P. J. Vickery, and T. A. Reinhold: "Reduced drag coefficient for high wind speeds in tropical cyclones", *Nature*, **422** (6929), 2003.
Powers, J. G., K. W. Manning, D. H. Bromwich, J. J. Cassano, and A. M. Cayette: "A Decade of Antarctic Science Support Through Amps", *Bulletin of the American Meteorological Society*, **93** (11), 2012.
Prather, K. A., T. H. Bertram, V. H. Grassian, G. B. Deane, M. D. Stokes, P. J. DeMott, L. I. Aluwihare, B. P. Palenik, F. Azam, J. H. Seinfeld, R. C. Moffet, M. J. Molina, C. D. Cappa, F. M. Geiger, G. C. Roberts, L. M. Russell, A. P. Ault, J. Baltrusaitis, D. B. Collins, C. E.

Corrigan, L. A. Cuadra-Rodriguez, C. J. Ebben, S. D. Forestieri, T. L. Guasco, S. P. Hersey, M. J. Kim, W. F. Lambert, R. L. Modini, W. Mui, B. E. Pedler, M. J. Ruppel, O. S. Ryder, N. G. Schoepp, R. C. Sullivan, and D. Zhao: "Bringing the ocean into the laboratory to probe the chemical complexity of sea spray aerosol", *Proceedings of the National Academy of Sciences*, **110** (19), 2013.

Pruppacher, H. R., J. D. Klett, and P. K. Wang: *Microphysics of clouds and precipitation*, Taylor & Francis, 1998.

Quinn, P. K., D. J. Coffman, J. E. Johnson, L. M. Upchurch, and T. S. Bates: "Small fraction of marine cloud condensation nuclei made up of sea spray aerosol", *Nature Geoscience*, **10**, 2017.

Raphael, M. N., G. J. Marshall, J. Turner, R. L. Fogt, D. Schneider, D. A. Dixon, J. S. Hosking, J. M. Jones, and W. R. Hobbs: "The Amundsen Sea Low: Variability, Change, and Impact on Antarctic Climate", *Bulletin of the American Meteorological Society*, **97** (1), 2016.

Revell, L. E., S. Kremser, S. Hartery, M. Harvey, J. P. Mulcahy, J. Williams, O. Morgenstern, A. J. McDonald, V. Varma, L. Bird, and A. Schuddeboom: "The sensitivity of Southern Ocean aerosols and cloud microphysics to sea spray and sulfate aerosol production in the HadGEM3-GA7.1 chemistry–climate model", *Atmospheric Chemistry and Physics*, **19** (24), 2019.

Richter, D. H. and P. P. Sullivan: "Sea Surface Drag and the Role of Spray", *Geophysical Research Letters*, **40** (3), 2013.

Romps, D. M.: "Exact Expression for the Lifting Condensation Level", *Journal of the Atmospheric Sciences*, **74** (12), 2017.

Rosenfeld, D. and W. L. Woodley: "Deep convective clouds with sustained supercooled liquid water down to-37.5 degrees C", *Nature*, **405** (6785), 2000.

Russell, L. M., D. H. Lenschow, K. K. Laursen, P. B. Krummel, S. T. Siems, A. R. Bandy, D. C. Thornton, and T. S. Bates: "Bidirectional mixing in an ACE 1 marine boundary layer overlain by a second turbulent layer", *Journal of Geophysical Research: Atmospheres*, **103** (D13), 1998.

Saliba, G., C.-L. Chen, S. Lewis, L. M. Russell, L.-H. Rivellini, A. K. Y. Lee, P. K. Quinn, T. S. Bates, N. Haëntjens, E. S. Boss, L. Karp-Boss, N. Baetge, C. A. Carlson, and M. J. Behrenfeld: "Factors driving the seasonal and hourly variability of sea-spray aerosol number in the North Atlantic", *Proceedings of the National Academy of Sciences*, **116** (41), 2019.

Schluessel, P., W. J. Emery, H. Grassl, and T. Mammen: "On the bulk-skin temperature difference and its impact on satellite remote sensing of sea surface temperature", *Journal of Geophysical Research: Oceans*, **95** (C8), 1990.

Schuddeboom, A., V. Varma, A. J. McDonald, O. Morgenstern, M. Harvey, S. Parsons, P. Field, and K. Furtado: "Cluster-Based Evaluation of Model Compensating Errors: A Case Study of Cloud Radiative Effect in the Southern Ocean", *Geophysical Research Letters*, **46** (6), 2019.

Schwendeman, M. and J. Thomson: "Observations of whitecap coverage and the relation to wind stress, wave slope, and turbulent dissipation", *Journal of Geophysical Research: Oceans*, **120** (12), 2015.

Seibert, P. and A. Frank: "Source-receptor matrix calculation with a Lagrangian particle dispersion model in backward mode", *Atmospheric Chemistry and Physics*, **4** (1), 2004.

Sellegri, K., C. D. O'Dowd, Y. J. Yoon, S. G. Jennings, and G. de Leeuw: "Surfactants and submicron sea spray generation", *Journal of Geophysical Research: Atmospheres*, **111** (D22), 2006.

Shindell, D. T., J.-F. Lamarque, M. Schulz, M. Flanner, C. Jiao, M. Chin, P. J. Young, Y. H. Lee, L. Rotstayn, N. Mahowald, G. Milly, G. Faluvegi, Y. Balkanski, W. J. Collins, A. J. Conley, S. Dalsoren, R. Easter, S. Ghan, L. Horowitz, X. Liu, G. Myhre, T. Nagashima, V.

Naik, S. T. Rumbold, R. Skeie, K. Sudo, S. Szopa, T. Takemura, A. Voulgarakis, J.-H. Yoon, and F. Lo: "Radiative Forcing in the ACCMIP Historical and Future Climate Simulations", *Atmospheric Chemistry and Physics*, **13** (6), 2013.

Slinn, W.: "Some Approximations for the Wet and Dry Removal of Particles and Gases from the Atmosphere", *Water, Air, and Soil Pollution*, **7** (4), 1977.

Smith, M. J., D. T. Ho, C. S. Law, J. McGregor, S. Popinet, and P. Schlosser: "Uncertainties in gas exchange parameterization during the SAGE dual-tracer experiment", *Deep Sea Research Part II: Topical Studies in Oceanography*, **58** (6), 2011.

Snyder, R. L. and R. M. Kennedy: "On the Formation of Whitecaps by a Threshold Mechanism. Part I:. Basic Formalism", *Journal of Physical Oceanography*, **13** (8), 1983.

Spearman, C.: "The Proof and Measurement of Association between Two Things", *The American Journal of Psychology*, **15** (1), 1904.

Stohl, A., C. Forster, A. Frank, P. Seibert, and G. Wotawa: "Technical note: The Lagrangian particle dispersion model FLEXPART version 6.2", *Atmospheric Chemistry and Physics*, **5** (9), 2005.

Stolzenburg, M.: "An Ultrafine Aerosol Size Distribution Measuring System", PhD thesis, University of Minnesota, 1988.

Stramska, M. and T. Petelski: "Observations of oceanic whitecaps in the north polar waters of the Atlantic", *Journal of Geophysical Research: Oceans*, **108** (C3), 2003.

Sugihara, Y., H. Tsumori, T. Ohga, H. Yoshioka, and S. Serizawa: "Variation of whitecap coverage with wave-field conditions", *Journal of Marine Systems*, **66** (1), 2007.

Trenberth, K. E. and J. T. Fasullo: "Simulation of present-day and twenty-first-century energy budgets of the Southern Oceans", *Journal of Climate*, **23** (2), 2010.

Truong, S. C. H., Y. Huang, F. Lang, M. Messmer, I. Simmonds, S. T. Siems, and M. J. Manton: "A Climatology of the Marine Atmospheric Boundary Layer Over the Southern Ocean From Four Field Campaigns During 2016–2018", *Journal of Geophysical Research: Atmospheres*, **125** (20), 2020.

Twomey, S.: "Comparison of constrained linear inversion and an iterative nonlinear algorithm applied to the indirect estimation of particle size distributions", *Journal of Computational Physics*, **18** (2), 1975.

Twomey, S.: "The Influence of Pollution on the Shortwave Albedo of Clouds", *Journal of the Atmospheric Sciences*, **34** (7), 1977.

Uetake, J., T. C. J. Hill, K. A. Moore, P. J. DeMott, A. Protat, and S. M. Kreidenweis: "Airborne bacteria confirm the pristine nature of the Southern Ocean boundary layer", *Proceedings of the National Academy of Sciences*, **117** (24), 2020.

Veres, P. R., J. A. Neuman, T. H. Bertram, E. Assaf, G. M. Wolfe, C. J. Williamson, B. Weinzierl, S. Tilmes, C. R. Thompson, A. B. Thames, J. C. Schroder, A. Saiz-Lopez, A. W. Rollins, J. M. Roberts, D. Price, J. Peischl, B. A. Nault, K. H. Møller, D. O. Miller, S. Meinardi, Q. Li, J.-F. Lamarque, A. Kupc, H. G. Kjaergaard, D. Kinnison, J. L. Jimenez, C. M. Jernigan, R. S. Hornbrook, A. Hills, M. Dollner, D. A. Day, C. A. Cuevas, P. Campuzano-Jost, J. Burkholder, T. P. Bui, W. H. Brune, S. S. Brown, C. A. Brock, I. Bourgeois, D. R. Blake, E. C. Apel, and T. B. Ryerson: "Global airborne sampling reveals a previously unobserved dimethyl sulfide oxidation mechanism in the marine atmosphere", *Proceedings of the National Academy of Sciences*, 2020.

Vergara-Temprado, J., B. J. Murray, T. W. Wilson, D. O'Sullivan, J. Browse, K. J. Pringle, K. Ardon-Dryer, A. K. Bertram, S. M. Burrows, D. Ceburnis, P. J. DeMott, R. H. Mason, C. D. O'Dowd, M. Rinaldi, and K. S. Carslaw: "Contribution of feldspar and marine organic aerosols to global ice nucleating particle concentrations", *Atmospheric Chemistry and Physics*, **17** (5), 2017.

Vergara-Temprado, J., A. K. Miltenberger, K. Furtado, D. P. Grosvenor, B. J. Shipway, A. A. Hill, J. M. Wilkinson, P. R. Field, B. J. Murray, and K. S. Carslaw: "Strong control of Southern Ocean cloud reflectivity by ice-nucleating particles", *Proceedings of the National Academy of Sciences*, **115** (11), 2018.

Voskresenskii, A.: "Condensation Nuclei in the Mirniy Region", *Sovet. Antarkticheskaia Eksped. Trudy*, **38**, 1968.

Walker, C. F., M. J. Harvey, M. J. Smith, T. G. Bell, E. S. Saltzman, A. S. Marriner, J. A. McGregor, and C. S. Law: "Assessing the potential for dimethylsulfide enrichment at the sea surface and its influence on air–sea flux", *Ocean Science*, **12** (5), 2016.

Wiedensohler, A.: "An approximation of the bipolar charge distribution for particles in the submicron size range", *Journal of Aerosol Science*, **19** (3), 1988.

Wiedensohler, A., W. Birmili, A. Nowak, A. Sonntag, K. Weinhold, M. Merkel, B. Wehner, T. Tuch, S. Pfeifer, M. Fiebig, A. M. Fjäraa, E. Asmi, K. Sellegri, R. Depuy, H. Venzac, P. Villani, P. Laj, P. Aalto, J. A. Ogren, E. Swietlicki, P. Williams, P. Roldin, P. Quincey, C. Hüglin, R. Fierz-Schmidhauser, M. Gysel, E. Weingartner, F. Riccobono, S. Santos, C. Grüning, K. Faloon, D. Beddows, R. Harrison, C. Monahan, S. G. Jennings, C. D. O'Dowd, A. Marinoni, H.-G. Horn, L. Keck, J. Jiang, J. Scheckman, P. H. McMurry, Z. Deng, C. S. Zhao, M. Moerman, B. Henzing, G. de Leeuw, G. Löschau, and S. Bastian: "Mobility particle size spectrometers: harmonization of technical standards and data structure to facilitate high quality long-term observations of atmospheric particle number size distributions", *Atmospheric Measurement Techniques*, **5** (3), 2012.

Wiedensohler, A., E. Lütkemeier, M. Feldpausch, and C. Helsper: "Investigation of the bipolar charge distribution at various gas conditions", *Journal of Aerosol Science*, **17** (3), 1986.

Williams, K., A. Bodas-Salcedo, M. Déqué, S. Fermepin, B. Medeiros, M. Watanabe, C. Jakob, S. Klein, C. Senior, and D. Williamson: "The Transpose-AMIP II experiment and its application to the understanding of Southern Ocean cloud biases in climate models", *Journal of Climate*, **26** (10), 2013.

Witek, M. L., D. J. Diner, and M. J. Garay: "Satellite Assessment of Sea Spray Aerosol Productivity: Southern Ocean Case Study", *Journal of Geophysical Research: Atmospheres*, **121** (2), 2016.

Wofsy, S. C.: "HIAPER Pole-to-Pole Observations (HIPPO): fine-grained, global-scale measurements of climatically important atmospheric gases and aerosols", *Philosophical Transactions of the Royal Society A: Mathematical, Physical and Engineering Sciences*, **369** (1943), 2011.

Xu, D., X. Liu, and D. Yu: "Probability of wave breaking and whitecap coverage in a fetch-limited sea", *Journal of Geophysical Research: Oceans*, **105** (C6), 2000.

Yang, X., J. A. Pyle, and R. A. Cox: "Sea salt aerosol production and bromine release: Role of snow on sea ice", *Geophysical Research Letters*, **35** (16), 2008.

Yin, B. and B. A. Albrecht: "Spatial Variability of Atmospheric Boundary Layer Structure over the Eastern Equatorial Pacific", *Journal of Climate*, **13** (9), 2000.

Young, I. R., S. Zieger, and A. V. Babanin: "Global Trends in Wind Speed and Wave Height", *Science*, **332** (6028), 2011.

Young, I.: "Seasonal Variability of the Global Ocean Wind and Wave Climate", *International Journal of Climatology*, **19** (9), 1999.

Yum, S. S. and J. G. Hudson: "Wintertime/summertime contrasts of cloud condensation nuclei and cloud microphysics over the Southern Ocean", *Journal of Geophysical Research: Atmospheres*, **109** (D6), 2004.

Zábori, J., R. Krejci, A. M. L. Ekman, E. M. Mårtensson, J. Ström, G. de Leeuw, and E. D. Nilsson: "Wintertime Arctic Ocean sea water properties and primary marine aerosol concentrations", *Atmospheric Chemistry and Physics*, **12** (21), 2012.

Zábori, J., M. Matisns, R. Krejci, E. Nilsson, and J. Ström: "Artificial primary marine aerosol production: a laboratory study with varying water temperature, salinity, and succinic acid concentration", *Atmospheric Chemistry and Physics*, **12** (22), 2012.